The Design and Development of a Spark Assisted Chemical Engraving System with Force Feedback Control

by

Zahraa Hassan Bassyouni

A Thesis submitted to the School of Graduate and Postdoctoral Studies in partial fulfillment of the requirements for the degree of

Master of Applied Science in Mechanical Engineering

Department of Mechanical and Manufacturing Engineering
Faculty of Engineering and Applied Sciences
Ontario Tech University
Oshawa, Ontario, Canada
December, 2023

Thesis Examination Information

Submitted by: Zahraa Bassyouni

Master of Applied Science in Mechanical Engineering

Thesis title: The Design and Development of a Spark Assisted Chemical Engraving System with Force Feedback Control.

An oral defense of this thesis took place on December 7, 2023 in front of the following examining committee:

Examining Committee:

- Chair of Examining Committee: Dr. Amirkianoos Kiani
- Research Supervisor: Dr. Jana Abou-Ziki
- Examining Committee Member: Dr. Sayyed Ali Hossenini
- Thesis Examiner: Dr. Meaghan Charest-Finn

The above committee determined that the thesis is acceptable in form and content and that a satisfactory knowledge of the field covered by the thesis was demonstrated by the candidate during an oral examination. A signed copy of the Certificate of Approval is available from the School of Graduate and Postdoctoral Studies

Abstract

Spark Assisted Chemical Engraving is a hybrid micromachining method capable of machining micro-holes and micro-channels on non-conductive substrates. This thesis centers around the design of a mechatronics system for precision manufacturing using SACE technology. The setup consists of a machining head and a processing cell. The electronics of the system are implemented on printed circuit boards and embodied in a well-ventilated box that connects the different components of the system. A current probe adapter that enables the reading of the current signal is designed. The system is modeled and controlled, and a force sensor that can detect machining forces is developed. A force-feedback drilling technique is implemented, where the machining continues with minimal contact forces (less than 200 mN). A preliminary study on characterizing the surface quality of machined holes was conducted, and a model that can characterize the surface texture of machined holes is developed.

Author's Declaration

I hereby declare that this thesis consists of original work of which I have authored. This is a true copy of the thesis, including any required final revisions, as accepted by my examiners. I authorize the University of Ontario Institute of Technology (Ontario Tech University) to lend this thesis to other institutions or individuals for the purpose of scholarly research. I further authorize University of Ontario Institute of Technology (Ontario Tech University) to reproduce this thesis by photocopying or by other means, in total or in part, at the request of other institutions or individuals for the purpose of scholarly research. I understand that my thesis will be made electronically available to the public.

Zahraa Bassyouni

Statement of Contributions

I hereby declare that this thesis consists of original work of which I have authored. The author's contributions to scholarly work related to this thesis are summarized below:

- A major part of Chapter 1 of this Thesis was published as part of a review paper: "Bassyouni, Zahraa, and Jana D. Abou Ziki. "The capabilities of spark-assisted chemical engraving: a review." Journal of Manufacturing and Materials Processing 4.4 (2020) 99."

- An abstract was published in proceedings of the Canadian Society for Mechanical Engineers conference and presented in Sherbrooke, QC: "Bassyouni, Zahraa, Trendov, Veronica, Abou Ziki, Jana (2023). The Development Of A Spark Assisted Chemical Engraving (SACE) Setup For Controlling The Surface Texture Of Machined Features. In Proceedings of the Canadian Society for Mechanical Engineering International Congress. Sherbrooke, QC."

- The author has also contributed in the submission of another paper on leveraging deep learning for characterizing the SACE process: "Sahebari, S. M. S., Bassyouni, Z., Barari, A., Abou Ziki, J. D. (2023). Intelligent Characterization of Spark-Assisted Chemical Engraving (SACE) Process Using Time Series Classification."

Part of this thesis, mainly excerpts from chapters 4 and 5, will be published as a conference paper/journal article.

Acknowledgements

I take the opportunity here to express my genuine feelings towards the people who have had a significant impact on me throughout this journey. A journey that has expanded my frontiers on many levels, with the academic level being the tangible outcome I'm proud to present today.

First and foremost, my deepest gratitude goes to my supervisor, Dr. Jana AbouZiki, who provided me with the opportunity and resources to complete a successful Master's program. Dr. Jana, thank you for believing in me during times I was so doubtful of myself, and for always encouraging me to strive for excellence.

I would also like to thank and acknowledge my fellow lab colleagues. Hazem, for the instrumental insights in designing the mechanical components of the system. Marwan for the numerous discussions on literature and the useful tips on machining. Mahmoud, for the AI discussions and help with the Dynamometer test. I would also like to thank Veronica, a previous intern at our lab, for her help in the PCB design.

I am deeply grateful to Peter Kahr, the technician at our university, for his support and assistance in creating parts for the setup. To all the people whom I have met in Canada and have shared a smile, a laugh, or a genuine thought with. You will always have a sweet spot in my heart.

And finally, my sincere gratitude goes out to my family. My mom, for her unwavering support throughout this journey. My dad, for always having faith in me. My sister, for being my first best friend and the person I'm most comfortable with. Lastly, my brother, for the joyful memories we've shared together.

Zahraa Bassyouni

Table of Contents

List of Tables

List of Figures

Abbreviations

ECDM Electrochemical Discharge Machining.

ESCON ESCON is a servo controller from Maxon motors.

KOH Potassium Hydroxide.

LM Linear Motor, and it refers to the voice coil actuator..

MRR Material removal rate.

NaOH Sodium Hydroxide.

SACE Spark Assisted Chemical Engraving.

Chapter 1

Introduction and Thesis Objectives

Spark Assisted Chemical Engraving (SACE) stands out as a non-conventional and hybrid manufacturing technique, demonstrating its significance in contemporary manufacturing processes. By utilizing thermally-assisted chemical etching, SACE enables the precise and controlled fabrication of micro-features, making it indispensable in various industries. Particularly notable is its ability to machine non-conductive materials, such as glass **??** and ceramics, which present formidable challenges to conventional machining methods. Moreover, SACE excels in rapid prototyping, offering a cost-effective solution for the swift customization of products.

Additionally, SACE distinguishes itself by simultaneously machining and texturing materials, a property with far-reaching implications across multiple engineering domains, including applications in tribology, where friction and wear properties are crucial [1, 2]. Moreover, its role extends to cell-based applications, enhancing the possibilities in medical and biological engineering [2]. Based on the research in the SACE field, it is evident that there are multiple modes of machining which result in various machining speed and quality. Therefore, it becomes clear that the SACE machine precision and capabilities are important for the performance of this process.

To achieve higher precision and accuracy with SACE machining, a SACE machine has been developed that allows machining while monitoring machining forces and compensating for them. The last is called force-feedback machining and it allows

enhancing the machining process and moving SACE towards the goal of digitalization within this domain.

Furthermore, the integration of Artificial Intelligence (AI) into SACE machining systems carries substantial implications. The utilization of machine learning and data-driven analytics in this context provides a pathway for the digitalization of the machining process. By harnessing data and predictive algorithms, SACE can move towards a more efficient, adaptive, and responsive approach. This transition towards online monitoring and predictive capabilities is integral for addressing contemporary demands for enhanced productivity, quality assurance, and competitiveness in manufacturing.

In summary, SACE's unique capabilities, combined with the integration of advanced force sensing technology and AI-driven digitalization, represent a pivotal advancement in modern manufacturing. These developments not only cater to the precision and customization needs of various industries but also lay the foundation for a future where machining processes become smarter, more efficient, and highly responsive to machining demands.

In this chapter, background information on Spark Assisted Chemical Engraving (SACE) is presented. All of the content in this chapter, with the exception of section 1.6, are excerpts from our published review paper on the capabilities of SACE [3]. Some figures were also newly constructed and inserted for the sake of this thesis.

The sections of this chapter unfold as follows: Section 1.1 starts with an overview about SACE, followed by how the process works (section 1.2), and its setup and three major machining modes (section 1.3). Then, a brief description on the gas film, a key element in SACE process, is presented (section 1.4) along with the main factors that influence it. Next, two major factors, the electrolyte and the machining voltage, that were highly reported in literature to affect the surface quality are reported (section 1.5). Section 1.6 presents the importance of digitalization and recent work on online monitoring in SACE manufacturing. And finally Section 1.7 presents the Objectives

of this Thesis.

1.1 SACE Overview

Spark−Assisted Chemical engraving, or SACE for short, is a hybrid technology that integrates chemical and thermal processes in the machining of several non-conductive materials. The technology is based on electrochemical discharge phenomena. Machining occurs due to thermally accelerated etching and machining zone temperature reaches levels up to 600 °C [4, 5]. Despite the existence of other machining technologies including mechanical, chemical, and thermal, SACE has advantages over other processes used for micro-machining non-conductive materials. Mainly, SACE does not require expensive or complex setup and can establish a variety of features (1 D to 2.5 D where 2.5 D refers to the machining of 2D structures but with varying depths) with aspect ratios (beyond 10) [6] and acceptable resolution (less than 0.5 μm surface roughness) at a relatively fast machining speed. This makes SACE a compatible technology for rapid prototyping of glass micro-parts and devices. Furthermore, SACE offers the possibility of modifying the surface properties, like texture while machining [7], fabricating micro-features on nanofiber layers [8] and modifying the surface of micro-features [9]. The research done about SACE in the past years has shown a promise that this technique can be further developed to establish micro-features with higher surface quality and at higher speed. Moreover, this technique has the potential to control the surface composition and structure while machining in a single step, contrary to most other micro-machining methods. Furthermore, it was demonstrated that SACE, in comparison to other manufacturing techniques like chemical, mechanical, and thermal, can eliminate intermediate steps in the process of manufacturing microfluidic and other lab-on-a-chip devices [10]. In rapid prototyping, sealing the machined devices through bonding them to glass is a critical step that might cause failure in the device manufacturing if not done properly [11–13]. Postprocessing steps, like polishing or particle removal, are needed to compensate

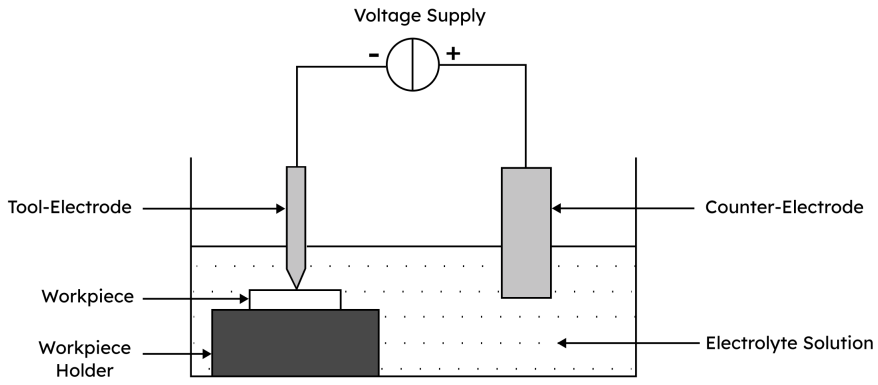

Figure 1.1: A schematic diagram of SACE process.

for any formation of bulges and bonding defects caused while machining by thermal [14–16] and mechanical [17, 18] processes, respectively. Recently, a glass device that was machined using SACE was successfully fusion bonded at high annealing temperature [3], and its performance was evaluated qualitatively and quantitatively [19]. Investigations revealed good bonding and no leakage.

1.2 SACE Process

SACE process can be summarized as follows. The sample to be machined is dipped in an electrolytic solution in a position just below a machining tool, referred to as the tool-electrode. This machining tool is a metallic electrode, usually a cathode, connected through a Direct Current (DC) voltage to another metallic counter electrode (anode), as shown in Figure 1.1

Both electrodes are also dipped in the solution, with the cathode having a smaller surface area than that of the anode. When the applied voltage reaches a critical value of around 30 V, the previously formed bubbles coalesce into a gas film, causing emissions of light and generations of high energy electrical discharges [20, 21]. These conditions contribute to the machining of the workpiece. This novel technology can be

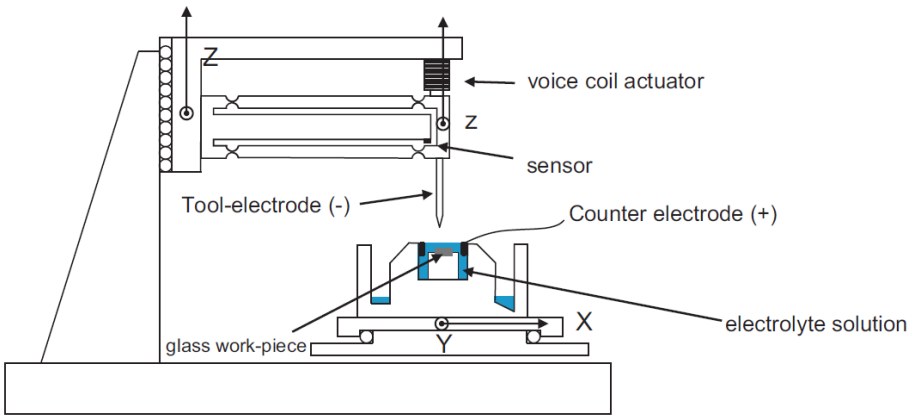

Figure 1.2: Schematic of a conventional SACE set-up. An XYZ Cartesian robot embodies a machining head (that holds the tool) and a processing cell containing the workpiece. Reprinted from the work in [22] with permission from Elsevier

used on non-conductive materials like glass and ceramics to perform several machining operations like drilling holes, milling micro-channels and micro-grooves, die-sinking, cutting micro-slits, turning, and grinding.

1.3 SACE Setup and Machining Modes

A machining head and a processing cell, mounted on the XYZ of a Cartesian robot, compose the setup of a conventional SACE machine, as shown in figure 1.2. The machining head embodies the following; the tool-electrode, a flexible structure that holds the tool and allows it to move freely with a displacement z along the Z-direction, a voice coil actuator that can control z, and an optical sensor to measure z. The processing cell can move in the XY directions and embodies the workpiece, counter-electrode, and electrolytic solution. Regarding the machining modes, there are two main modes commonly used in literature. The first mode is the gravity feed. In this mode, the tool is pushed down by a constant force F—which is basically the weight of the structure holding the tool—to maintain contact between the tool (source of heat) and the workpiece. Until now, the gravity-feed is considered the simplest strategy as it has no complicated technical details. The tool–workpiece contact ensures similar temperatures between the tool and machining zone. The other common machining

mode is the constant-velocity feed. This machining mode, in comparison to the first one, feeds the tool with a constant feed rate (f). Contrary to gravity-feed machining where the tool is always in contact with the substrate, in constant-velocity feed the tool occasionally contacts the surface. This occurs due to the lack of monitoring for drilling depth and progress, leading to contact between the tool and the workpiece when Material Removal Rate (MRR) is slow. Tool–substrate contact can be avoided especially for shallow machining depth (less than 200 μm usually) depending on the chosen tool feed rate. Recently, this strategy has been integrated with force-feedback algorithms to reduce the tool–substrate contact and hence tool bending even for high depths. Basically, the contact force between the tool and workpiece is monitored and minimized while machining. It is worth mentioning that the gap between the tool and workpiece is not constant and, until now, controlling it is not yet possible due to the fact that the tool is conductive while the substrate is non-conductive. This hinders an accurate control of the process and hence the machining integrity and surface quality as the two machining limiting factors, heating and flushing, differ depending on this gap. As mentioned earlier, this process is based on thermally accelerated etching, and therefore the presence of electrolyte in the machining zone through flushing it and the proximity of the tool, which is the heat source, to the substrate are crucial to the machining progress [7]. Figure 1.3 illustrates the major differences between the two main strategies.

1.3.1 Gravity-Feed Machining

In this machining mode, the tool remains in contact with the surface of the workpiece, where the gravity effect allows it to keep pushing on the surface. Machining progress can be monitored without the use of any additional signal due to this continuous contact. In gravity-feed drilling, machining can be divided into two basic regimes: Discharge regime and hydrodynamic regime [23]. The first regime is in the case of low depths (typically less than 200 μm), and is controlled mainly by the amplitude

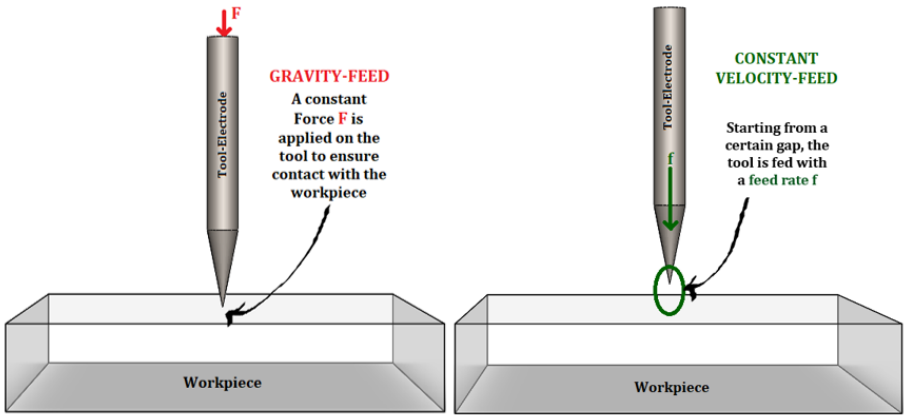

Figure 1.3: A schematic comparing the two most common types of machining

of applied voltage where drilling speed can reach up to 100 μm/s for a certain applied voltage (33 V). In the latter regime, drilling depth is high ($\geq$ 200μm), and the drilling speed reduces drastically as machining is hindered by insufficient flushing of electrolyte into the machining zone. Maillard et al. [24] identified four distinguished types of holes based on the applied voltage and drilling depth. Cylindrical holes having smooth surfaces were successfully machined at low depths ($\leq$ 100μm) or a low voltage (28 V and depths up to 300 μm). Jagged holes appeared at higher depths (200–300 μm, 30 V), holes with some heat-affected zones (HAZ) were the results of higher voltages (greater than 30 V), and holes with cracks appeared at 37 V. In general, it was found that as machining depth exceeds 200 μm, it becomes more challenging to limit HAZ and width overcut of holes. Several efforts have been made in the light of improving the machining performance. Wüthrich et al. [25] revealed that the addition of tool vibrations decreased the machining time to half its initial value where 300 μm deep micro-holes were drilled in about 10 s or less. A similar approach to enhance flow of electrolyte into deep holes was done by Han et al. [26] through applying pulsed voltage and ultrasonic vibrations to the electrolyte. The approach effectively increased the machining depth (as shown in Figure 1.4) but increased overcut and geometric inaccuracies.

This approach used a side-insulated tool of diameter 0.2 mm along with pulsed

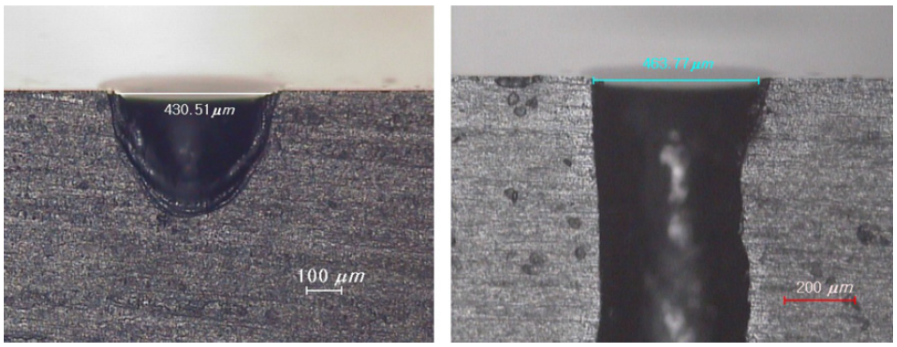

Figure 1.4: Difference in machining depth between (a) without using pulse voltage and vibrated electrolyte and (b) with pulse voltage and vibrated electrolyte. Republished with permission of Institute of Physics (IOP) Publishing, Ltd., from Geometric improvement of electrochemical discharge micro-drilling using an ultrasonic-vibrated electrolyte, Han et al., 19, 2009; permission conveyed through Copyright Clearance Center, Inc.

voltage and proved better in improving hole geometry (diameter was reduced from 0.426 mm to 0.328 mm) and depth increased to a value of 550 μm. Another combination of using a pulse voltage along with an unconventional tool geometry (having a front that is flat-sidewall-flat) was done by Zheng et al. [27] at a machining depth of 450μm. Taper was significantly reduced where hole entrance decreased from 570μm (for cylindrical tool) to 330μm.

Furutani et al. [28] achieved a groove depth of around 600 μm at a rotation speed of 30 rotations per minute and 40 V applied voltage with smooth bottom surface and some micro-cracks. The groove's depth, width, and surface roughness increased as the applied voltage increased. These values were achieved while rotating the workpiece to allow the flow of fresh electrolyte into the machining zone. Another approach to facilitate the flow of electrolyte to the tool–workpiece gap was done by Mehrabi et al. [29] using pressurized injection systems at various pressure levels and using hollow tool-electrodes with several outer and inner diameters. One end of the tool was in contact with the workpiece while the other was connected through a tube to an injection system. The anode was made of steel and placed 10 cm away from the cathode. Under a machining voltage of 75 V, hole depth was improved by 70% using

a 1.7 mm electrode diameter and 60% and 55% using an electrode diameter of 1.4 mm and 1 mm, respectively. These results showed an increase in materials removal rate (MRR). However, oversized hole diameter can result from high injection pressure.

Overall, this strategy clearly demonstrated successful results especially for hole depths below 300 μm. In the case of hole depth above 300 μm, this strategy suffers from the drawback of limited flushing and hole deformation due to the continuous tool–workpiece mechanical contact. Another drawback is the high possibility of tool bending in case of small tool sizes, which limits the minimum diameter of used tools to 200 μm.

1.3.2 Constant Velocity-Feed Machining

In this machining mode, the tool is fed with a constant feed rate (f) offering the potential of avoiding any contact between the tool and workpiece, which can solve the problem of tool bending. The tool here is moved towards the substrate at a constant feed rate where it proceeds vertically downward while machining. When the feed rate is lower than the MRR, a variable tool–workpiece gap is created. While this gap enhances the local flow of electrolyte at the machining zone, it causes the last to possess a lower temperature compared to that of the tool-electrode (the heat source). Moreover, and up to this date, the gap cannot be controlled which hinders online monitoring of the machining progress. Recent efforts have been made by Abou Ziki et al. [30] to measure the tool–substrate gap towards the end of machining. This was done for several machining conditions and a thermal model was constructed to explain the gap values measured. Temperature of machining zone and local flushing were identified to be the two factors that affect the value of the gap, which was found out to be around 10 μm or less in [30]. The model implies that the gap grows until the temperature of the surface reaches the melting temperature of the electrolyte salt. The gap does not grow further for lower temperature since the electrolyte solidifies and etching stops. Note that initially, at zero gap, the surface temperature is considered

to be similar to the tool temperature. Other efforts to control and monitor the process are exerted through developing force feedback algorithms, which is discussed in depth in the following section.

Drilling Forces

A novel attempt by Abou Ziki et al. [22] paved the way in developing force feedback algorithms that are expected to improve the machining performance. During drilling, the tool moves vertically downwards at a specific feed rate while the machining head (that holds the tool) acts as a force sensor that measures the forces applied on the tool. In this study, a feedback signal based on the contact forces between the tool-electrode and the workpiece was proposed as a possible way to monitor the process. Three different force patterns were distinguished based on the hole depth (feed rate) and applied voltage. Electrolyte flushing and workpiece surface heating were identified as the limiting factors in cases of high depth and low depth respectively. It was found that the range of allowable tool feed rates increases (up to 70 μm/s) for smaller tool diameters (250 μm) and at a machining voltage of 33 V. The forces were also studied from the current signal point of view where a correlation was identified between applied forces and current shifts as shown in Figure 1.5.

A further investigation on the nature of the drilling forces occurring at the tool-substrate vicinity was done by Abou Ziki et al. [31] and revealed that a chemical bond can form between the tool and the glass surface even before any contact between them occurs. This bond was explained as the result of the formation of an adhesive glass melt (sodium silicate) during the etching process. Basically, the contact forces that exist towards the end of machining, called Pressing Forces, start decaying after the applied voltage is switched off due to tool-retraction caused by a temperature drop in the machining zone. These decaying forces can either decay into a positive value or a negative value. In the case where pressing forces are low ($<$0.25 N), forces decay negatively indicating that the tool is being pulled downwards toward the

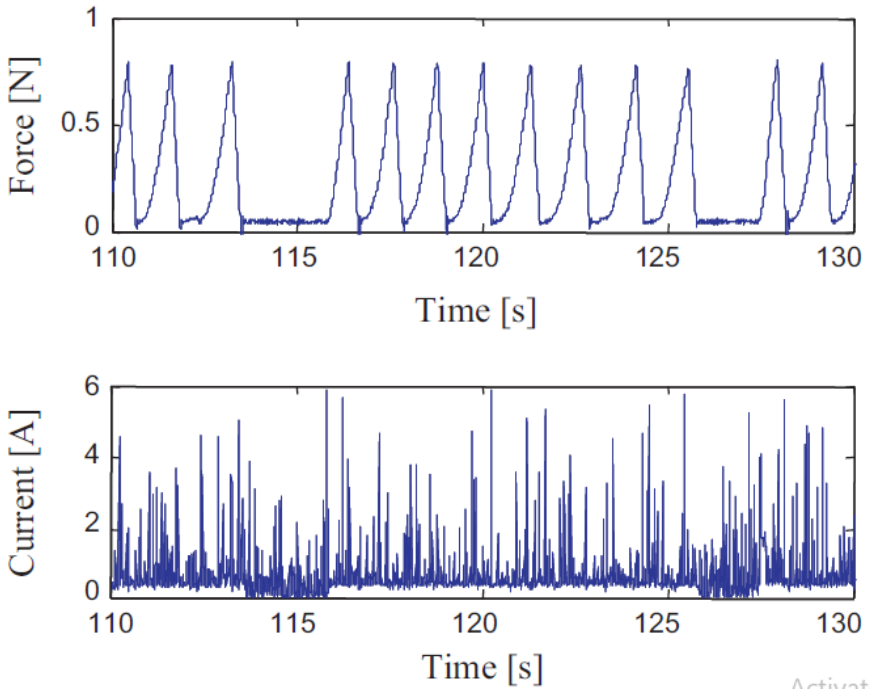

Figure 1.5: The force signal and its corresponding current signal for a machining voltage of 33 V and feed rate of 15 μm/s. Reprinted from the work in [22] with permission from Elsevier.

workpiece then values go back to zero indicating that the tool–glass bond was broken. This phenomenon results in interrupted drilling and its causes vary depending on machining conditions and machined geometry. In case of deep holes and continuous tool–glass contact, machining temperature is similar to that of the tool, and machining is hindered by insufficient electrolyte flushing. In the case of low depth and shallow surfaces, machining temperature is equal to vaporization temperature of electrolyte, and machining is hindered because of insufficient heating of workpiece surface. This causes the formation of a glass melt in the tool vicinity that creates a tool-glass adhesive bond [32].

1.4 The Gas Film

As mentioned earlier in the introduction, SACE process is based on electrochemical discharge phenomenon. The electrical discharges generated from the tool tip during

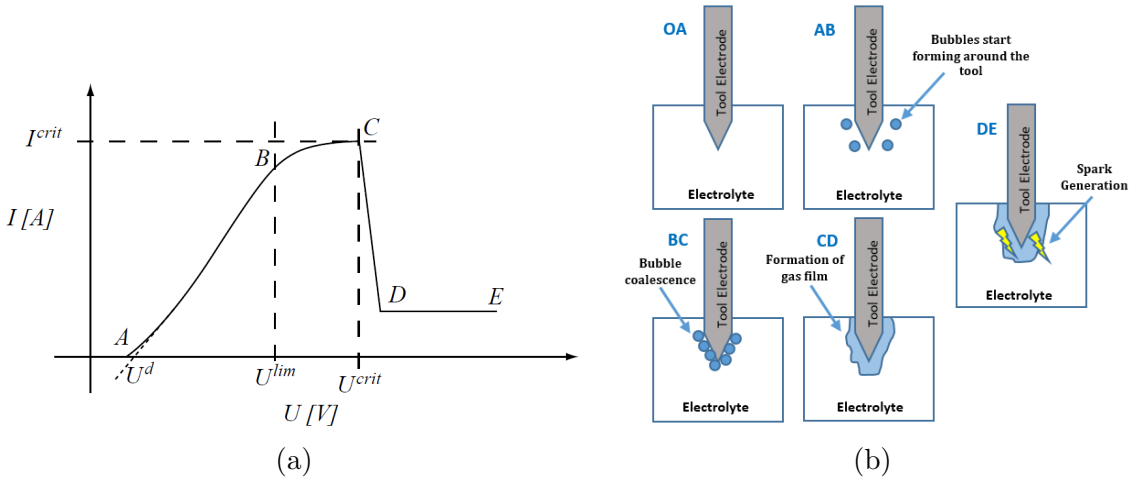

Figure 1.6: (a) The I–U characteristic curve during SACE. Reprinted from the work in [6] with permission from Elsevier. (b) The gas film formation process around the tool-electrode.

the process cause the local heating effect, making the tool the heat source. These discharges occur through the gas film that forms around the tool and isolates it from the surrounding electrolyte. The properties of this gas film affect the quality and repeatability of the process, making it a substantial element in SACE machining [33]. For example, the discharge activity is influenced by the shape of the gas film, thus the resulting overcut is affected. The gas film forms and breakdowns every few milliseconds and keeps on reforming continuously during the machining process. Therefore, it influences the local electrolyte flow dynamics in the tool vicinity which in turn has effects on the surface topography and quality. Consequently, it is fundamental to understand the factors and parameters that influence the gas film properties. The gas film formation cycle was divided into five regions in past literature [34–37] based on the mean I–U characteristics curve shown in Figure 1.6(a). The five regions 1.6(b) are summarized below.

- OA: Thermodynamic Region: The water's decomposition potential (U^d) is not yet reached, and no electrolysis occurs.
- AB: Ohmic Region: Water electrolysis occurs.

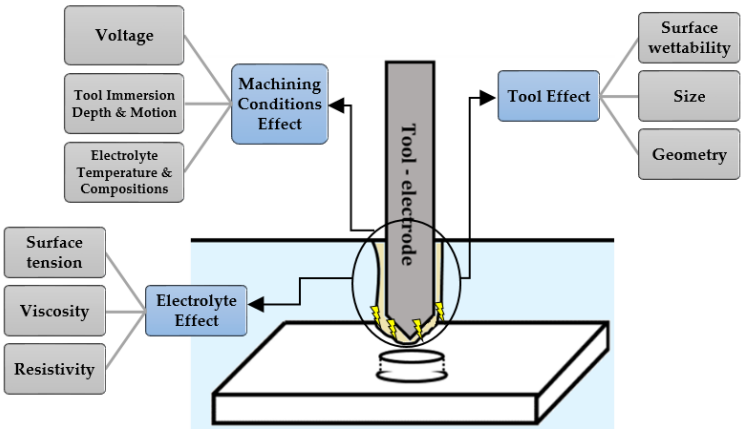

Figure 1.7: The different factors that affect the gas film.

- BC: Limiting-Current Region: Bubbles coalesce saturating the current.
- CD: Transition Region: A gas film starts forming around the tool covering its surface; machining becomes possible. A current density of around 1 A/mm^2 is generally required for gas film formation.
- DE: Arc Region: Nucleation sites of active bubbles are covered now with the gas film, and current is transported through micro-level arc discharges.

Basically, the qualities used to indicate the stability of the gas film are its shape, thickness, lifetime, and formation time, as well as the standard deviation of discharge current. Many factors (shown in Figure 1.7) influence these qualities, these mainly include the machining conditions (voltage, tool immersion depth and motion), the electrolyte properties (surface tension, viscosity, and resistivity), and tool-electrode properties (surface wettability, size and geometry).

1.5 The Major Process Parameters

The following subsections present literature on the effect of varying aspects related to one of the three most influencing process parameters: electrolyte, tool, and machining voltage.

1.5.1 The Electrolyte

In spark-assisted chemical engraving, the used electrolyte plays a key role in machining as the etching rate is greatly influenced by the electrolyte properties [38]. In consequence, the electrolyte affects MRR, surface quality, and overcut. This section presents the effects of electrolyte nature (used material), electrolyte concentration level, and electrolyte additives while machining on glass.

Electrolyte Material

In general, NaOH and KOH are the two mostly used electrolytes in literature, where NaOH is unique in its high viscosity, while KOH in its high conductivity. Gupta et al. [39] compared the material removal rate (MRR) and overcut using three electrolytes (Sodium Chloride (NaCl), Sodium Hydroxide (NaOH), and Potassium Hydroxide (KOH) at same concentration (25 wt%) while using a pulsed voltage in a glass drilling application. NaOH resulted in a higher MRR compared to KOH and NaCl by (3.8 and 9.7 times higher respectively), while KOH resulted in less overcut than NaOH and NaCl by a factor of 1.26 and 3.26 respectively. A mixed electrolyte (50% NaOH and 50% KOH) was used in [40] in micro-channel machining and achieved a 20.78% and 13.33% decrease in critical voltage and entrance width respectively at a 25 wt% concentration for each. Furthermore, 31.9% increase in channel depth was achieved when using this mixed electrolyte, compared to when NaOH electrolyte at same concentration (25 wt%) was used and while rotating the tool at 800 rpm and applying 32 V. Furthermore, alkaline solutions perform better than acidic ones. Harugadi et al. [41] compared MRR in a drilling ECDM experiment on soda lime glass using two electrolytes: basic KOH and sulfuric acid H2SO4. The authors noted that bubble generation in the acidic solution was almost negligible resulting in poor MRR.

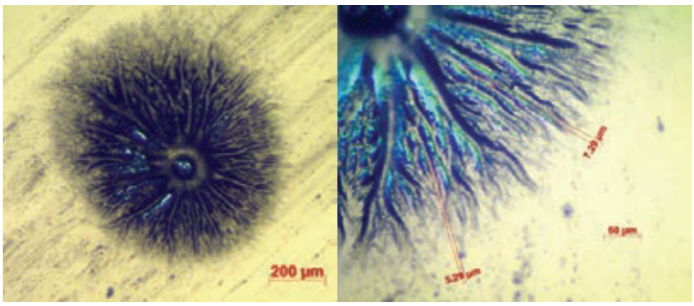

Figure 1.8: Surface wrinkles observed under Microscope on 0.4 M sample. Reprinted from the work in [44] with permission from Elsevier.

Electrolyte Concentration

Decreasing the levels of electrolyte concentration is advisable for achieving high aspect ratios and improving surface quality and integrity. Jui et al. [42] achieved a high aspect ratio of 11 during micro-drilling of glass using a 30 μm tungsten carbide and sulfuric acid as the electrolyte. The concentration used (10 wt %) resulted in an 18%, 22%, and 39% reduction in hole taper, overcut, and tool wear, respectively. Following this, a mathematical model that captures the relation between electrolyte concentration and overcut in machined surfaces was proposed by Kamaraj et al. [43]. The fabrication of micro-holes with aspect ratios as high as 12 was achieved in this contribution using NaOH as the electrolyte. However, Kolhekar at al. [44] revealed that as concentration levels drop below 1 M, surface wrinkles are produced in the perimeter of the machined hole surface as shown in Figure 1.8.

Surface hardness, on the other hand, was reduced with the decrease in electrolyte concentration and was observed in a range between 350 and 800 Vickers hardness number. The effect of varying concentration of three electrolytes (NaNO3, NaOH, and KOH) on the critical voltage was also compared by Zhang et al. [45]. For the same concentration, NaNO3 had the highest value of critical voltage among the three, KOH came second, and NaOH had the lowest value. As the concentration increases, the critical voltage is reduced by around 34 % with KOH, 30 % with NaOH, and 9 % with NaNO3. Madhavi et al. [46] and Bellubi et al. [47] confirmed that MRR increases

with the increase in electrolyte concentration while using a 0.63 mm stainless-steel tool and a 0.3 mm tungsten carbide tool respectively. Using the Taguchi method, similar optimized values for maximum MRR were obtained. It was identified that MRR is maximum for the following values of process parameters; 60 V machining voltage, 30 wt% electrolyte concentration and 70% duty factor in [74], and 50 V voltage, 25 wt% concentration, and 70% duty factor values in [47].

Addition of Surfactants/Magnetic Fields

Another significant factor that achieved improved surface quality is the addition of surfactants and particles to the electrolyte. The addition of around 0.2 % Sodium Dodecyl Sulfate Surfactant (SDS) to 6 M KOH electrolyte during drilling of quartz glass was investigated by Laio et al. [48]. This resulted in an increase in current density and improved machining capability, where the etched area increased from around 0.246 mm2 (without SDS) to 0.313 mm2, indicating a 27 % improvement in etching capability. This improvement was explained by the increase in the amount of bubbles formed and their speed in leaving the electrode surface thus leading to a reduction in gas film thickness. Similarly, the addition of 20 mL soap to 200 mL NaOH electrolyte as done by Wuthrich et al. [49] resulted in a 25 % decrease in critical voltage. A similar experiment was done by Han et al. [50] where the effects of mixing Graphite powder with 30 wt % NaOH electrolytes on surface integrity were investigated. A 10% reduction in peak current and breakdown voltage were achieved while machining on a borosilicate glass. Consequently, an improved surface quality was obtained compared to that obtained with traditional electrolyte where a surface roughness of 0.95 μm was obtained using 0.5–1 wt % concentrations of powder at an applied DC voltage of 35 V. The effect of adding graphite powder in improving machined features was also confirmed by Paul et al. [51].

In a cutting operation of Pyrex glass, Yang et al. [52] achieved a 43 % decrease in surface roughness through adding SiC abrasives (silicon carbide) to KOH electrolyte

while the workpiece was driven by a speed control motor. A 0.25 mm brass wire was used as the cathode with 30 mm of its length immersed in the electrolyte, and a pulsed voltage with different frequencies was applied. Despite the improvement in surface quality, abrasives were poorly circulated which caused a concentration polarization of electrolyte and blocked the machining zone. In an effort to improve the circulation of SiC abrasives, Kuo et al. [53] used a micro tube pump to continuously supply titrated electrolyte over the quartz glass workpiece. The electrolyte was composed of 5 wt % SiC mixed with 5 M KOH under the action of magnetic stirrers rotating at 150 rpm. The flow of titrated electrolyte flushes away debris generated at the machining zone. The proposed method improved surface roughness and mean slit width by 80% and 7.5 %, respectively, where the optimum process parameters for achieving such results were a 35 V applied voltage, 4 mL/min flow rate, 210 s machining time, 5 μm/s feed rate, and 5 wt% Sic powder concentration. An effort to improve the quality and depth of micro-channels was done by Hajian et al. [54] through investigating the effect of magnetic field orientations in combination with different machining voltages and electrolyte concentrations. The experiment was done on soda lime glass using a 0.5 mm flattened end high speed steel (HSS) tool-electrode using NaOH electrolyte of 15 wt% and 30 wt% concentration. The authors stated that the presence of a magnetic field results in a smoother surface, and with the right combination of electrolyte concentration and applied voltage (e.g., 15 wt%, 35 V), machining depth can increase by around 43 %. They also observed that at low electrolyte concentration (15 wt %), the presence of a magnetic field highly intensifies the effect of applied voltage in increasing the machining depth. In contrast, at higher electrolyte concentration (30 wt %) the effect of applying a magnetic field in increasing machining depth was only 4%.

1.5.2 Machining Voltage

The use of a rectified constant DC voltage was the conventional method in SACE machining. In general, machining experiments have revealed an exponential increase in MRR as the applied voltage is increased [55, 56]. However, literature found some limitations. At high machining depths, even if the applied voltage increases beyond 100 V, MRR starts decreasing due to insufficient flow of electrolyte into the machining gap [57]. Moreover, micro-cracks appear at groove depths of around 200 μm and at an applied voltage of 35 V [58]. Over the last two decades, the use of a pulsed voltage in SACE machining to overcome such disadvantages was investigated more in literature, where it offered great results in improving machining conditions for glass is presented in this subsection.

The utilization of a pulsed voltage of different frequencies and duty ratios was proposed by Kim et al. [5] to overcome the drawbacks of thermal damage in ECDM. It was found that HAZ is reduced with the increase in frequency and decrease in duty ratio. The results were confirmed by Zheng et al. [59] while using a flat-sidewall flat-front tool instead of the conventional cylindrical tool used in [5]. In this experiment, the formation time of the gas film was 1.5 ms with a 100 μm sidewall thickness, 40 V DC voltage, and 450 μm depth. Consequently, the pulse on time was chosen as 2 ms to perform experiments with a pulsed voltage while the pulse-off time was varied. Although entrance diameter dramatically decreased (from 570 μm to 340 μm) and no cracks were observed, machining time increased from 40 s to 160 s as pulse off time was increased to 2 ms, as shown in Figure 1.9. Authors attributed this phenomenon to the limited discharge energy/unit and the consumption of high amounts of energy for electrolyte heating.

In an experiment done by Zhang et al. [45], the gas film formation time decreased to around 0.05 ms as the magnitude of applied pulses increased to 25 V. The experiment was done using a 0.2 mm tungsten carbide tool at 1000 rpm tool rotational

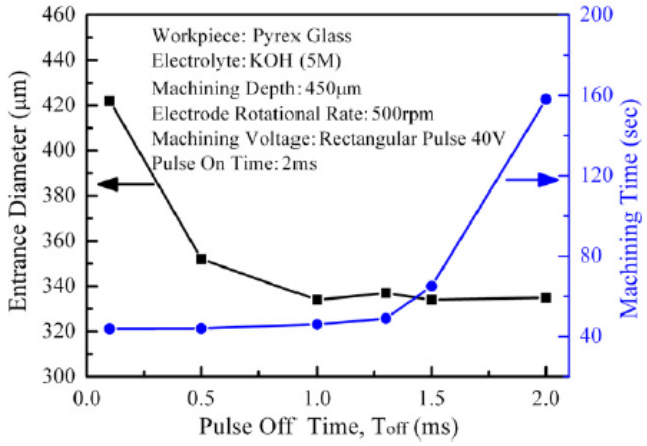

Figure 1.9: Variations of Entrance diameter and machining time as a function of the pulse off time. Republished with permission of IOP publishing, Ltd., from "The tool geometrical shape and pulse-off time of pulse voltage effects in a Pyrex glass electrochemical discharge micro-drilling process",Zheng et al., 17, 2007; permission conveyed through Copyright Clearance Center, Inc

speed, a 500 Hz frequency, 50% duty cycle, and using a 20 wt% NaOH electrolyte. Authors noted that at lower magnitude (19 V), diametric overcut was smaller and less micro-cracks were observed in comparison to the case at 25 V. However, the machining time was drastically increased from 48 s at 25 V to 130 s at 19 V. To put it simply, although this method proved efficient in improving machining quality, it poses the problem of having an efficient machining rate. A novel attempt to increase machining efficiency was done by Zheng et al. [60] through introducing the offset pulse-voltage configuration. During the pulse off time, the gas film is allowed to reconstruct itself, resulting in unpredictable discharges and an unstable gas film. To solve this, a constant voltage of 10 V (referred to as offset voltage in this experiment) is added during pulse off time to enhance the stability of the gas film. Results showed a 60% decrease in machining time and standard deviation. Although this method didn't alter the geometry of the machined hole, a slight increase in the fillet angle in micro-hole entrance was noted. A finite element modeling of the process was done by Paul et al. [61] to compare MRR with a constant voltage versus a pulsed voltage.

For the same process conditions, MRR was increased by around 62% using pulsed voltage.

1.6 Digitalization and Online monitoring in SACE

Within SACE, the chosen drilling strategy has a significant influence on machining quality. To enhance control over the process, feedback algorithms have been applied. In a previous study [62], the authors utilized the optical sensor voltage signal to monitor the drilling process, proposing a technique that combines both gravity-feed and constant velocity-feed methods. However, a drawback of this method is the continuous contact between the tool and the workpiece, which can lead to increased geometric inaccuracies and tool wear. In another research endeavor [63], authors developed a force-feedback drilling approach that relies on detecting contact forces between the tool and the workpiece using a pressure sensor. This method demonstrated notable improvements in terms of efficiency and accuracy when compared to traditional gravity-feed and constant velocity-feed methods. A pressurized feeding mechanism was developed in [64] in an effort to keep the tool-workpiece gap constant. Pressure is applied to the workpiece by creating a holding fixture that enables the exertion of force on the workpiece. For the same machining conditions, the machining depth was improved by 207.4% using the monitored drilling technique over the traditional method.

Moreover, artificial intelligence holds significant potential for elevating the controllability and precision of SACE. By collecting data during the machining process, particularly the current and force signals, which are indicative of the machining status, the process can be enriched with intelligence and improved controllability. Recently [65], a composite algorithm leveraging deep learning techniques was developed to characterize machining performance. Specifically, the current signal was employed as time series data, and deep learning techniques, including Temporal Convolutional Networks and LSTM networks, were harnessed to extract crucial parameters related

to the process, such as gas film formation time and lifetime, both of which can be derived from the current signal. This marks a significant step towards achieving process monitoring in the realm of SACE.

In this thesis, some of the main components of the SACE machine have been designed and built including mechanical and electronics systems necessary to the function of the machine. Furthermore, a force sensor with enhanced resolution, around 15 mN, has been designed and implemented, contributing to the enhancement of precision and controllability within the SACE process. And lastly, a preliminary model is developed that leverages machine learning algorithms to characterize the surface texture of machined holes.

1.7 Thesis Objectives

This master's thesis objective is the design and development of critical components of some of the SACE machine main components, encompassing its electrical and electronics system, control system, processing cell, workpiece holder, and the electrolyte overflow pump system. A force sensor is designed and implemented which enables a zero-displacement mode in the machining head. This actuator plays a pivotal role in force-feedback drilling, facilitating the drilling of micro-holes with zero contact forces between the tool and the glass workpiece which allows the generation of different surface textures.

The next step involves controlling surface texture. This thesis only takes a preliminary step in this direction. The PID system eliminates tool-workpiece contact, enabling the generation of multiple textures. A machining gap is always maintained, allowing the imprinting of local flow patterns of the electrolyte to produce different textures. The effect of the PID in creating diverse textures is examined through a machine learning (ML) application.

To fulfil the aforementioned objective, The following work is conducted:

- Electrical and Electronics System: The development of printed circuit boards (PCBs) to facilitate the connection and transmission of signals within the SACE machine.

- Control System: Designing PID controller that allows reading sensor signals from the machine head and controlling actuators accordingly. These signals and the XYZ stage motion signals are transmitted between a motion controller, real time dSPACE control board and the machine head.

- Processing Cell Design: Designing a processing cell that optimally accommodates the electrolyte and prevents leakage. The cell is connected to a pump to control the electrolyte overflow during the SACE process.

- Workpiece Holder Design: Creating a workpiece holder that securely and effectively positions the workpiece, maintaining fixture throughout the machining process.

- Force Sensor Development: The development of a force sensor enables the SACE machine to sense and respond to minimal forces acting on the tool, thereby facilitating force-feedback drilling with zero contact forces between the tool and the glass workpiece.

- Machine Learning Model for Surface Texture Prediction: To test the PID's ability to elimintate the tool-workpiece contact and enable different surface textures to be generated, experiments are conducted and a model is developed to predict the resulting surface texture of micro-holes, given a set of process parameters.

Chapter 2

SACE System Design and Development

SACE system is composed of different mechanical and electrical components, as shown in figure 2.5. The machining head is the sole component not developed in-house; it was designed and manufactured at Concordia University and imported without modifications. All other major components were designed as part of this thesis deliverable, including the processing cell and the workpiece holder, four PCBs that facilitate data retrieval and communication, the Data Interface Unit that houses the PCBs and motor controllers, and finally the Current Probe adapter that houses two PCBs. All of the in-house designed components would include the terms "Design of " in their section titles. The following briefly describes the role of each component in the chapter:

- The machining head is mounted to the Z-stage, while the processing cell is mounted on the XY-stages of an XYZ Cartesian system provided by Newport.
- The processing cell was structured in three layers and embodies workpiece holder, electrolyte, and counter-electrode.
- The XYZ stages are interconnected with an XPS motion controller (master controller) and their operation is facilitated through the XPS interface, programmed using the TCL programming language.
- The dSPACE data acquisition board was used as a slave controller, for data

processing, visualization and control of SACE signals. The dSPACE board signals (blocks) are accessible through Matlab (Simulink model). ControlDesk software, connected to Simulink model, is a graphical interface that allows real-time visualization, control and recording of these signals.

- A Data Interface Unit was built to enable communication between the XPS motion controller (Master) and dSPACE motion controller (Slave). This unit incorporates custom-designed PCBs that establish a link between the input/output (I/O) channels of these controllers, enabling efficient and minimal-noise exchange of data.

- A current probe adapter was crucial to address the need for recording of the current signal during SACE machining. This adapter allows connecting the current probe to the BNC channel of dSPACE.

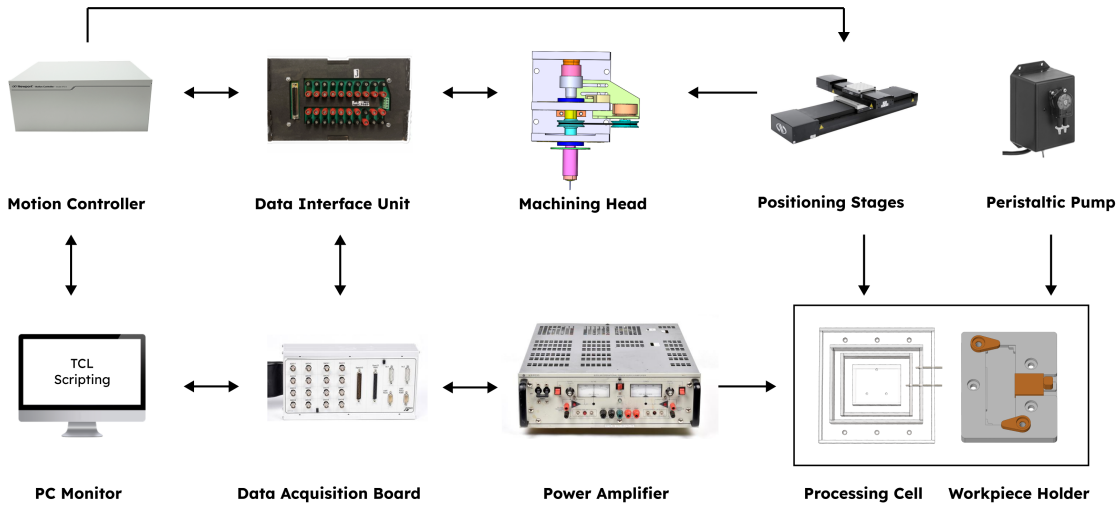

Figure 2.1: The electrical system and signal directions in SACE machine

2.1 Machining Head

The machining head (mounted on Z-stage) embodies the tool that is supported by a flexible structure that enables internal z-motion in the head (extra degree of free-

dom)and can be controlled by a voice coil actuator (LA10-12-027A). The tool is capable of rotating along the Z direction by a rotary motor (Maxon EC32) through a collet-spindle assembly. An optical sensor (SFH9206) is used to detect any movement in the z-direction, as shown in Figure 2.2. The optical sensor and voice coil assembly allow the machining head to operate in two configurations: A profile-meter and a force sensor. In the first configuration, the sensor is used to find the substrate (glass) surface level and detect any deflections in the z-direction. In the second configuration, when the voice coil is activated, the head is used as a force sensor to detect machining forces. In the second mode, a PID controller is designed to keep the flexible structure rigid as opposed to first mode where the structure is free to move in z direction.By moving the head as a rigid entity in the Z-direction, any machining forces exerted on the tool will be detected and compensated by voice-coil actuator. The force exerted by the voice coil on the tool is an equal but opposite to machining forces exerted on the tool. The PID controller is further described in chapter 3 and it controls the voltage sent to the voice coil through a zero-displacement measuring principle.

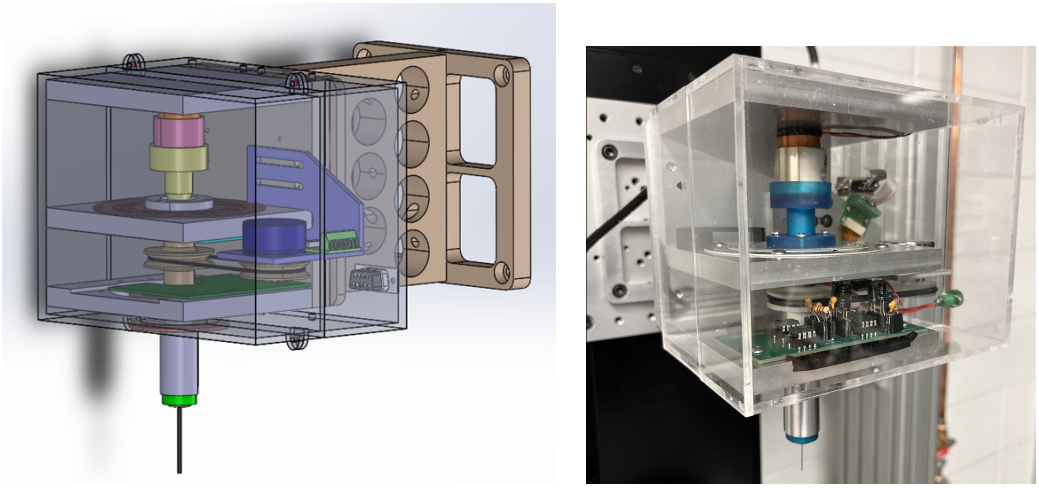

(a) (b)

Figure 2.2: Machining Head. (a) SolidWorks Design. (b) Physical Implementation. Note that the design of the head was conducted in Concordia University in Montreal.

2.2 High Precision Positioning Stages

The relative motion between the tool (machining Head) and the workpiece (Processing Cell) is facilitated by an XYZ three axis platform from Newport. As the accuracy and precision of the machined features are important in micro-machining, it is crucial to choose a high-performance stage in all three directions. An ILS100BPP, ILS150BPP, and an IMS300V stages were used for the X, Y, and Z Axes, respectively. Table 2.1 details the high-accuracy and precision specifications of the three stages (less than 1 micron motion error) , along with their respective range of motion. The motion control of these stages is performed using an XPS-RL universal motion controller.

Table 2.1: The Specifications of the X, Y, and Z stages from Newport.

	X-Axis	**Y-Axis**	**Z-Axis**
Type	ILS100BPP (SN B196038)	ILS150BPP (SN B192842)	IMS300V (SN B225468)
Range (mm)	100	150	300
Min Incremental Motion (μm)	1	1	0.3
Accuracy (μm)	$\pm$0.8	$\pm$1.5	$\pm$3.5
Bi-directional Repeatability (μm)	$\pm$0.4	$\pm$0.45	$\pm$0.2

2.3 Design of Processing Cell and Workpiece Holder

The design of the processing cell was structured in three layers, as shown in figure 2.3. The first layer contains the workpiece holder, counter-electrode, and electrolyte, while the second layer is dedicated to housing fresh electrolyte for circulation, facilitated by a peristaltic pump. The addition of the third layer serves as a safety measure, preventing electrolyte leakage or spillage. This layer is connected to the XY stages through an aluminum base. The workpiece holder was designed to be modular, allowing for easy removal and re-installation, particularly when adjustments to the immersion depth are required. The chosen cell material was Acrylic due to its corrosion resistance and affordable cost. The parts were cut and then assembled together using a glass melting chemical, as shown in figure 2.3 .

The base of the cell includes a fixture connected to a modular 3D printed workpiece holder and both connected using three plastic screws. Acrylic spacers of different thicknesses can be inserted between the workpiece holder and the acrylic fixture in case the immersion depth of the tool needs to be adapted.

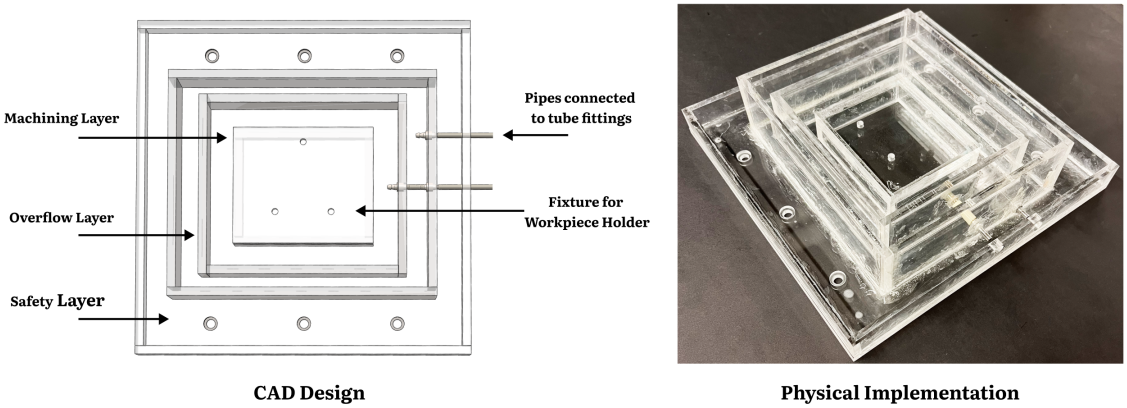

Figure 2.3: The Design and Physical Implementation of the Processing cell in SACE setup. The inner layer embodies a fixture that can be screwed to a modular workpiece holder. Barbed tube fittings were used to enable circulation of electrolyte between the middle layer and inner layer that contains the workpiece..

The workpiece holder is designed to prevent any motion of the workpiece during machining. A roller-slider pushes the workpiece in the y-direction preventing its motion and two opposite pins ensure the workpiece does not move along the z-direction. The processing cell also embodies the counter-electrode, a stainless-steel sheet that is folded and inserted in the inner machining layer of the cell. The electrolyte is first poured into the inner machining layer of the cell, where the level of the electrolyte should be at a level of around 1 mm from the surface of the workpiece for an immersion depth of 1 mm.

A fixed-flow rate (9.28 ml/min) peristaltic pump is used to provide a circulation system for the electrolyte. A barbed tube fitting was inserted at the bottom of the middle layer to collect the electrolyte and continuously inject fresh electrolyte into the inner layer through another barbed tube fitting attached at the lower level of the inner layer. This step is critical to ensure the electrolyte level is maintained in the machining zone.

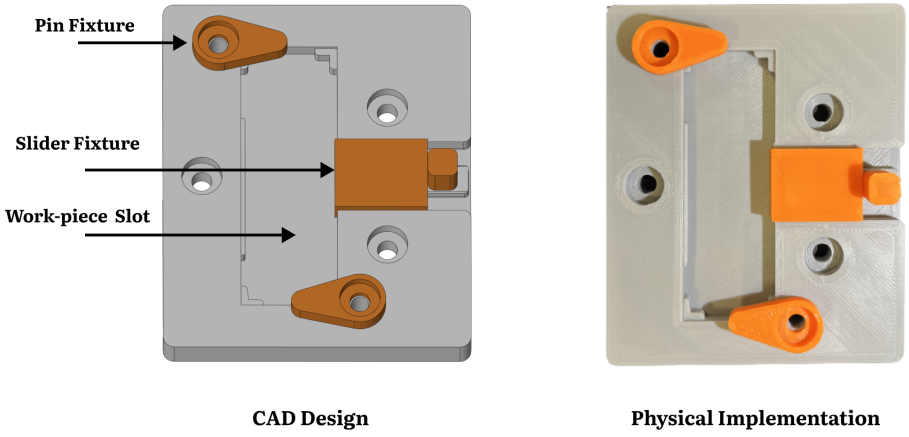

Figure 2.4: The 3D printed design and physical implementation of Workpiece Holder.

2.4 Design of Electrical and Control System

In this section, the design of the electrical and electronics systems of SACE setup are presented. The technical specification and properties of the different components, including the motor controllers, XPS-RL motion controller, dSPACE data acquisition board, and the printed circuit boards, are presented. An illustration of the components and used signals in SACE machine is shown in figure 2.5. A data Interface box was designed in-house and embodies three designed PCBs and two motor controllers. P1 is the XPS Plugin Board that gives access to the Analog and Digital IOs of the XPS motion controller. P4 is the Connection Hub which connects these signals to P2 (Dspace plugin board). The last connects to the dSPACE data acquisition board. Furthermore, this box carries two output signals to the machining head: A control signal to the linear motor (BEI Kimcoe LA10-12-027A voice coil actuator) and a control signal to the rotary motor (EC 32 flat), as well as an input signal from the machining head (optical sensor signal to indicate displacement). The motion controller and dSPACE board are both wired to a PC monitor where different softwares were used for signal control (Simulink/Controldesk and XPS software via TCL script).

2.4.1 Design of Data Interface Unit

The data communication unit, shown in Figure 2.6, is where all the communication between the different components of the system take place. It contains the controller for the voice coil actuator (ESCON 50/5), the controller for the rotary motor (DEC 50/5), and three PCB boards: the XPS plugin board, the DSPACE plugin board, and the main connection board. The XPS and dSPACE plugin boards connect the main connection board to the XPS-RL controller and DSPACE board, respectively. The last is interfaced with Simulink.

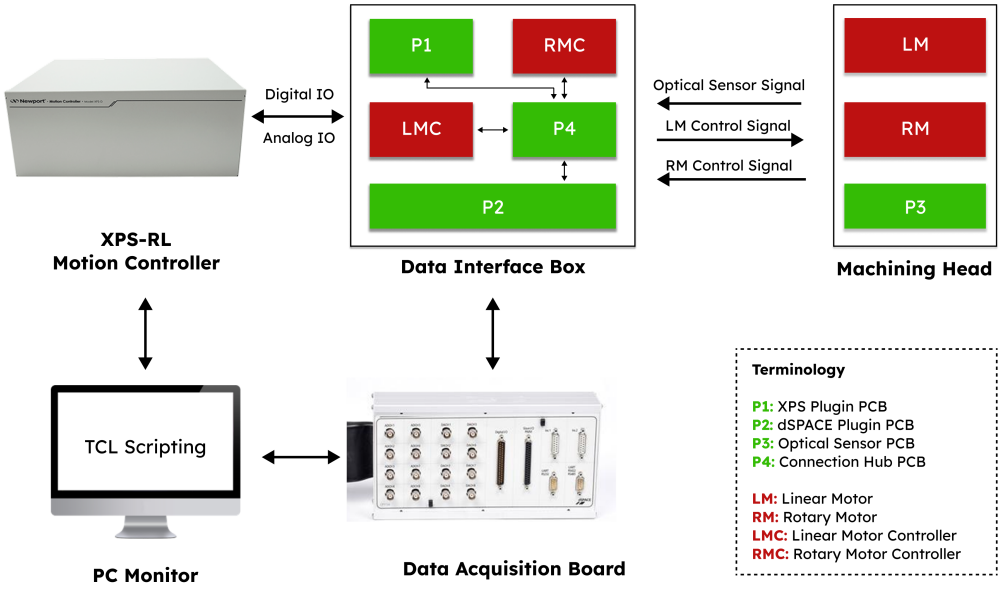

Figure 2.5: The electrical system and signal directions in SACE machine

2.4.2 Design of Control Circuit of Linear Motor and its Amplifier

The machining head embodies a linear voice coil actuator ((BEI Kimcoe LA10-12-027A) that is able to move the tool along the z-direction. This actuator is controlled (current control mode) by a maxon motor controller (409510 ESCON 50/5). To do that, an analog volatge signal is sent to ESCON through pins 1 and 2 of its Analog IOs (J6), and a corresponding current is outputted to the voice coil actuator. An analog output signal from ESCON is used to know the actual current that is being sent to the voice-coil (pin 6 of J6). The ESCON also requires a digital Enable, connected to pin 2 of its Digital IOs (J5). Finally, the wires of the actuator are connected to pins 1 and 2 of the Motor signals (J2). The connections to ESCON are shown in figure 2.7.

In order to read the current from ESCON, a conversion factor was applied. Knowing that the nominal current I of the system at peak force is 2.28 A and the maximum voltage is 4V, then the conversion ratio from Voltage to current is 2.28/4 and hence the current can be calculated using equation 2.1

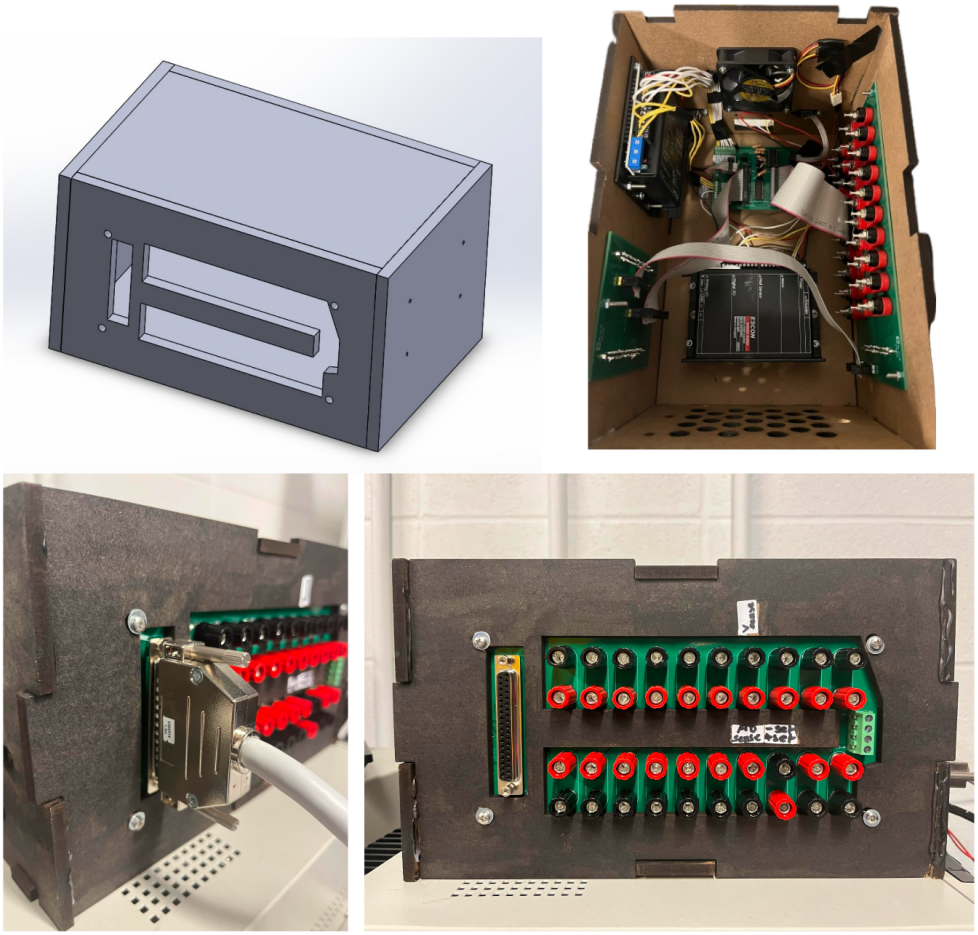

Figure 2.6: The Data Interface Unit that embodies the PCBs and motor controllers

$$I_{vc} = \frac{2.28}{4} * V_{vc} \tag{2.1}$$

The force exerted by the voice coil on the system can be calculated by multiplying the current with the force sensitivity of the voice coil k_f as in equation 2.2

$$F_{vc} = k_f * I_{vc} \tag{2.2}$$

The datasheet of the used voice coil actuator is included in the appendix.

Signal	Voltage Range
+Set,-Set	−10,+10 V
AO	−4,+4 V
Digital Enable	+2.4,+36 V

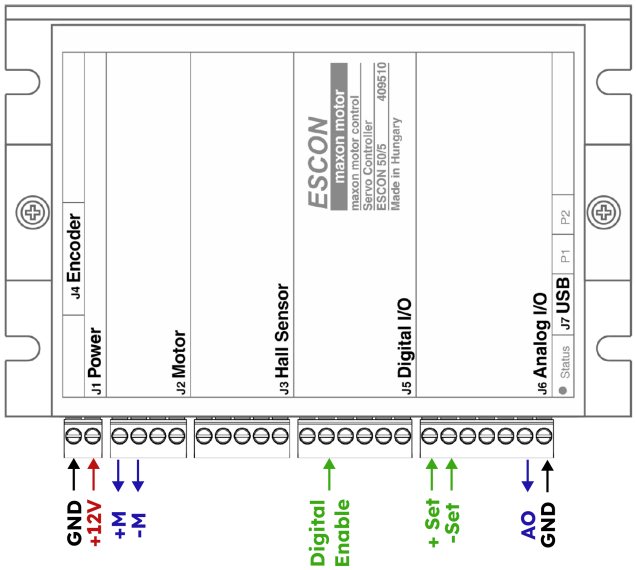

Figure 2.7: The input and output connections to ESCON

2.4.3 Design of Printed Circuit Boards (PCBs)

PCBs are essential elements in any system, as they integrate different functions and connect the components of a system allowing for a structured communication among them. In this section, the design and working principle of four different PBCs is detailed.

Design of XPS Plugin PCB

The XPS plugin board, shown in figure 2.8, connects the XPS-RL motion controller to other components in the system through two VGA connectors.

The used motion controller GPIOs (General Purpose Input Outputs) are GPIO3 and GPIO4 and their general I/O layout is shown in table 2.2. GPIO3 is an extended digital I/O connector with 8 digital inputs and 8 digital outputs with a minimum and maximum voltage outputs of 2V to 30V respectively. GPIO4 is an extended analog I/O connector with 8 analog inputs having a voltage range of ±10 V and 8 analog outputs with a configurable voltage scale of ±5 V, ±10 V, or ±12.288 V. The pin-out and actual soldered PCB is shown in figure 2.8. This board was used for two main

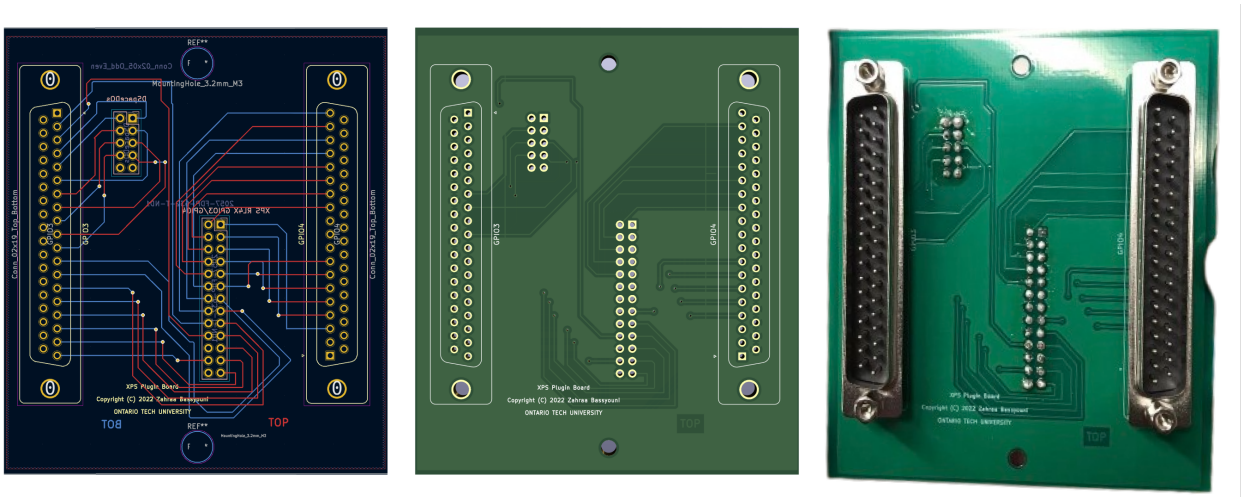

(a) (b) (c)

Figure 2.8: XPS Plugin Board. (a) Board Design on KiCad. (b) 3D View on KiCad. (c) Physical Implementation of PCB with soldered component.

reasons. The first reason is that it connects the digital triggers of 6 different signals for SACE machine using the DIOs of its GPIO3. These signals are the Enable trigger for Voice-coil actuator driver, the trigger of machining voltage, trigger of Pulsed Voltage, and the Brake, Direction, and the Disable signals of the rotary motor driver. The detailed connections of the signals is shown in table 2.4. The other purpose of this board is to read the analog signal coming from the machining head (Voltage of the optical sensor that indicates the displacement of the head), and to write analog signals to control two signals: the Speed of the rotary motor and the Force applied by the voice coil motor. The three analog signals connected to GPIO3 using the XPS plugin board are detailed in table 2.3.

Design of dSPACE Plugin PCB

The dSPACE plugin board, shown in figure 2.9 connects the dSPACE controller to the other components in the system. It has a 26 pin flat cable that connects signals with the connection hub PCB, which are in turn connected to the dSPACE board through 20 binding post connectors and banana-to-BNC plugs. These signals are:

- Vsense: Optical Sensor Signal (ADC)

Table 2.2: The general IO connectors of GOPI3 and GPIO4 of XPS-RL. Full Table can be obtained from page 235 in XPS-RL Users Manual.

GPIO3		**GPIO4**	
Pin Number	**Function**	**Pin Number**	**Function**
4	TTL Input 1	3	Analog Output 1
5	TTL Input 2	4	Analog Output 2
6	TTL Input 3	5	Analog Output 3
7	TTL Input 4	6	Analog Output 4
8	TTL Input 5	7	Analog Output 5
9	TTL Input 6	8	Analog Output 6
10	TTL Input 7	9	Analog Output 7
11	TTL Input 8	10	Analog Output 8
12	O.D. Output 1	12	Analog Input 1
13	O.D. Output 2	13	Analog Input 2
14	O.D. Output 3	14	Analog Input 3
15	O.D. Output 4	15	Analog Input 4
16	O.D. Output 5	16	Analog Input 5
17	O.D. Output 6	17	Analog Input 6
18	O.D. Output 7	18	Analog Input 7
19	O.D. Output 8	19	Analog Input 8

- +Set,-Set: Control Signal for Linear motor in machining Head (DAC)
- AOsense: Current representation signal of the voltage sent to the voice coil (ADC).
- Force: the Force signal used for a zero-displacement machining mode (ADC)

Furthermore, this PCB has a screw terminal that enables the connection of four external Analog inputs to the dSPACE board for data acquisition. And finally, the PCB enables connecting eight DI/O pins between dSPACE and XPS through another

Table 2.3: The detailed layout of the connections between the Assigned digital Signals for SACE Machine and GPIO3 of the XPS Controller. I/O is the name of the IO signal used, XPS Pin is the pin number on the dB37 connector of GPIO3, XPS FC is the pin number on the XPS-flat-cable (FC) connector on the Connection Hub PCB, dSPACE FC is the pin number on the dspace-flat-cable (FC) connector on the Connection Hub PCB, dSPACE pin is the pin number on the db37 Connection of dSPACE I/O, dSPACE IO is the I/O pin number as seen on Simulink interface, and finally the assigned signal describes the function of that connection. Note that RM means Rotary Motor and LM means Linear Motor.

GPIO3-SACE Connections						
XPS I/O	**XPS Pin**	**XPS FC**	**dSPACE FC**	**dSPACE Pin**	**dSPACE IO**	**Assigned Signal**
DO 1	12	13	17	9	**IO8**	RM Brake
DO 2	13	15	15	8	**IO7**	RM Direction
DO 3	14	17	13	6	**IO5**	RM Disable
DO 4	15	19	16	5	**IO4**	LM Enable
DO 5	16	21	18	3	**IO2**	Pulsed V Trigger
DO 6	17	23	20	2	**IO1**	Machining V Trigger

flat cable connector. These DI/O signals are for controlling the digital output of the system, and they mainly are:

- Turning On/OFF the rotary motor break
- Turning On/OFF the rotary motor Direction
- Turning On/OFF the rotary motor Disable
- Turning On/OFF the linear motor enable
- Turning On/OFF machining Voltage

Table 2.4: The detailed layout of the connections between the Assigned analog Signals for SACE Machine and GPIO4 of the XPS Controller

GPIO4-SACE Connections					
XPS IO	**XPS Pin**	**XPS FC**	**dSPACE FC**	**dSPACE BNC**	**Assigned Signal**
AO1	3	1	2	DACE3	**RM Speed**
AI7	18	10	21	ADC5	**Vsense**
AI8	19	16	23	ADC7	**Force**

- Turning On/OFF pulsed Voltage

The pin layout of these signals are detailed in table 2.3.

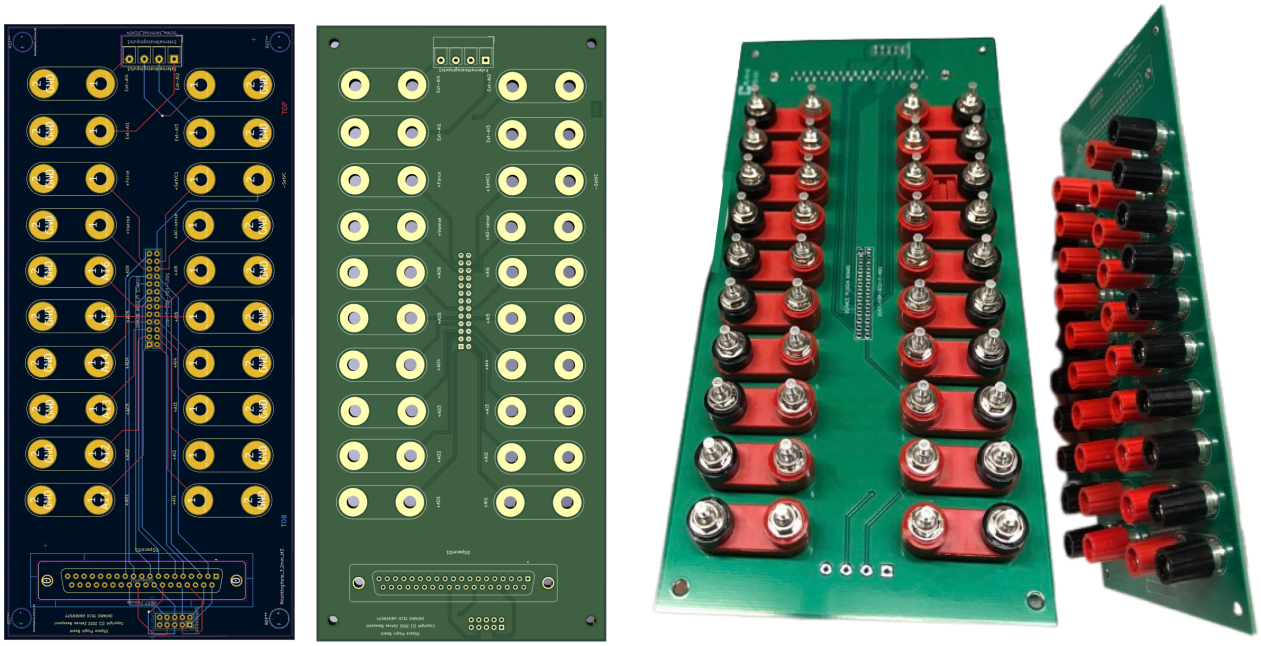

(a) (b) (c) (d)

Figure 2.9: dSPACE Plugin Board. (a) Board Design on KiCad. (b) 3D View on KiCad. (c) Front and (d) Back of PCB with soldered component.

Design of Optical Sensor PCB

This PCB, shown in figure 2.10, allows the communication between the machining head and the control system through a displacement sensor mounted on its back. The SFH9206 sensor, shown in Figure 2.11(a) detects the displacement of the tool through change in sensor's output voltage. Two Ref195 op-Amps were used to enable a precise and stable output voltage to the optical sensor. The SFH9206 optical sensor works according to the principle shown in Figure 2.11(b). The selection of the values for R_f and R_L has been done by applying Ohm's law as shown in equations 2.3 and 2.4

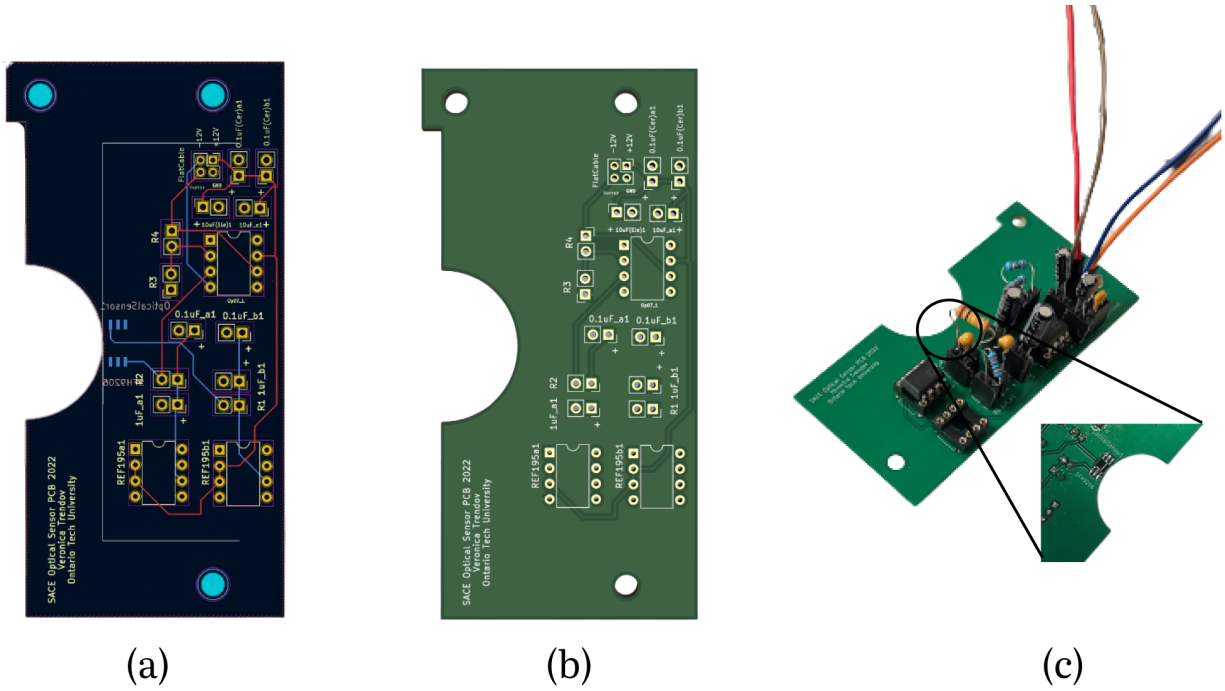

Figure 2.10: (a) Board Design on KiCad. (b) 3D View on KiCad. (c) Front and (d) Back of PCB with soldered component.

Furthermore, another factor was involved in choosing the optimal values of R_f and R_L that ensures the curve falls in the linear region where the heighest variation of voltage is achieved. A graph showing the relation between the photocurrent I_c as a function of the collector-emitter voltage V_{ce} is shown in figure 2.13. This curve shows a relation between the collector current I_c and the forward current I_f that affects the

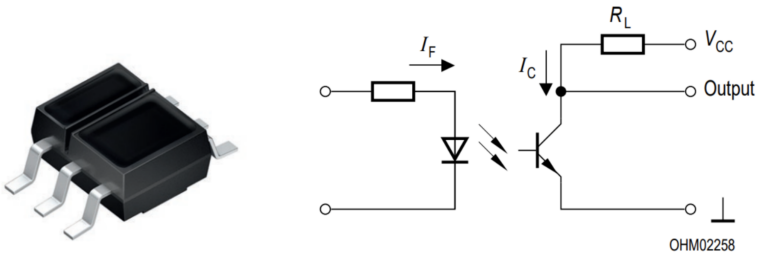

(a) (b)

Figure 2.11: SFH9206 Optical Sensor. (a) The actual physical sensor. (b) The Test Circuit for Switching and Response Time included in the sensor's datasheet.

behavior of the sensor. After applying equations 2.3 and 2.4, the selected values for R_f and R_L were 820 Ω and 18k Ω, respectively.

$$V_f = R_f I_f \tag{2.3}$$

$$V_{cc} = R_c I_c \tag{2.4}$$

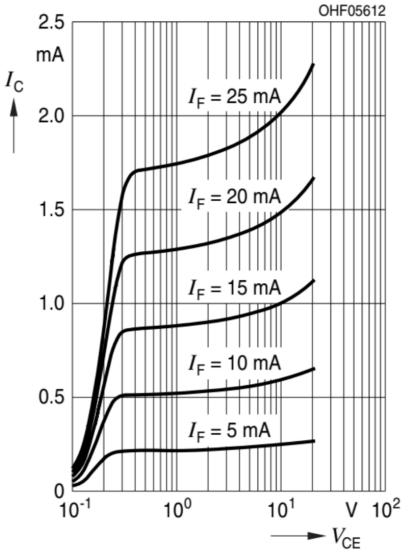

Figure 2.12: The relation between the collector-emmiter voltage V_{ce} and the collector and forward currents, I_c and I_f, respectively.

The obtained sensor has an accuracy of less than 4 microns and a precision of 1 to 2 microns.

Design of Connection Hub PCB

This PCB connects the components on the three other PCBS (Optical sensor PCB, XPS Plugin PCB, and dSPACE plugin PCB) to each other using connectors. It embodies a screw terminal that provides the required power to all other boards (+12V, -12V, and GND). It connects the XPS plugin PCB to the dSPACE plugin PCB through two flat cable connectors. Two Op-Amps (LM348) are used to maintain a low-current to the XPS Analog Inputs.

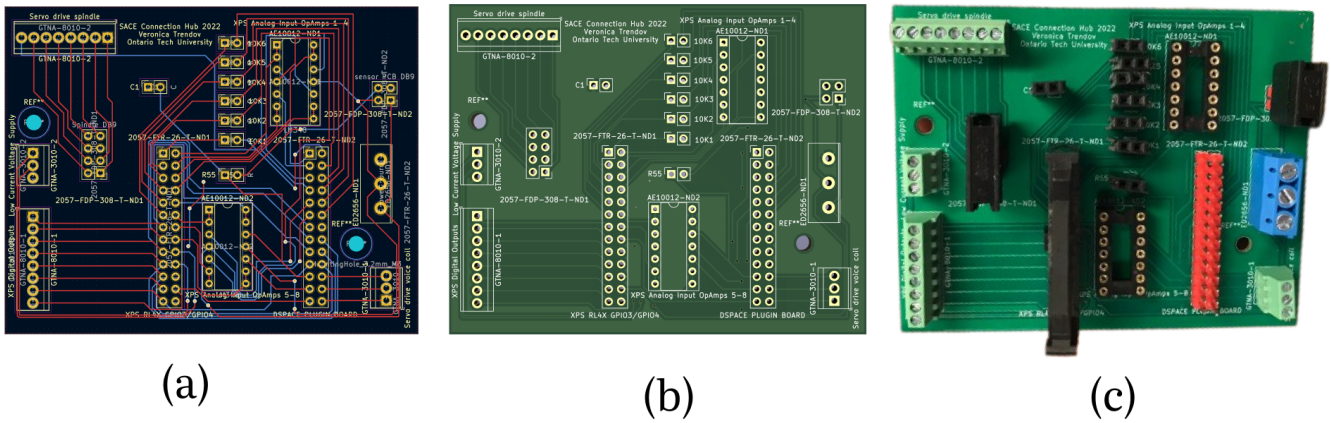

Figure 2.13: Conection Hub PCB. (a) Board Design on KiCad. (b) 3D View on KiCad. (c) Actual PCB with soldered component.

2.4.4 Design of Current Probe Adapter

The current signal during SACE machining was previously found to reveal significant information related to the quality of machining through indicating properties related to the formed gas film, including its formation time and lifetime. To retrieve the current signal during machining, the Tektronix current Probe needs to be connected to the BNC plugs of the dSPACE acquisition board. Due to incompatibility between the current probe tip and the BNC plug on the dSPACE board, an adaptor was designed in-house to connect both items.

. Figure 2.14 shows the Tektronix current probe and the needed signals to power it.

Figure 2.14: A layout describing the technical requirements for the current probe adapter. The current probe has 6 pads that need to be powered with specified signals, as indicated in the figure.

Two PCBs were designed using KiCAD. First, a 3D model with the required geometrical dimension and constraints was constructed using SolidWorks. The first PCB has to include the six Pads used to power the current Probe. The signals of these pads would come from a small screw terminal that links signals to the second PCB. This latter PCB has two female BNCs, a main screw terminal for the +12V and GND inputs, two voltage regulators with current limiting capabilities, and a small screw terminal used to transmit these signals to the first PCB. It should be noted that the 12V and 5V require a minimum current limit of 500 mA and 300 mA, respectively, and hence, suitable voltage regulators were used. Figure 2.15 shows the solidworks model of the current probe adapter and the two PCBS designed using KiCAD.

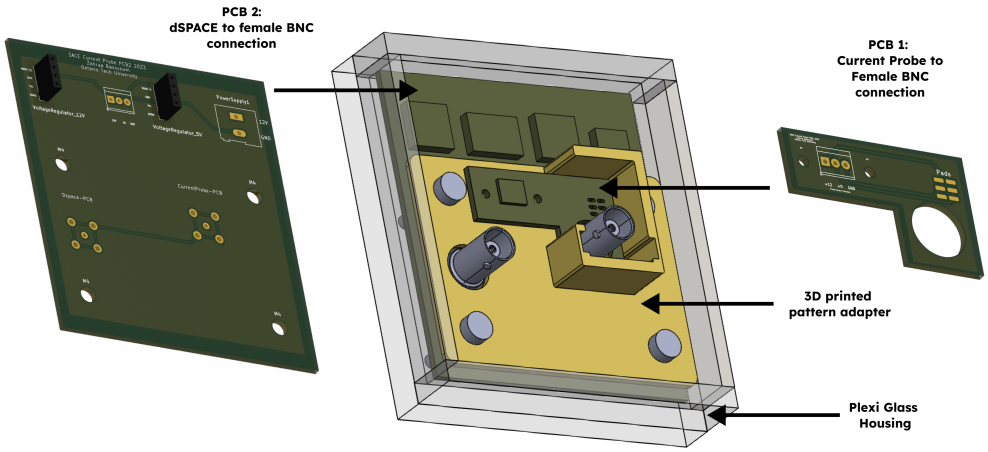

Figure 2.15: The designed current probe adapter using Solidworks for geometrical details and Kicad for electrical connections.

Chapter 3

Force-Feedback Control: Design and Implementation

As detailed in the previous chapter, the SACE machine is mounted on three motion stages and it is composed of different mechanical and electrical parts and systems. The work conducted in this chapter leads to the implementation of a force sensor. This force sensor relies on the implementation of a PID controller that can precisely detect the machining forces based on the zero-displacement measurement principal as depicted in Figure 3.1. The PID causes the flexible structure to be held in a fixed rigid position (converting it to a stiff structure). During machining, upon tool-substrate contact, the slightest contact force is detected by the deflection of the flexure. The voice coil actuator exerts an opposite force (F_{vc}) to compensate for the contact force (F_d) and keeps the structure at a fixed position.

Hence, this chapter starts with system calibrations and presents a piepeline of mathematical equations that enable an accurate measure of this force (F_{vc}). Then, a PID is designed and implemented on a model of the system, before implementing it on the physical structure. The chapter concludes with force-feedback drilling experiments to evaluate the designed forcesensor.

The sections of this chapter unfold as follows:

- *Section 3.1 System Calibrations The calibration process begins with the calibration of the optical sensor voltage that represents the displacement of the tool in*

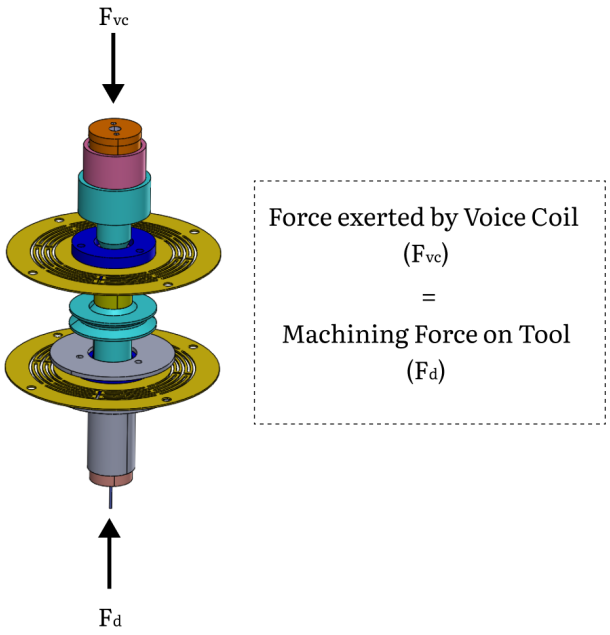

Figure 3.1: The concept behind the zero-displacement measuring principle.

the z-direction. Subsequently, the voice coil voltage was calibrated against the tool displacement by establishing a connection between the two parameters . This led to the last step: calibrating the voice coil voltage with the force it produces. This systematic calibration process enabled a precise and reliable method for measuring the force exerted by the voice-coil actuator. This section concludes with identifying and validating the stiffness of the system, a crucial step for the next section.

- *Section 3.2: PID Control Design Using System Modeling. This section presents a dynamic system modeling of the machining head. It is modeled in terms of its mechanical and electrical systems. A transfer function is obtained, and an open-loop response analysis was conducted after confirming the stiffness of the structure. This is followed by modeling the feedback signal (Optical sensor voltage) and obtaining the closed-loop response of the dynamic model. This modeling and control step was crucial to avoid any unwanted movements, imposed*

by an unstable controller on the tool/shaft assembly. Tool rotations were not taken into account during PID tuning or system modeling; nevertheless, they will impact system stability and introduce vibrations.

- *Section 3.3 Force-Sensor Implementation. This section describes the performance of the PID controller and describes the characteristics of the designed force sensor.*

- *Section 3.4 Results: Force-feedback Drilling Experiments This section presents experiments to evaluate the designed force sensor.*

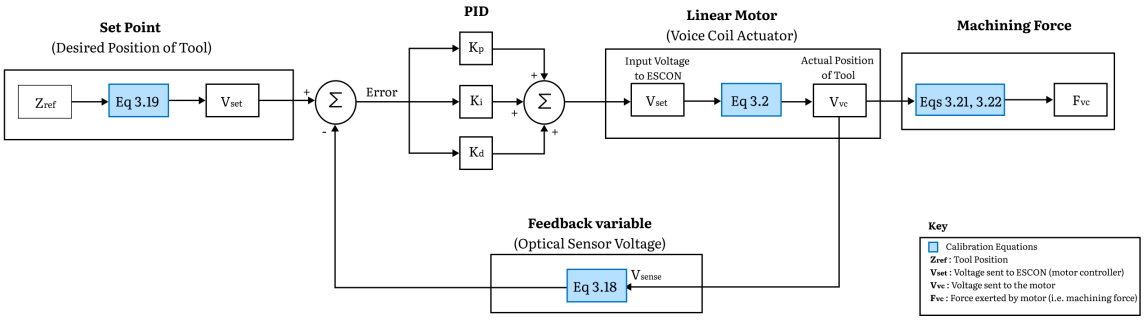

Figure 3.2: The role of calibrations in designing and controlling the system starting from setting a Reference set point all the way to identifying the machining forces acting on the system.

3.1 System Calibrations

This section covers system calibrations, a critical aspect in the development of a force sensor.

A diagram explaining the role of calibration tests in the development of the force-sensor is presented in figure 3.2. A calibration equation (Eq: 3.19) converts the desired stiff position of the tool to a reference voltage input from the voice coil. This reference voltage is then calibrated to the voltage representing the actual tool position (calibration Equation 3.18) which leads to evaluating the error in tool position that

is fed to a PID controller. The output of the controller is a voltage that is fed to the controller of the voice coil actuator (calibration Equation 3.2) which outputs the equivalent voltage sent to the voice-coil actuator. Finally calibration equation 3.22 gives us the force exerted by the voice-coil which is a representation of the machining force.

3.1.1 Optical Sensor Voltage

The SFH 9206 optical sensor is soldered to a PCB fixed on the middle plate of the machining head and facing the moving flexure plate (attached to the tool). When forces are applied on the tool, the flexure moves causing change in the sensor voltage. For a proper use of the sensor, a calibration curve was implemented. The Z-stage is moved down until the surface level is detected (expressed as a drop in voltage), and then small increments of 10 μm are applied while the corresponding voltage output from the optical sensor is recorded. The voltage was recorded for a total displacement of 1 mm. The calibration curve is depicted in Figure 3.3. The output voltage ranged between 6.86 V at the free position (tool not touching the work-piece) to 5.5 V after a 1 mm displacement. A linear fit equation was obtained that relates the voltage of the optical sensor expressed in [V] to the displacement of the tool [μm], as expressed in equation 3.1

$$V_{sense} = -0.001294z + 6.8553 \tag{3.1}$$

The model mismatch resulting from choosing a linear fit results in a mean absolute error of 27 mV. The accuracy of the optical sensor is less than 4 microns and its precision is 1 to 2micros (obtained experimentally).

3.1.2 Voice Coil Voltage

A calibration curve is needed to relate the input voltage of the voice-coil to the tool displacement. It should be noted that the voice coil voltage is limited by the ESCON

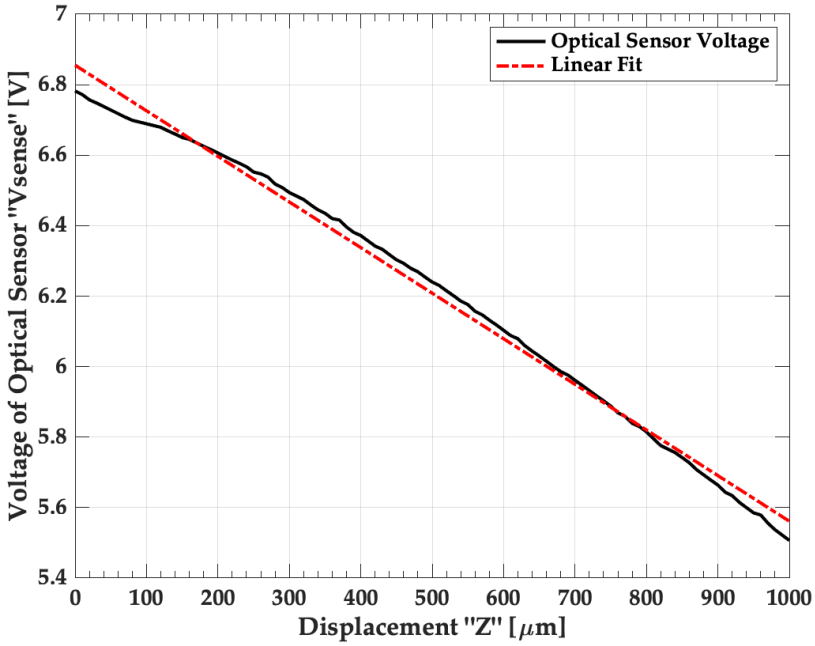

Figure 3.3: The calibration graph of the SFH 9206 sensor showing the change of the output voltage (V) as a function of the Displacement of the Z-stage (mm).

conversion rate (detailed in section 2.4.2) which was necessary to protect the structure from large movements that might damage the flexible structure.

An input sinusoidal voltage signal ranging from -2.5 V to 2.5 V was applied to the voice coil. The curve was plotted in Matlab, as shown in figure 3.4(a). The set point (V_{set}) that will drive the voice-coil was chosen in the region with the least amount of noise, as shown in 3.4(b). This represents a region where the voltage range is 0 to 2.5V

From the preceding linear fit, The equation that relates the voice-coil voltage to the output sensor signals is represented by equation 3.2.

$$V_{sense} = 0.14133V_{set} + 6.8303 \tag{3.2}$$

Where V_{set} is the voice coil voltage and V_{sense} is the optical sensor voltage.

Hence, equation 3.2 can be combined with equation 3.1 to determine the required voltage V_{set} needed by the voice coil to maintain a certain displacement of the tool z

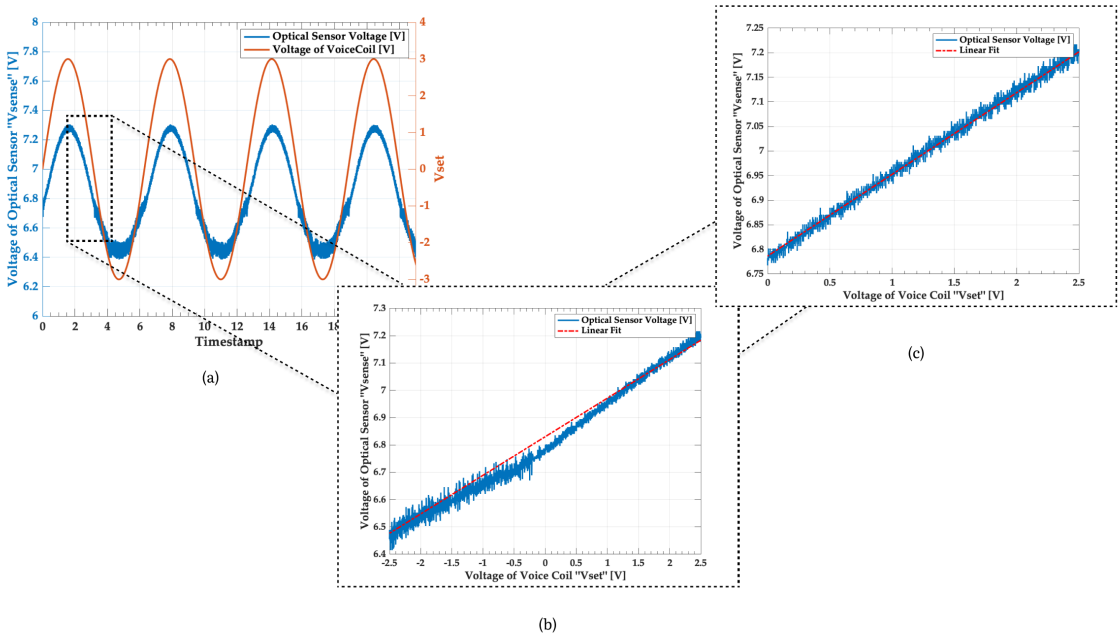

Figure 3.4: The variations of the optical sensor voltage(that represents the tool displacement) and the corresponding analog input signal (V_{set} of voice coil) as a function of time

in [μm], as represented in equation 3.3. The graph is plotted in figure 3.5.

$$V_{set} = -0.00916z + 0.0215 \tag{3.3}$$

3.1.3 Voice Coil Force

The Voice coil force can be measured using the Analog output of the ESCON controller. As mentioned in section 3.1.2, The input voltage to ESCON is converted to an output voltage that drives the voice coil with the proper current signal. The output voltage can be recorded from the Analog output pin of ESCON. Since the ESCON is capable of outputting a maximum voltage of 4V, the conversion rate between the input voltage to output voltage of ESCON is expressed as in Equation 3.4

$$V_{vc} = \frac{V_{set} \times 4}{10} \tag{3.4}$$

where V_{vc} is the analog output voltage from ESCON that represents the current being sent to drive the voice coil and V_{set} is the input voltage sent to ESCON. This can be

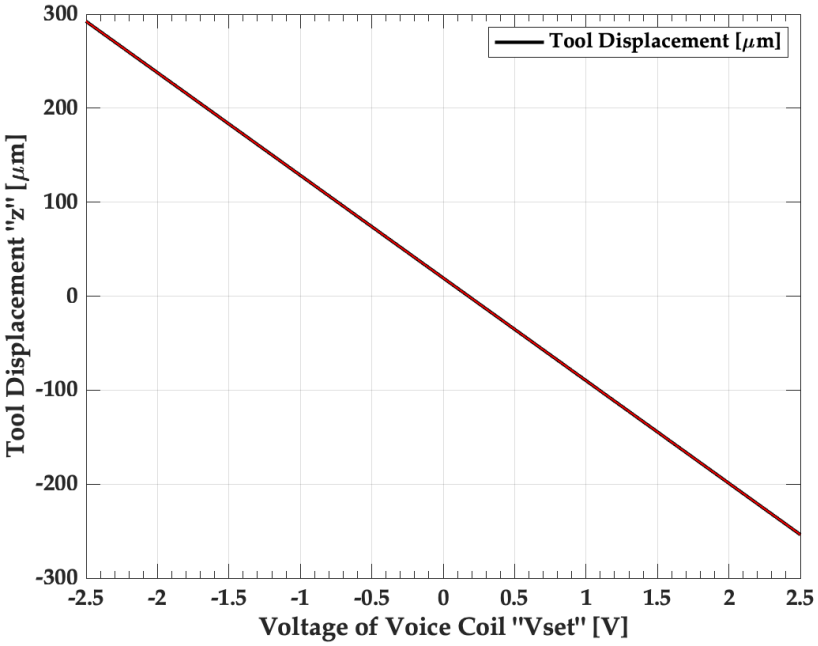

Figure 3.5: The tool displacement [μm] as a function of the applied voltage to the voice coil "Vset" [V]

seen in Figure 3.6 where a dynamic and a static test was made to display the relation between these two signals, respectively. The imposed limits on the voice-coil movement can be observed in Figure 3.6(b). When the applied voltage surpasses a specific threshold, the current sent to the voice-coil is restricted to safeguard the structure from extensive movement, as dictated by the ESCON conversion rate (explained in detail in Section 2.4.2). Consequently, the voltage saturates.

The current of the voice coil can then be calculated based on the applied conversion factor that was explained in 2.4.2 and is expressed in Equation 3.6

$$I_{vc} = \frac{V_{vc} \times 2.28}{4} \tag{3.5}$$

where I_{vc} is the current of the voice coil motor.

Finally, the force can be obtained based on the characteristics of the voice coil found in Appendix A, where the force is equal to the current multiplied by the force sensitivity k_f which is equal to 5.87 N/Amps.

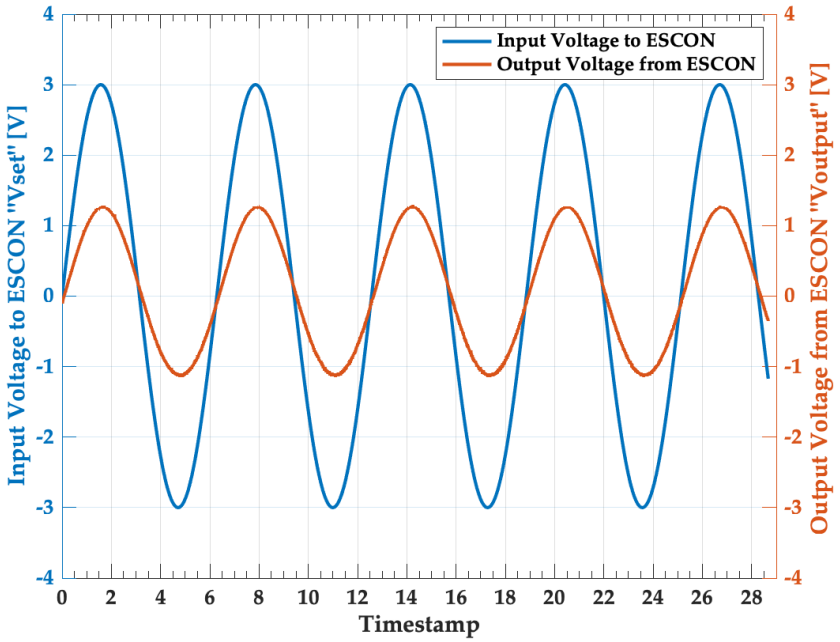

(a)

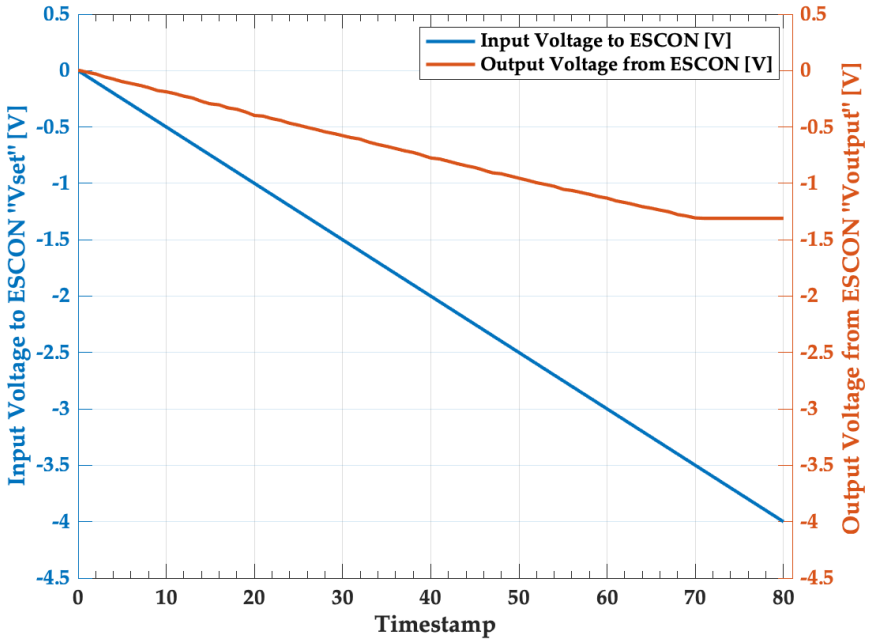

(b)

Figure 3.6: The relation between the analog input to ESCON and its output. (a) The recordings of a dynamic test with an analog input Voltage of -3V to +3V. (b) A static test with voltage increments of 50 mV

$$F_{vc} = I_{vc} \times k_f \tag{3.6}$$

3.1.4 System's Stiffness

Before applying the controller on the model, the stiffness of the system was determined and validated using two methods. In the first method, the voice coil actuator was used to exert a force on the tool, and the displacement of the system was recorded based on the optical sensor readings. In the second method, a dynamometer was used to measure the force exerted by the tool on the dynamometer surface, and then the displacement was recorded in the same manner.

Method 1: Exerting a Force on the Shaft using the Linear Motor

In the first experiment, a static test has been applied on the shaft, where increments of 50 mV were applied by the voice coil actuator, and the optical sensor voltage was recorded for each step. Figures 3.7(a) and (b) present the corresponding Force vs shaft movement for positive and negative increments of the applied voltage, respectively. From these figures, the stiffness of the shaft was calculated to be around 10.4 N/mm.

Method 2: Exerting a Force by the Tool on a Dynamometer Surface

In this method, the dynamometer was used to measure the force exerted by the shaft on the system while the shaft moved with the aid of the z-stage. For calibration purposes, a total of five tests were done, and each test had six experiments. During each experiment, different masses (55 up to 501 grams) were gradually added on the dynamometer surface, and for each mass, the shaft was moved downward with a certain displacement. The masses were used to calibrate the voltage-force relation. Bases on that, the corresponding force was recorded for every shaft movement. The results of test 1 are shown in figure 3.8. The stiffness was found to be around 10.8 N/mm.

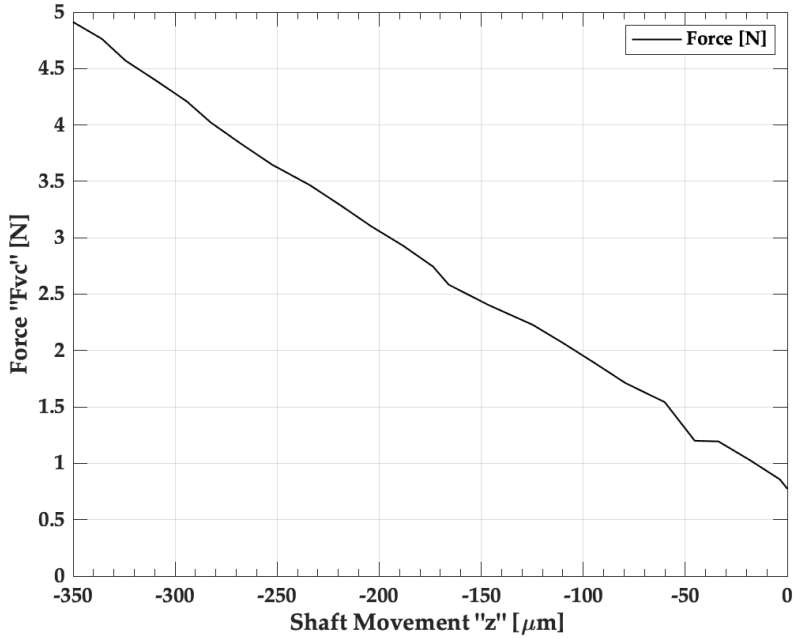

(a)

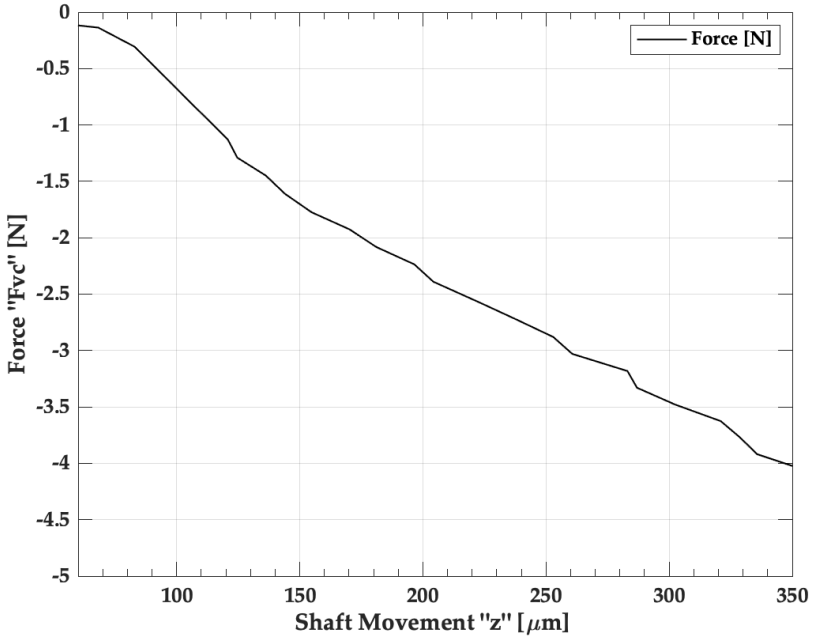

(b)

Figure 3.7: The variations of the voice-coil Force as a function of shaft movements. (a) Test applied using positive increments of the voice-coil voltage. (b) Test applied using negative increments of the voice-coil voltage.

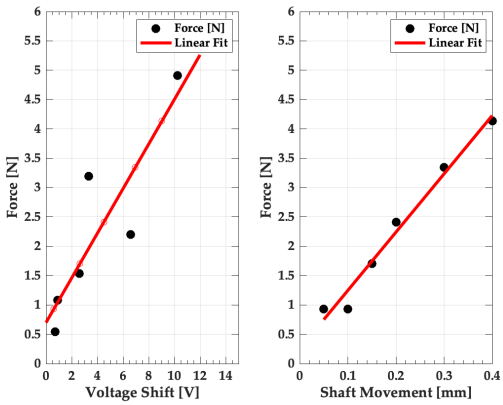

Figure 3.8: The variations of the Force measured by the Dynamometer as a function of the voltage shift (left) and The variations of the Force measured by the Dynamometer as a function of the voltage shift (right)

The two used methods showed similar results for the stiffness determination. Furthermore, a previous FEA analysis conducted on the used flexure of the machining head was found to be 5.65 N/mm (a total stiffness of 11.3 N/mm due to the presence of two flexures). Hence, the used stiffness in the modeling of the system was chosen to be 10.8 N/mm.

3.2 PID Control Design Using System Modeling

In this section, the dynamic model of the system is introduced, including its mechanical and electrical model. The system is mechanically modeled as a second order system of mass m, stiffness k, damping b, a force F_{vc} applied by the voice coil actuator, and a disturbance force F_d . Its electrical model is represented by an electric circuit of inductance L, resistance R, and an induced electromotive force V_e.Based on that, a transfer function that maps the input of the system (Voice Coil Voltage) to the output (Displacement of the Tool) is developed using Simulink blocks. The section concludes with open loop and closed-loop response analysis.

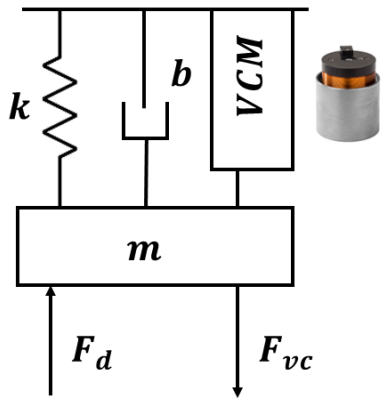

Figure 3.9: Dynamic Model of the system. A stiffness of known k represent the two flexible flexures, m represents the mass of the tool and its support, b represents the damping of the flexures, F_{vc} represents the force exerted by the voice coil actuator, and F_d represents the forces of disturbance.

3.2.1 Mechanical Model

The structure holding the tool is modeled as a second order system of mass m and a stiffness k, as shown in figure 3.9. The system does not include modeling of gravitational forces since the structure is supported by the voice coil actuator and is not freely suspended. The stiffness k was found to be 10.8 N/mm (detailed in section 3.1.4). The second order system is represented by the model in Equation 3.7:

$$m\ddot{z}(t) + b\dot{z}(t) + kz(t) = F_{vc}(t) - F_d(t) \tag{3.7}$$

Where F_{vc} is the force exerted by the voice coil, F_d represents disturbance forces exerted on the load (machining tool in this case), k is the stiffness of the flexure, and z is the displacement of the tool in the vertical direction with respect to the base of the machining head. The force F_{vc} is directly proportional to the current and is represented by Equation 3.8:

$$F_{vc}(t) = k_f I(t) \tag{3.8}$$

where k_f is the force sensitivity of the voice coil and I is the current passing through the coil. Given that, the derivative of the displacement x can be represented by the

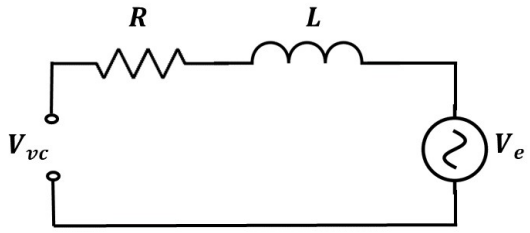

Figure 3.10: The electrical circuit of the voice coil actuator

velocity v of the system as in Equation 3.9:

$$\ddot{z}(t) = \dot{v}(t) \tag{3.9}$$

Combining equations 3.7 to 3.9, the mechanical model of the system can be written as Equation 3.10

$$m\dot{v}(t) + bv(t) + k\int v(t) = F_{vc}(t) - F_d(t) \tag{3.10}$$

Applying laplace Transform on Equation 3.10 results in the velocity of the system represented in Equation 3.11

$$v(s) = \frac{F_{vc}(s) - F_d(s)}{ms^2 + bs + k}s \tag{3.11}$$

Similarly applying Laplace on Equation 3.8 results in the force exerted by the voice coil as represented in Equation 3.12:

$$F_{vc}(s) = k_f I(s) \tag{3.12}$$

3.2.2 Electrical Model

The electrical model of the system is shown in Figure 3.10. The voltage balance equation can be represented by Equation 3.13:

$$V_{vc}(t) = RI(t) + L\frac{dI}{dt} + V_e(t) \tag{3.13}$$

Where $V_{vc}(t)$ is the input voltage to the voice coil actuator, R is the resistance of the voice coil, L is the inductance, and $V_e(t)$ is the induced electromotive force. Given that $V_e(t)$ is equivalent to the product of the back electromotive force constant k_{emf} and the velocity of the system v, Equation 3.14 can be written as follows:

$$V_e = k_{emf}\dot{z}(t) \tag{3.14}$$

Combining Equations 3.13 and 3.14, the electrical model of the system can be expressed as shown in Equation 3.15

$$V_{vc}(t) = RI(t) + L\frac{dI}{dt} + k_{emf}\dot{z}(t) \tag{3.15}$$

Applying laplace transform on Equation 3.15, results in the laplace transform of the current I(s) as follows:

$$I(s) = \frac{V_{vc}(s) - V_e(s)}{Ls + R} \tag{3.16}$$

and the laplace transform of the induced electromotive force as follows:

$$V_e(s) = k_{emf}v(s) \tag{3.17}$$

3.2.3 Transfer Function

The mechanical and electrical models of the system are combined, and four equations are used in the modeling of the actuator system. Equation 3.18 represents the velocity of the system v as follows:

$$v(s) = \frac{F(s) - F_d(s)}{ms^2 + bs + k}s \tag{3.18}$$

The force exerted by the voice coil F_{vc} is represented as a function of the voice coil's force sensitivity k_f and the current I as shown in Equation 3.19.

$$F_{vc}(s) = k_f I(s) \tag{3.19}$$

The induced electromotive force V_e is represented as a function of the back electromotive force constant k_{emf} and the velocity of the system as shown in Equation 3.20

$$V_e(s) = k_{emf} v(s) \tag{3.20}$$

The current I is represented in terms of the voltage applied to the voice coil V_{vc} and its induced electromotive force V_e,and the coil's inductance L and resistivity R as shown in Equation 3.21.

$$I(s) = \frac{V_{vc}(s) - V_e(s)}{Ls + R} \tag{3.21}$$

Equations 3.18 to 3.21 were used in the modeling of the transfer function of the system using Simulink Blocks, as shown in Figure 3.11(a). The Output is the displacement of the system Z in mm, or the position of the tool, V_{vc} is the input voltage to the voice coil actuator, m is the mass of the system, L is the inductance, R is the resistance of the voice coil, k_{emf} is the back electromotive force constant, k_f is the force sensitivity of the voice coil, and v is the velocity of the system. The properties of the system are summarized in Table 3.1.

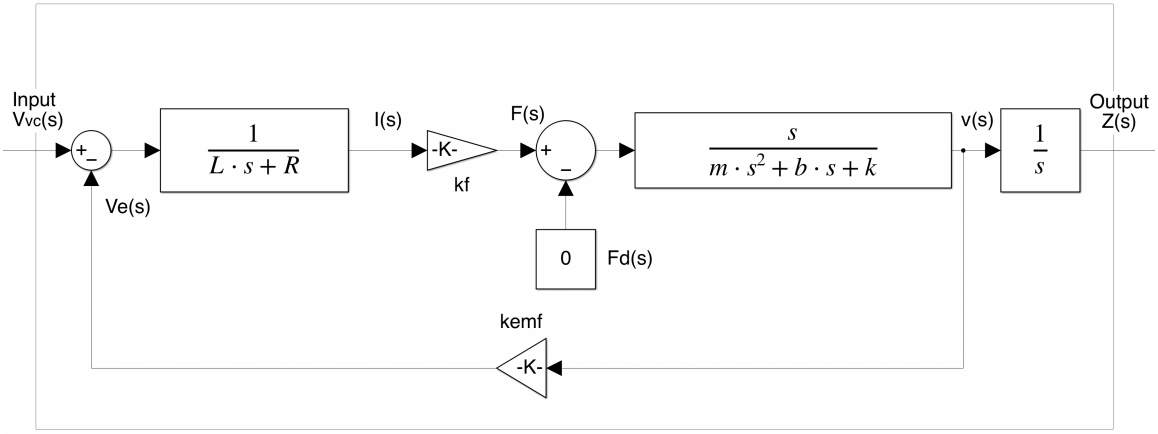

Figure 3.11: The Dynamic modeling of the system representing its mechanical and electrical components. This model will be later used as the actuator model in section 3.2.6.

Table 3.1: The properties of the modelled system

Symbol	Description	Value
m	Mass	276 g
k	Stiffness of flexures	10.8 N/mm
L	Inductance of Voice coil	3.05 mH
R	Resistance of Voice coil	11 Ω
k_{emf}	Back electromotive force constant	5.87 V/m/sec
k_f	Force sensitivity of the voice coil	5.87 N/amps

3.2.4 Open Loop Response

A step voltage was fed as an input to the model in Figure 3.11, and the recorded displacement was visualized in the graph of Figure 3.12. The graph shows a behavior of an under-damped system that oscillates for more than 2.5s before settling to a steady value.

3.2.5 Sensor Model

To conduct a closed-loop response analysis on the System Model, a sensor model was incorporated. The last represents the feedback of the tool's response to a step input, thereby obtaining the actual tool displacement. To achieve this, an optical sensor (SFH9206) was used. The sensor was soldered on the back of a PCB mounted on the machining head. This sensor detects micro displacements of the tool through outputting a voltage that is read through a data acquisition board. Using the Z-stage, the machining head that holds the tool was moved vertically downward until it touches the surface of a substrate fixed underneath it. After the tool detects the surface level, a total of 1 mm displacement was applied by increments of 10 μm, and the voltage was recorded for every increment. Figure /reffig:sensorfig2 shows the variation of the optical sensor voltage Vsense in [V] as a function of the displacement

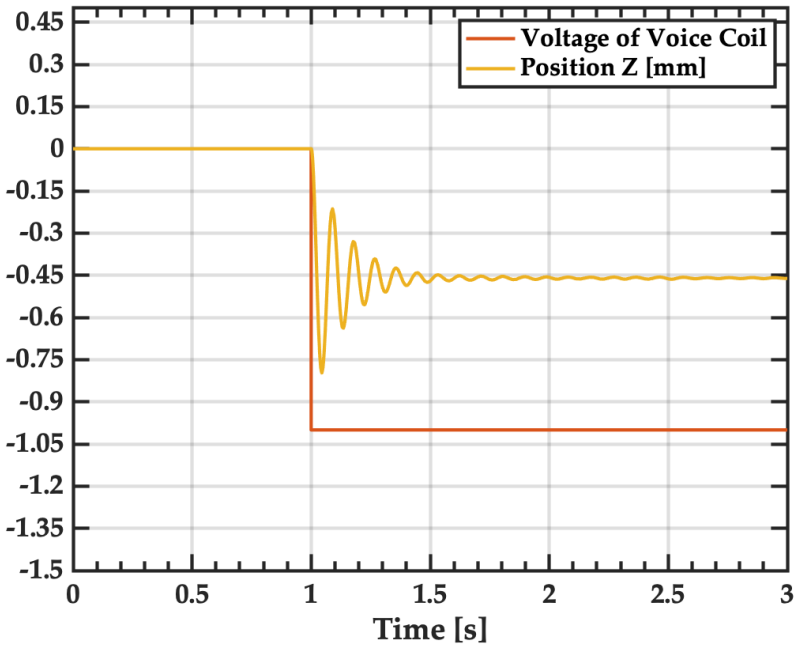

Figure 3.12: The system's model response to a step input. The graph indicates a displacement of around 0.46 mm for an applied voltage of 1 V.

of the tool Z in [mm]

Subsequently, the voltage-displacement equation was formulated as depicted in Equation 3.22 where V_{sense} is the output voltage from the optical sensor in V and Z is the displacement of the tool in mm. A sensor model was then obtained that transforms the displacement Z into its corresponding Voltage.

$$V_{sense} = -0.8875Z + 6.944 \tag{3.22}$$

3.2.6 Closed Loop Response

After modeling the system in terms of its actuator model G(s) and its sensor model H(s), a PID controller is implemented and tuned on the underdamped dynamic system model with the help of the PID block in Simulink. The different blocks used to model the system are illustrated in Figure 3.14. The input to the system is the Voltage applied to the voice coil V_{vc} expressed in [V] while the output is the position Z

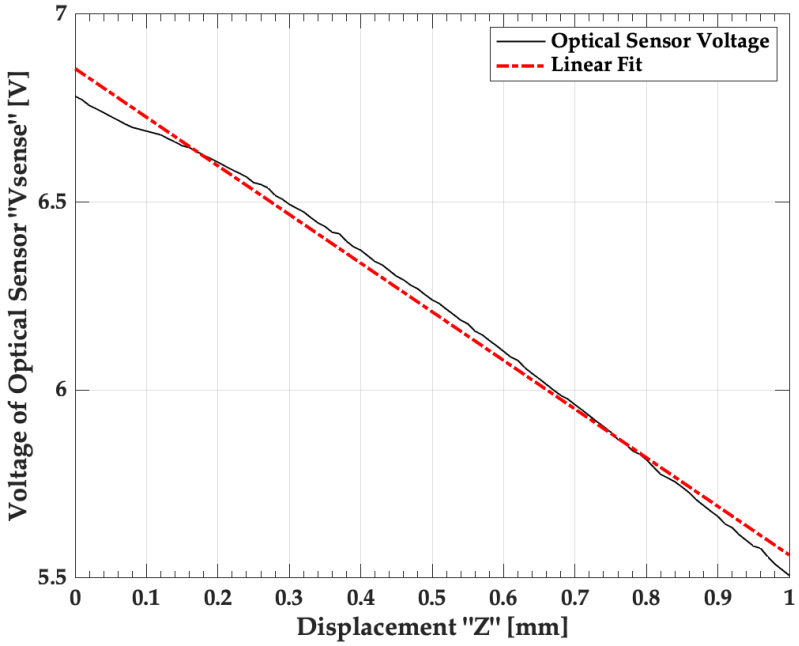

Figure 3.13: The optical sensor voltage readings as a funciton of tool displacement.

expressed in [mm]. The closed loop response of the model is shown in figure **??**.

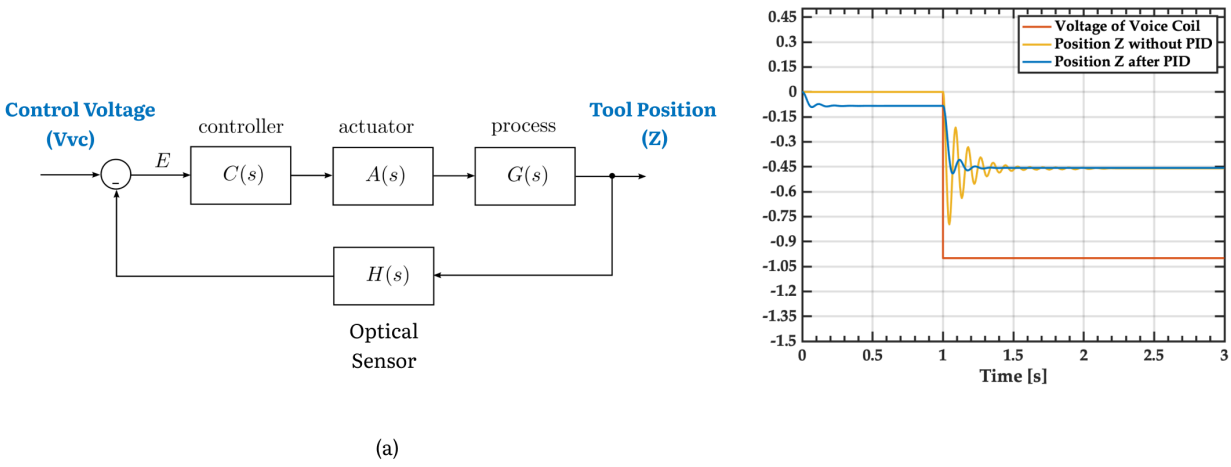

(a)

Figure 3.14: Controller Implementation. (a) The control model of the system expressed as consecutive blocks of the Controller C(s), the actuator A(s), the process G(s), and a feedback loop expressed in terms of the sensor H(s). (b) The closed-loop response of implementing the controller on the system model.

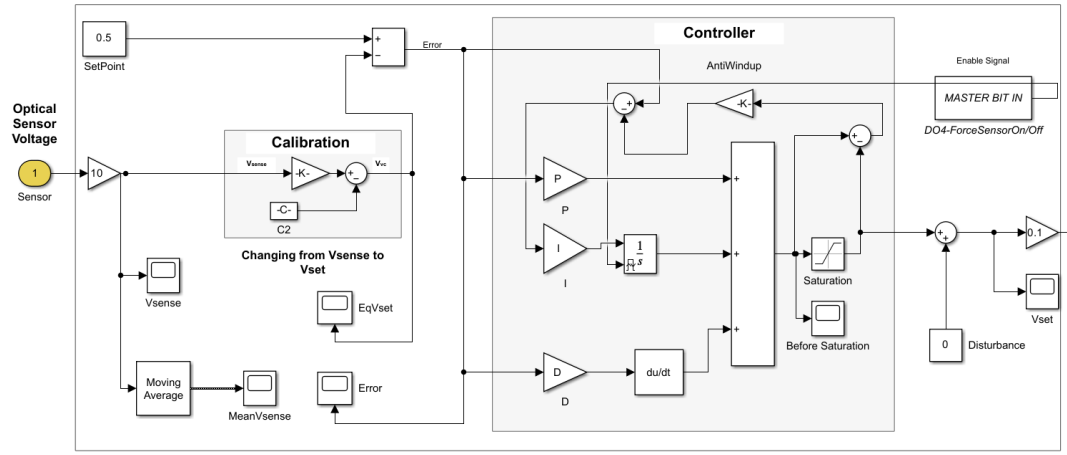

Figure 3.15: The Simulink Code used to apply the physical Implementation of the PID code on the SACE setup

3.2.7 Summary: System Modelling and Control

In this section design and development of a dynamic system model was presented and implemented on Matlab using Simulink Blocks. Subsequently, a PID model was applied and fine-tuned on the system. This process yielded initial control parameter values that played a pivotal role in ensuring the prevention of unintended movements that might potentially harm the flexible structure.

3.3 Force Sensor Implementation

As previously mentioned, the machining head should be able to operate in a zero-displacement mode. This means that the tool is held by the machine head structure in a fixed rigid position that can resist the external noise and sense small force disturbance.This mode is crucial to prevent surface damage and deteriorated machining quality. Hence, the PID controller was used for this purpose. Figure 3.15 shows the Simulink Blocks used to implement the controller on the SACE setup.

The PID controller was tuned according to the Ziegler-Nichols heuristic tuning technique, where initial values of k_P, k_I,k_D were set to 1, 0, and 0, respectively. Then k_P was gradually increased until the system shows sustained oscillations. Based on

that value, the ultimate gain k_U was set, and the oscillation period T_U was determined from the plot. Next, the following parameters were used as a starting point for tuning:

- $k_P = 0.6 \times k_U$
- $k_I = 2 \times k_P / T_U$
- $k_D = k_P \times T_U / 8$

Note that the PID was tuned in a dry experiment, and it behaved normally even after adding the fluid. Therefore, the effect of fluid damping is disregarded.

The response to a step input, shown in figure 3.16a, features a rise time of 100 ms and a zero-overshoot.

The implemented force sensor features an operating range spanning from -5 N to 5 N. To quantify the characteristics of the force sensor, the response to disturbance was plotted, as shown in figure 3.16. The force sensor has a response to disturbance time of 200 ms and an rms noise of 11.8 mN. In both plots, the moving average signal was used. .

3.4 Results: Force-feedback Drilling Experiments

To assess the effectiveness of the designed force sensor, holes with varying depths were drilled using the force-feedback approach. This involved creating four holes at a drilling depth of 100 μm, another four at 300 μm, and an additional four at 500 μm depth. All holes were drilled at the same machining conditions, as shown in table 3.2.

The force-feedback drilling technique was conducted as follows:

- The machining head is moved down at a speed of 5 mm/sec until it reaches an initial position around 2 mm before the surface level. Then the speed is lowered (50 μm/sec) until it reaches a starting position around 0.5 mm above surface level(zstarting).

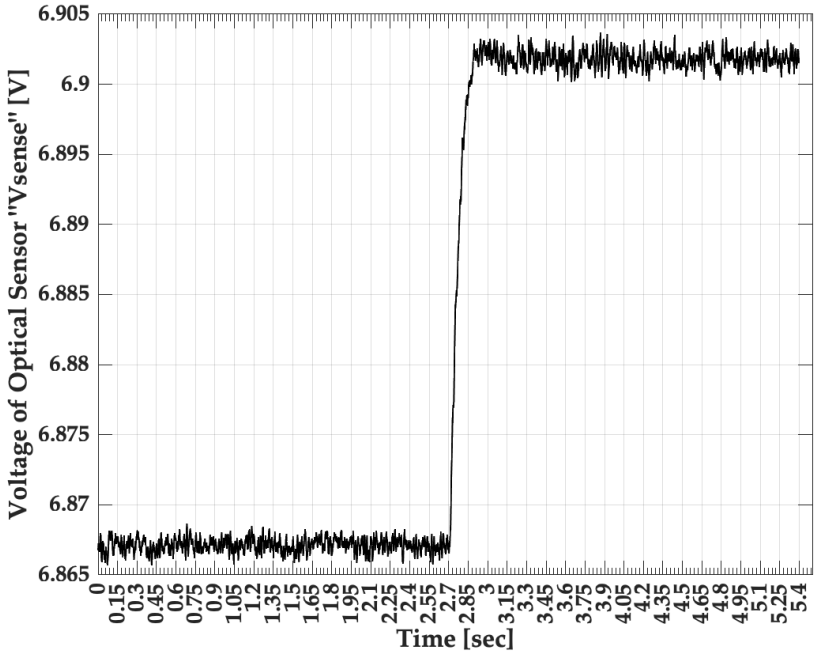

(a)

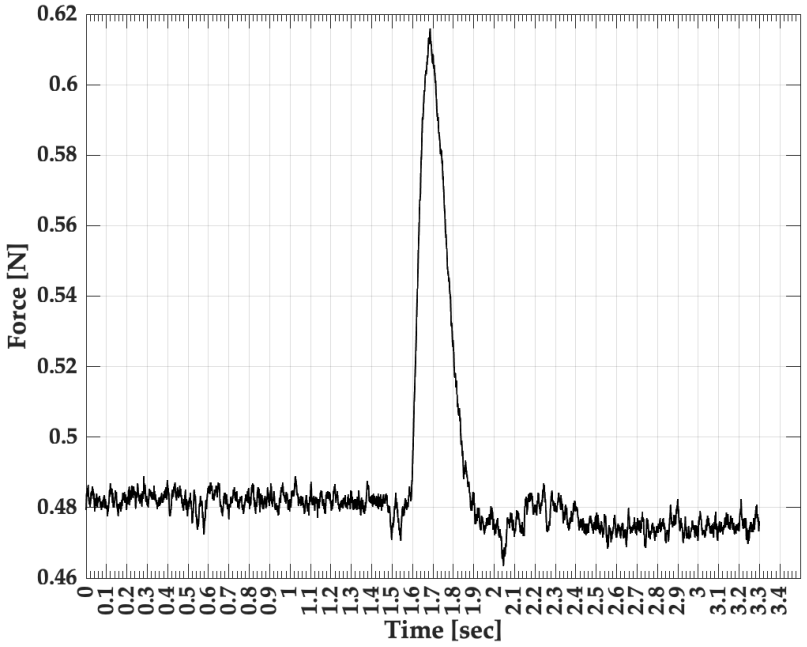

(b)

Figure 3.16: (a) The system's response to a step input. (b) The force sensor's response to disturbance plot. In both plots, the moving average signal was used.

Table 3.2: Machining Conditions for Drilling Experiments.

Machining Condition	Value
Feed-rate	3 μm/sec
Machining Gap	100 μm
Voltage High	34 V
Voltage low	15 V
Duty Cycle	90%
Period	2.5 ms
Electrolyte	30 wt% NaOH

- The optical sensor voltage signal is used to detect the workpiece surface level. While operating the machine head in the profilometer mode (PID controller off) the head is moved at a low speed of 10 μm/sec. When a voltage change of 5 mV is detected (as the tool touches the workpiece) the whole shaft is displaced upward and hence the optical sensor voltage changes indicating the tool-substrate contact.

- After the surface level is detected, the tool is moved upwards by a 50 μm. This gap is added to enhance the flushing of the electrolyte during machining.

- the machining voltage and the force sensor are then turned on, hence switching the head from profilometer to force sensor mode where the structure is converted from flexible to stiff rigid one. Then the tool moves at a specified feed rate until the whole depth is moved down by the z-axis. Throughout this downward movement, the force sensor measures the forces exerted on the tool, if they are greater than 200 mN, the downward movement stops and the Z-stage retracts upward by a distance of 10 μm. This movement will be referred to as a counteraction.

  The above methodology ensures minimal contact forces throughout the ma-

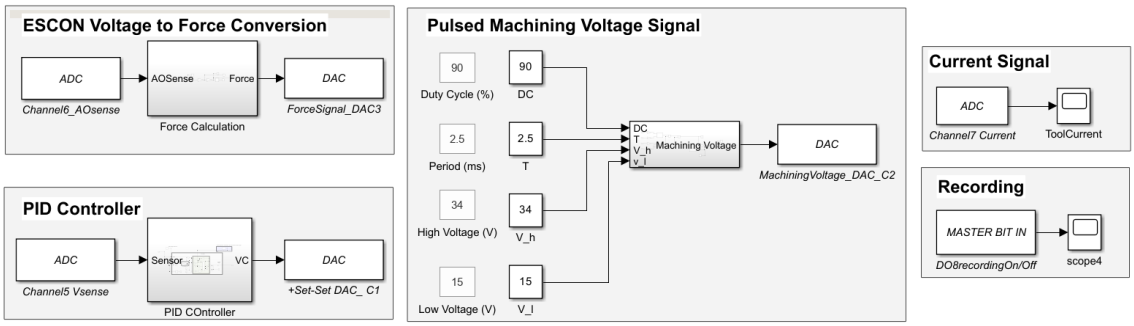

Figure 3.17: Th Simulink Code used to apply the PID controller on the SACE setup

chining of holes and enables the machining of deeper holes while preserving the quality and integrity of the hole. The Simulink Code that enables the reading and writing of Signals s shown in figure 3.17

As shown in Figure 3.18, when drilling 100-micron deep holes, most holes (three out of four) exhibited minimal counteractions, with no counteractions recorded. However, with an increase in drilling depth to 300 μm, the number of counteractions rose, averaging 12 per hole. When drilling even deeper, at 500 μm, the count of counteractions significantly increased to 62. These findings align with established SACE literature, which notes that as drilling depth increases, the Material Removal Rate (MRR) decreases, making the process more challenging due to complications in electrolyte flushing within the holes. Consequently, contact forces intensify with greater depth, leading to a higher number of counteractions by the system. Furthermore, the decreasing trend in the number of counteractions (hence reduced drilling time) with each subsequent hole can be attributed to the more stabilized heating (substrate and electrolyte temperature). This results in improved repeatability of the drilling results as more holes are drilled. Furthermore, there is a decreasing trend in the machining time as drilling proceeds for subsequent holes within each depth category. This result also confirms with literature findings that SACE process becomes more repeatable as drilling progresses. Also, the increase in tool-electrode and electrolyte temperature increases the MRR.

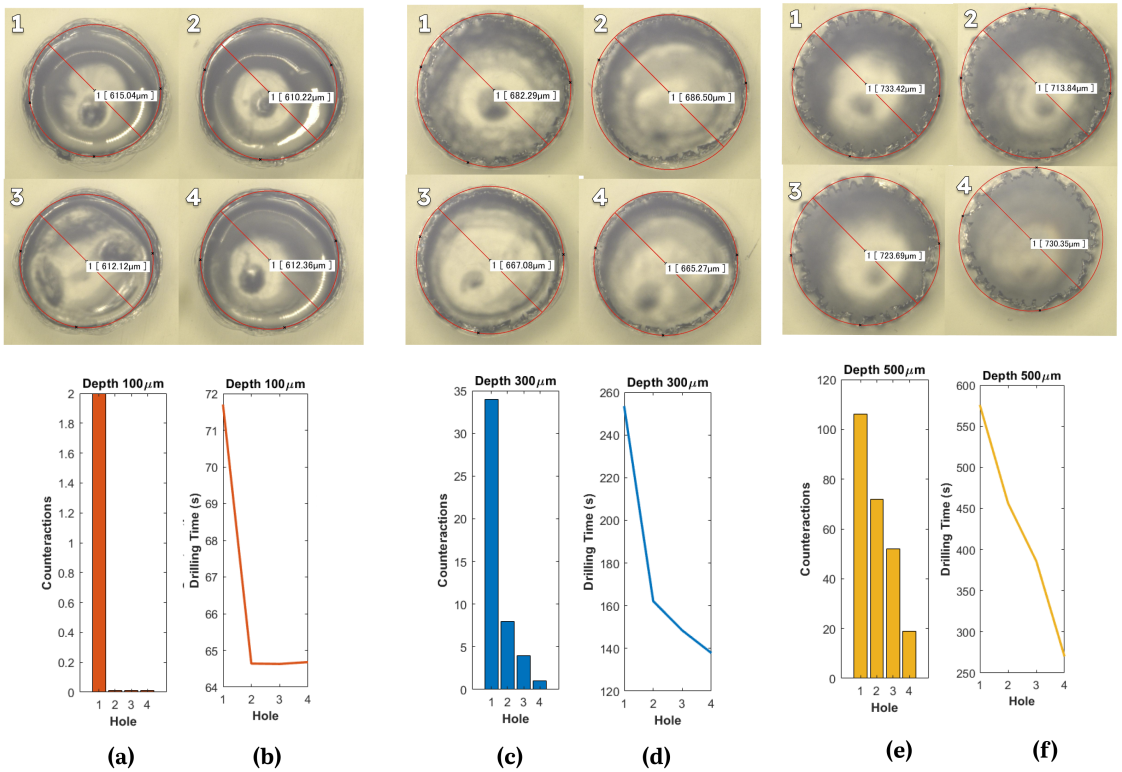

Figure 3.18: The number of counteractions and the drilling time for each Hole per each drilling depth.

Chapter 4

Machine Learning Application

Now that the tool-workpiece contact can be eliminated, different surface textures can be generated using SACE. The examination of the PID's effect involves assessing its capability to generate various textures. Subsequently, an ML application is conducted as a validation experiment to confirm the PID's effectiveness in creating diverse textures. In this chapter, a machine learning model was applied to predict the surface texture of machined holes for different machining conditions. The chapter begins with an overview of the experimental setup and procedure in Sections 4.1 and 4.2, followed by a discussion on the design of experiments in Section 4.3. Section 4.4 presents a data visualization of the collected dataset, and in Section 4.5, the classifiers used in this study are shown. The chapter culminates with the presentation of results in Section 4.6.

4.1 Experimental Setup

The setup used for the machine learning experiments is detailed in chapter 2. On the mechanical side, the machining head that holds the tool is mounted on the Z-stage of an XYZ cartesian system. The processing cell, on the other hand, is mounted on the XY stages and embodies the workpiece holder in a position just below the machining tool. The cell is connected to a pump that ensures a constant overflow of fresh electrolyte into the machining area. On the electrical side, the tool and counter-

electrode are connected to the negative and positive terminal outputs of a machining power amplifier, respectively. The input of this power amplifier is fed through the output of a Digital to Analog converter (DAC) channel from dSPACE where its value can be controlled and changed throughout machining. The tool displacement signal (represented by the voltage of the optical sensor that can monitor the displacement of the tool shaft) is connected through the Data Interface Box and wired through to the dSPACE and XPS motion controllers. The force signal, calculated based on the measured machining current signal passing through the voice coil actuator (detailed in chapter 3), is fed to the XPS motion controller and used as a feedback signal during machining. The main code for system initialization and tool motion and control is executed in the XPS software interface and written in TCL scripting language. The machining is done while the head is in the force sensor mode to sense any forces exerted on the tool while machining. This mode is executed by activating the PID controller that is implemented using Simulink model and visually monitored using ControlDesk software.

4.2 Experimental procedure

The hole-drilling experiments were performed as follows:

- While the machining head is in the profilometer mode (PID controller off), it is moved down at a speed of 5 mm/sec until it reaches an initial position around 2 mm above the substrate surface level. Then the speed is lowered (50 μm/sec) until it reaches a starting position around 0.5 mm above surface level(zstarting).

- The optical sensor voltage signal is used to detect the workpiece surface level. At a low speed of 10 μm/sec, the tool is moved down until a voltage change of 5 mV is detected (indicating the tool contact with the workpiece).

- After the glass surface level is detected, the tool is moved upwards by a 100 μm.

This gap is added to give some time for the tool to heat up, when switching on the voltage, before it reaches the glass surface.

- the machining voltage is then turned on, and the tool moves at a specified feed rate until the optical sensor voltage returns to its initial voltage at surface level (meaning that the required depth is reached).

4.3 Design of Experiments

The primary objective is to develop a machine learning model capable of receiving machining conditions as input parameters and subsequently predicting the resulting surface texture. To achieve this goal, a Factorial Optimal Design Model was adopted incorporating five key factors, each with specific levels of variation:

- Voltage high-amplitude (3 Levels): This factor explores the impact of three level variations of the voltage high-amplitude level (low, medium, high)
- Voltage low-amplitude (3 Levels): This factor explores the impact of three level variations of low-amplitude voltage level (low, medium, high)
- Duty Cycle (2 Levels): Duty cycle variation is examined as a two-level factor (low, high) to assess its influence on the process.
- Period (2 Levels): The period parameter, also with two levels, is considered to understand its role in shaping the surface texture.
- Electrolyte Viscosity (3 Levels): Varying the viscosity of the electrolyte is explored across three distinct levels to determine its impact on the texture.

The desired output of this experimental setup is the prediction of the bottom surface texture, a critical aspect in machining quality evaluation. This multifactorial design approach ensures a comprehensive exploration of the machining conditions and their correlation with surface texture, facilitating a more nuanced understanding of the

manufacturing process. A total of 42 different combinations were obtained, as shown in Table.

4.4 Data Visualization and Analysis

The data is made up of 42 samples with 5 feature inputs (High voltage, low voltage, period, duty cycle, and electrolyte viscosity) and one output (bottom surface texture) with three labels: smooth, rough, and feathery. Samples of the three textures are shown in figure 4.1.

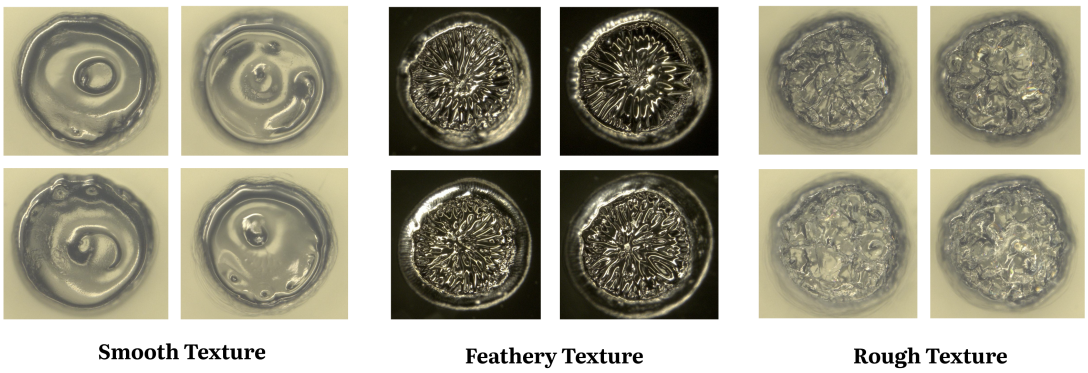

Figure 4.1: The three output labels corresponding to three surface texture from left to tight: smooth, feathery, and rough.

To gain insights into the interrelationships between the features and their correlation with the output surface texture, a data visualization tool, namely a heatmap, was employed as shown in figure 4.2. This heat map provides a comprehensive overview of how the various features are interconnected and their collective correlation with the output variable, surface texture. Notably, the feature that exhibits the strongest correlation with the output is electrolyte viscosity, boasting the highest correlation coefficient at 0.76. This finding underscores the pivotal role of electrolyte viscosity in influencing surface texture. This finding is also in harmony with literature, where Abou Ziki et al. [7] showed that different micro-textures can be formed on SACE machined surfaces during machining with different electrolyte viscosity. A similar

tool of 500 μm diameter was used, applied pulse voltage was 28V, and the reported duty cycle was 80%. As the concentration of electrolyte increases from 10 to 40 wt%, surface roughness decreases by 78%. Micro-cracks were observed at high electrolyte concentration (>30 wt %) whereas at lower values (10 wt%), patterns formed on the surface resembled the Kelvin wake patterns. The texture was found to be highly affected by the flow patterns of electrolyte, where machined surface texture changes from a feathery-like-pattern to a uniform and smooth pattern, as shown in Figure **??**.

Following closely in terms of correlation strength is the voltage high-level feature, with a correlation coefficient of 0.25. Subsequently, the voltage low-level and duty cycle features exhibit lower coefficients, at 0.11 and 0.09, respectively, suggesting their moderate impact on surface texture.

Conversely, the period feature demonstrates a negligible effect on the output surface texture, as indicated by its correlation coefficient of -0.03.

4.5 Machine Learning Classifiers

In the pursuit of applying a machine learning model for predicting the surface texture of machined holes based on a specific set of parameters, an exploration of various machine learning algorithms was undertaken, primarily focusing on support vector machine, logistic regression, and random forest. The code is found in Appendix C. Machine learning, by nature, lacks a one-size-fits-all solution. Hence, it becomes imperative to investigate and understand the intricacies of different classifiers. The subsequent sections will elucidate the operational principles of each.

4.5.1 Support Vector Machine

The support vector machine (SVM), a versatile supervised learning algorithm, is adept at handling both classification and regression problems. Its fundamental premise lies in identifying the optimal hyperplane that effectively segregates data points into their respective groups. The ideal hyperplane is the one that maximizes the separation

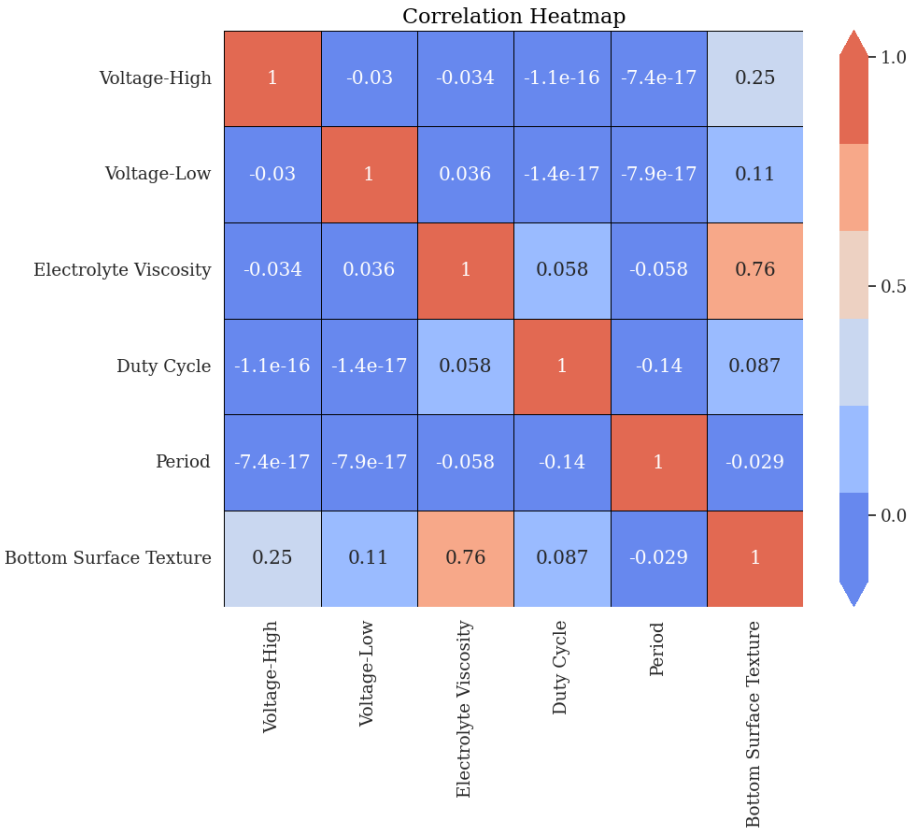

Figure 4.2: A heatmap showing the correlation between features and the output surface texture.

distance between these groups or, in other words, classes.

4.5.2 Logistic Regression

Logistic regression (LR) represents a supervised machine learning algorithm primarily tailored for classification tasks. It operates by modeling the probability that a given input belongs to a specific category or class. LR is predominantly employed in binary classification scenarios, where it deploys a logistic function, often referred to as a sigmoid function, to generate the probability of a binary outcome.

Furthermore, logistic regression is adaptable and can be extended to address multi-class classification challenges. When applied in this context, it is commonly known as multinomial logistic regression or softmax regression. In this expanded role, LR handles situations involving more than two classes, offering a versatile and valuable tool for a broad spectrum of classification problems.

4.5.3 Random Forest

Random forest (RF) is an ensemble algorithm and is one of the most popular machine learning algorithms as it is a versatile algorithm that builds up on the performance of individual decision trees.

4.6 Results and Discussion

The initial step in the present analysis involved standardizing the feature dataset, ensuring that all features share the same scale, with a mean of zero and a standard deviation of one. Subsequently, the data was partitioned into two subsets, allocating 70% for training and reserving the remaining 30% for testing purposes.

Following this data preparation, an instance of each classifier was created, and the corresponding model was trained on the training dataset. The final phase of evaluation encompassed making predictions on the unseen test data. The model's performance was then assessed by calculating key metrics, including precision, recall,

F1 score, and accuracy, based on these predictions.

Table 4.1 provides an overview of the performance metrics for each model on the test data. Notably, among all three classifiers, the random forest model achieved the highest accuracy, reaching 100%. This outcome aligns with the prevailing literature, which often cites random forest as a top-performing algorithm.

However, it's important to acknowledge that achieving a 100% accuracy rate is typically a rare occurrence. In most practical applications, a perfect accuracy score raises concerns about potential issues, including overfitting the model to the training data or having an insufficiently small dataset. In the present case, the dataset used was relatively small, and it's worth noting that working with a more extensive dataset would likely provide a more accurate representation of the model's real-world performance.

Table 4.1: The Results of different machine learning classifiers on predicting the surface texture of machined holes

	Precision	**Recall**	**F1-score**	**Accuracy**
Support Vector Machine	81	77	74	77
Logistic Regression	89	85	84	85
Random Forest	100	100	100	100

Chapter 5

Conclusion

This thesis has contributed in constructing major parts of a SACE machine, including mechanical and electrical components as well as the control system. This enabled the online monitoring of SACE process and applying machine learning algorithms for multiple purposes. The outcomes of this thesis can be summarized as follows:

5.1 Thesis Contributions

The main contributions of this thesis are summarized as follows:

Design of Major hardware components in SACE:

- The Processing Cell: An acrylic processing cell was designed and assembled to meet specific requirements. Its design is optimized to maintain uniform electrolyte levels, a crucial factor for machining quality and consistency. The cell consists of three rectangular layers, facilitating an electrolyte circulation system powered by a peristaltic pump that connects the middle layer to the inner layer. The final layer is securely fixed to the stage fixture, serving as an added safety layer.

- The Workpiece Holder: A modular holder, 3D printed from ABS plastic, was designed to be easily attached to the cell. This holder guarantees the workpiece's stability with no movement along the x, y, and z axes.

- Printed Circuit Boards (PCBs): Four PCBs were custom-designed, and connector types were soldered onto them to facilitate the physical interconnection of various system components.

- Data Interface Unit: A well-ventilated data interface box has been developed and built to accommodate the PCBs, motor controllers, and their respective connections.

- Current Probe Adapter: An adapter device that adapts the connector type of the Tektronix current probe available at our lab to the BNC channel input of the dSPACE board was designed. The adapter constitutes two PCBs housed in an acrylic box and enables the reading of the current signal during SACE.

Force-Feedback Control: Design and Implementation:

- Dynamic System Modeling: The system was modeled as a second order mass-spring system. The model's response to a step input showed an underdamped system which oscillates for more than 2.5 s before settling to its steady state.A PID controller was then implemented and tuned on the system, and initial values for the control parameter were obtained.

- Control System Implementation: The PID controller was implemented on the physical structure. A simulink code was developed to apply the PID on the physical structure. The implemented PID controller features a rise time of 200 ms and 0 overshoot. The resulting force sensor has a working range of -5N to 5N, a response time of 200 ms to disturbance, and 11.8 mV rms noise.

- Force-feedback drilling experiments: Experiments were conducted using force-feedback drilling technique. A total of 12 holes were drilled. For small depths (100 μm), zero counteractions are recorded. However, as drilling depth increases to 300 μm, the number of counteractions increases (12 per hole). At 500 μm, the counteractions significantly rose to 62. These findings align with

established SACE literature, which notes that as drilling depth increases, the Material Removal Rate (MRR) decreases, making the process more challenging due to complications in electrolyte flushing within the holes. Consequently, contact forces intensify with greater depth, leading to a higher number of counteractions by the system. Furthermore, the decreasing trend in the number of counteractions (hence reduced drilling time) with each subsequent hole can be attributed to the more stabilized heating (substrate and electrolyte temperature). This causes improved repeatability of the drilling results as more holes are drilled.

Machine Learning for Surface Texture Characterization Application

- A machine learning application was tested to predict the surface texture of machined holes based on input machining features. The input features were the high and low values of the machining voltage, the duty cycle, the period, and the electrolyte viscosity.

- Three machine learning models were implemented using the Sickit learn library, mainly support vector machines, logistic regression, and Random Forest. The code was written using Python on Google Colab.

- The support vector machine scored the lowest accuracy of 77%, followed by logistic regression which scored 85 %. Random forest scored the highest accuracy (100%). These provide preliminary results, as achieving a 100% accuracy is rare and often raises concerns, including overfitting or having a very small dataset. A larger dataset would offer a more accurate model representation which will be conducted in future work.

The objectives of this thesis, spanning component design and development and the integration of force feedback control and machine learning, have been successfully accomplished. Through these achievements, this thesis contributed to the advancement

and refinement of SACE technology, setting the stage for online monitoring and thus moving the process to a smarter, more efficient, and highly responsive one.

5.2 Outlook

In this section, potential areas for future work are highlighted, providing a glimpse into possible research directions

Adding Tool Rotations

Incorporating tool rotations has shown positive results in reducing Heat-Affected Zone (HAZ) phenomena and hole overcut by facilitating better electrolyte access to the machining zone. Nevertheless, it is essential to recognize that introducing tool rotations will impact the PID characteristics due to potential vibrations induced by the rotating motor. Therefore, further work in this area is needed.

Online monitoring of the machining forces

The force signal's potential to assess machining quality is another crucial aspect for investigation. For instance, when a shallow hole experiences an excessive number of counteractions, it indicates a slow Material Removal Rate (MRR), signifying the requirement for an immediate voltage increment. Counter actions can be initiated based on the force sensor's input data.

Real Time Actions to modify faulty machining

The system is designed with the capability to utilize its I/O channels for both reading and writing signals, enabling the potential for real-time monitoring of the process and initiating corrective machining actions based on the acquired data. Thus, more work can be investigated within this domain. For instance, the system can be further explored to develop motion algorithms that are activated based on the specific type of data being read.

Deep learning Models for Controlling machining quality

In this thesis, preliminary results were obtained by exploring machine learning algorithms for characterizing the texture of machined holes. The dataset used was relatively small, and the input parameters were not exhaustive. The potential of AI can be harnessed on a larger scale than the current study, to collect more extensive machining data and employ deep learning models for a more comprehensive understanding of the relationships between parameters and their impact on machining quality.

Controlling the Surface Texture

Among the upcoming steps are motion algorithms designed to create distinct and defined textures. Following this, efforts will focus on developing algorithms to consistently maintain a controlled gap between the tool and the surface.

Bibliography

[1] I Etsion and E Sher, "Improving fuel efficiency with laser surface textured piston rings," *Tribology International*, vol. 42, no. 4, pp. 542–547, 2009.

[2] J. W. Byun, H. S. Shin, M. H. Kwon, B. H. Kim, and C. N. Chu, "Surface texturing by micro ecm for friction reduction," *International Journal of Precision Engineering and Manufacturing*, vol. 11, pp. 747–753, 2010.

[3] Z. Bassyouni and J. D. Abou Ziki, "The capabilities of spark-assisted chemical engraving: A review," *Journal of Manufacturing and Materials Processing*, vol. 4, no. 4, p. 99, 2020.

[4] M Jalali, P Maillard, and R Wüthrich, "Toward a better understanding of glass gravity-feed micro-hole drilling with electrochemical discharges," *Journal of Micromechanics and Microengineering*, vol. 19, no. 4, p. 045 001, 2009.

[5] D.-J. Kim, Y. Ahn, S.-H. Lee, and Y.-K. Kim, "Voltage pulse frequency and duty ratio effects in an electrochemical discharge microdrilling process of pyrex glass," *International Journal of Machine Tools and Manufacture*, vol. 46, no. 10, pp. 1064–1067, 2006.

[6] A. Ziki and J. Daher, "Spark assisted chemical engraving: A novel approach for quantifying the machining zone parameters using drilling forces," Ph.D. dissertation, Concordia University, 2014.

[7] J. D. Abou Ziki, T. F. Didar, and R. Wüthrich, "Micro-texturing channel surfaces on glass with spark assisted chemical engraving," *International Journal of Machine Tools and Manufacture*, vol. 57, pp. 66–72, 2012.

[8] I. Ikwuagwu, A. Kiani, and J. D. Abou Ziki, "Hybrid method combining sace micro-machining and laser processing to fabricate glass micro-features with special surface properties," *IFAC-PapersOnLine*, vol. 52, no. 10, pp. 311–314, 2019.

[9] J. D. Abou Ziki, "Investigating the surface layer of micro-features machined by spark assisted chemical engraving," *IFAC-PapersOnLine*, vol. 52, no. 10, pp. 315–318, 2019.

[10] L. A. Hof and R. Wüthrich, "Rapid prototyping of packaged glass devices: Eliminating a process step in the manufacturing workflow from micromachining to die singularizing," *Manufacturing Letters*, vol. 17, pp. 9–13, 2018.

[11] Y. Temiz, R. D. Lovchik, G. V. Kaigala, and E. Delamarche, "Lab-on-a-chip devices: How to close and plug the lab?" *Microelectronic Engineering*, vol. 132, pp. 156–175, 2015.

[12] Y. Xu *et al.*, "Bonding of glass nanofluidic chips at room temperature by a one-step surface activation using an o 2/cf 4 plasma treatment," *Lab on a Chip*, vol. 13, no. 6, pp. 1048–1052, 2013.

[13] N. Chiem, L. Lockyear-Shultz, P. Andersson, C. Skinner, and D. J. Harrison, "Room temperature bonding of micromachined glass devices for capillary electrophoresis," *Sensors and Actuators B: Chemical*, vol. 63, no. 3, pp. 147–152, 2000.

[14] C.-K. Chung *et al.*, "Water-assisted co 2 laser ablated glass and modified thermal bonding for capillary-driven bio-fluidic application," *Biomedical microdevices*, vol. 12, pp. 107–114, 2010.

[15] A. Ben-Yakar, A. Harkin, J. Ashmore, R. L. Byer, and H. A. Stone, "Thermal and fluid processes of a thin melt zone during femtosecond laser ablation of glass: The formation of rims by single laser pulses," *Journal of Physics D: Applied Physics*, vol. 40, no. 5, p. 1447, 2007.

[16] C.-K. Chung and S. Lin, "On the fabrication of minimizing bulges and reducing the feature dimensions of microchannels using novel co2 laser micromachining," *Journal of Micromechanics and Microengineering*, vol. 21, no. 6, p. 065 023, 2011.

[17] H. Wensink, H. V. Jansen, J. W. Berenschot, and M. C. Elwenspoek, "Mask materials for powder blasting," *Journal of micromechanics and microengineering*, vol. 10, no. 2, p. 175, 2000.

[18] H. Wensink, "Fabrication of microstructures by powder blasting," *University of Twente: Enshede, The Netherlands*, 2002.

[19] L. A. Hof and R. Wüthrich, "Rapid prototyping of packaged glass devices: Eliminating a process step in the manufacturing workflow from micromachining to die singularizing," *Manufacturing Letters*, vol. 17, pp. 9–13, 2018.

[20] R. Wüthrich and V. Fascio, "Machining of non-conducting materials using electrochemical discharge phenomenon—an overview," *International Journal of Machine Tools and Manufacture*, vol. 45, no. 9, pp. 1095–1108, 2005.

[21] R. Wuthrich and J. D. Abou Ziki, *Micromachining using electrochemical discharge phenomenon: fundamentals and application of spark assisted chemical engraving*. William Andrew, 2014.

[22] J. D. Abou Ziki and R. Wüthrich, "Forces exerted on the tool-electrode during constant-feed glass micro-drilling by spark assisted chemical engraving," *International Journal of Machine Tools and Manufacture*, vol. 73, pp. 47–54, 2013.

[23] R. Wüthrich, U. Spaelter, Y Wu, and H. Bleuler, "A systematic characterization method for gravity-feed micro-hole drilling in glass with spark assisted chemical engraving (sace)," *Journal of Micromechanics and Microengineering*, vol. 16, no. 9, p. 1891, 2006.

[24] P Maillard, B Despont, H Bleuler, and R Wüthrich, "Geometrical characterization of micro-holes drilled in glass by gravity-feed with spark assisted chemical engraving (sace)," *Journal of micromechanics and microengineering*, vol. 17, no. 7, p. 1343, 2007.

[25] R Wüthrich, B Despont, P Maillard, and H Bleuler, "Improving the material removal rate in spark-assisted chemical engraving (sace) gravity-feed micro-hole drilling by tool vibration," *Journal of Micromechanics and Microengineering*, vol. 16, no. 11, N28, 2006.

[26] M.-S. Han, B.-K. Min, and S. J. Lee, "Geometric improvement of electrochemical discharge micro-drilling using an ultrasonic-vibrated electrolyte," *Journal of Micromechanics and Microengineering*, vol. 19, no. 6, p. 065 004, 2009.

[27] M.-S. Han, B.-K. Min, and S. J. Lee, "Geometric improvement of electrochemical discharge micro-drilling using an ultrasonic-vibrated electrolyte," *Journal of Micromechanics and Microengineering*, vol. 19, no. 6, p. 065 004, 2009.

[28] K. Furutani and H. Maeda, "Machining a glass rod with a lathe-type electrochemical discharge machine," *Journal of Micromechanics and Microengineering*, vol. 18, no. 6, p. 065 006, 2008.

[29] F Mehrabi, M Farahnakian, S Elhami, and M. Razfar, "Application of electrolyte injection to the electro-chemical discharge machining (ecdm) on the optical glass," *Journal of Materials Processing Technology*, vol. 255, pp. 665–672, 2018.

[30] J. D. Abou Ziki and R. Wüthrich, "The machining gap during constant velocity-feed glass micro-drilling by spark assisted chemical engraving," *Journal of Manufacturing Processes*, vol. 19, pp. 87–94, 2015.

[31] J. D. Abou Ziki and R. Wüthrich, "Nature of drilling forces during spark assisted chemical engraving," *Manufacturing Letters*, vol. 4, pp. 10–13, 2015.

[32] J. D. Abou Ziki, L. A. Hof, and R. Wüthrich, "The machining temperature during spark assisted chemical engraving of glass," *Manufacturing Letters*, vol. 3, pp. 9–13, 2015.

[33] R. Wuthrich and J. D. Abou Ziki, *Micromachining using electrochemical discharge phenomenon: fundamentals and application of spark assisted chemical engraving*. William Andrew, 2014.

[34] H. H. Kellogg, "Anode effect in aqueous electrolysis," *Journal of the electrochemical society*, vol. 97, no. 4, p. 133, 1950.

[35] I. Basak and A. Ghosh, "Mechanism of spark generation during electrochemical discharge machining: A theoretical model and experimental verification," *Journal of Materials Processing Technology*, vol. 62, no. 1-3, pp. 46–53, 1996.

[36] V Fascio, H. Langen, H Bleuler, and C. Comninellis, "Investigations of the spark assisted chemical engraving," *Electrochemistry communications*, vol. 5, no. 3, pp. 203–207, 2003.

[37] H Kurafuji, "Electrical discharge drilling of glass," *Ann. CIRP*, vol. 16, pp. 415–419, 1968.

[38] A. Allagui and R. Wüthrich, "Gas film formation time and gas film life time during electrochemical discharge phenomenon," *Electrochimica Acta*, vol. 54, no. 23, pp. 5336–5343, 2009.

[39] P. Kumar Gupta, A. Dvivedi, and P. Kumar, "Effect of electrolytes on quality characteristics of glass during ecdm," in *Key Engineering Materials*, Trans Tech Publ, vol. 658, 2015, pp. 141–145.

[40] N. Sabahi, M. Hajian, and M. R. Razfar, "Experimental study on the heat-affected zone of glass substrate machined by electrochemical discharge machining (ecdm) process," *The International Journal of Advanced Manufacturing Technology*, vol. 97, pp. 1557–1564, 2018.

[41] M. Harugade, M. Kavade, and N. Hargude, "Effect of electrolyte solution on material removal rate in electrochemical discharge machining," *IOSR Journal of Mechanical and Civil Engineering (IOSR-JMCE)*, vol. 5, pp. 1–8, 2013.

[42] S. K. Jui, A. B. Kamaraj, and M. M. Sundaram, "High aspect ratio micromachining of glass by electrochemical discharge machining (ecdm)," *Journal of Manufacturing Processes*, vol. 15, no. 4, pp. 460–466, 2013.

[43] A. B. Kamaraj, S. K. Jui, Z. Cai, and M. M. Sundaram, "A mathematical model to predict overcut during electrochemical discharge machining," *The International Journal of Advanced Manufacturing Technology*, vol. 81, pp. 685–691, 2015.

[44] K. R. Kolhekar and M. Sundaram, "A study on the effect of electrolyte concentration on surface integrity in micro electrochemical discharge machining," *Procedia CIRP*, vol. 45, pp. 355–358, 2016.

[45] Z. Zhang *et al.*, "A study to explore the properties of electrochemical discharge effect based on pulse power supply," *The International Journal of Advanced Manufacturing Technology*, vol. 85, pp. 2107–2114, 2016.

[46] Z. Zhang *et al.*, "A study to explore the properties of electrochemical discharge effect based on pulse power supply," *The International Journal of Advanced Manufacturing Technology*, vol. 85, pp. 2107–2114, 2016.

[47] S. Bellubbi, R. Naik, and N Sathisha, "An experimental study of process parameters on material removal rate in ecdm process," *Materials Today: Proceedings*, vol. 35, pp. 298–302, 2021.

[48] Y. Laio, L. Wu, and W. Peng, "A study to improve drilling quality of electrochemical discharge machining (ecdm) process," *Procedia CIRP*, vol. 6, pp. 609–614, 2013.

[49] R. Wüthrich *et al.*, "Physical principles and miniaturization of spark assisted chemical engraving (sace)," *Journal of Micromechanics and Microengineering*, vol. 15, no. 10, S268, 2005.

[50] M.-S. Han, B.-K. Min, and S. J. Lee, "Improvement of surface integrity of electro-chemical discharge machining process using powder-mixed electrolyte," *Journal of Materials Processing Technology*, vol. 191, no. 1-3, pp. 224–227, 2007.

[51] L. Paul and A. B. Kumar, "Improvement in micro feature generation in ecdm process with powder mixed electrolyte," in *International Manufacturing Science and Engineering Conference*, American Society of Mechanical Engineers, vol. 51388, 2018, V004T03A049.

[52] C. Yang, S. Song, B. Yan, and F. Huang, "Improving machining performance of wire electrochemical discharge machining by adding sic abrasive to electrolyte," *International Journal of machine tools and manufacture*, vol. 46, no. 15, pp. 2044–2050, 2006.

[53] K. Y. Kuo, K. L. Wu, C. K. Yang, and B.-H. Yan, "Effect of adding sic powder on surface quality of quartz glass microslit machined by wecdm," *The International Journal of Advanced Manufacturing Technology*, vol. 78, pp. 73–83, 2015.

[54] M. Hajian, M. R. Razfar, and S. Movahed, "An experimental study on the effect of magnetic field orientations and electrolyte concentrations on ecdm milling performance of glass," *Precision Engineering*, vol. 45, pp. 322–331, 2016.

[55] H. Tokura, I. Kondoh, and M. Yoshikswa, "Ceramic material processing by electrical discharge in electrolyte," *Journal of materials science*, vol. 24, pp. 991–998, 1989.

[56] V. Jain, P Sreenivasa Rao, S. Choudhary, and K. Rajurkar, "Experimental investigations into traveling wire electrochemical spark machining (tw-ecsm) of composites," 1991.

[57] C. Jawalkar, "Investigation on performance enhancement of ecdm process while machining glass," *Indian Institute of Technology: Roorkee, India*, 2013.

[58] K. Furutani and H. Maeda, "Machining a glass rod with a lathe-type electrochemical discharge machine," *Journal of Micromechanics and Microengineering*, vol. 18, no. 6, p. 065 006, 2008.

[59] Z.-P. Zheng, H.-C. Su, F.-Y. Huang, and B.-H. Yan, "The tool geometrical shape and pulse-off time of pulse voltage effects in a pyrex glass electrochemical discharge microdrilling process," *Journal of Micromechanics and Microengineering*, vol. 17, no. 2, p. 265, 2007.

[60] Z.-P. Zheng, J.-K. Lin, F.-Y. Huang, and B.-H. Yan, "Improving the machining efficiency in electrochemical discharge machining (ecdm) microhole drilling by offset pulse voltage," *Journal of Micromechanics and Microengineering*, vol. 18, no. 2, p. 025 014, 2008.

[61] L. Paul and L. V. Korah, "Effect of power source in ecdm process with fem modeling," *Procedia Technology*, vol. 25, pp. 1175–1181, 2016.

[62] F. Charbonneau, "Improving the sparks assisted chemical engraving (sace) for industrial application," Ph.D. dissertation, Concordia University, 2016.

[63] W. Tang *et al.*, "Force feedback feed for electrochemical discharge machining (ecdm) micro-hole drilling," in *15th International Conference & Exhibition of the European Society of Precision Engineering and Nanotechnology*, vol. 1, 2015, pp. 73–74.

[64] T. Singh and A. Dvivedi, "On pressurized feeding approach for effective control on working gap in ecdm," *Materials and Manufacturing Processes*, vol. 33, no. 4, pp. 462–473, 2018.

[65] S. M. Seyedi Sahebari, Z. Bassyouni, A. Barari, and J. D. Abou Ziki, "Intelligent characterization of spark-assisted chemical engraving (sace) process using time series classification," *The International Journal of Advanced Manufacturing Technology*, pp. 1–16, 2023.

Appendix A: Motor Datasheets

LA10-12-027A | F

WINDING CONSTANTS *	UNITS	TOL	SYMBOL	WDG Z
DC RESISTANCE	OHMS	±12.5%	R	11.0
VOLTAGE @ F_P	VOLTS	NOMINAL	V_P	25.1
CURRENT @ F_P	AMPERES	NOMINAL	I_P	2.28
FORCE SENSITIVITY	OZ/AMP	±10%	K_F	21.1
	N/AMP	±10%		5.87
BACK EMF CONSTANT	V/FT/SEC	±10%	K_B	1.79
	V/M/SEC	±10%		5.87
INDUCTANCE ****	MILLI-HENRY	±15%	L	3.05

ACTUATOR PARAMETERS *	UNITS	SYMBOL	VALUE
PEAK FORCE **	OZ	F_P	48
	N		13.3
CONTINUOUS STALL FORCE ***	OZ	F_{CS}	17.8
	N		4.95
ACTUATOR CONSTANT	OZ/ $\sqrt{WATT}$	K_A	6.36
	N/ $\sqrt{WATT}$		1.77
ELECTRICAL TIME CONSTANT	MICRO-SEC	τ_E	277
MECHANICAL TIME CONSTANT	MILLI-SEC	τ_M	4.43
POWER I^2R @ F_P	WATTS	P_P	57.2
STROKE	± INCHES		0.180
	± MM		4.57
CLEARANCE ON EACH SIDE OF COIL	IN		0.015
	MM		0.38
THERMAL RESISTANCE OF COIL	°C/WATT	Θ_{TH}	11.3
MAX. ALLOWABLE COIL TEMP.	°C	TEMP	155
WEIGHT OF COIL ASSEMBLY	OZ	WT_C	0.49
	G		13.89
WEIGHT OF FIELD ASSEMBLY	OZ	WT_F	2.0
	G		56.7

* 25°C AMBIENT TEMPERATURE
** 10 SECONDS AT 25°C AMBIENT & 155°C COIL TEMP
*** 25°C AMBIENT & 155°C WINDING TEMPERATURE
**** MEASURED AT 1000 Hz

LTR	ECO NO.	DESCRIPTION	DRN	APP'D	DATE
E	080225	ADD CHART, UPDATE DATA, RoHS	JWT	MG	04/18/06
F	080406	UPDATED THD HOLES CALL-OUT	RG	MG	10/03/08

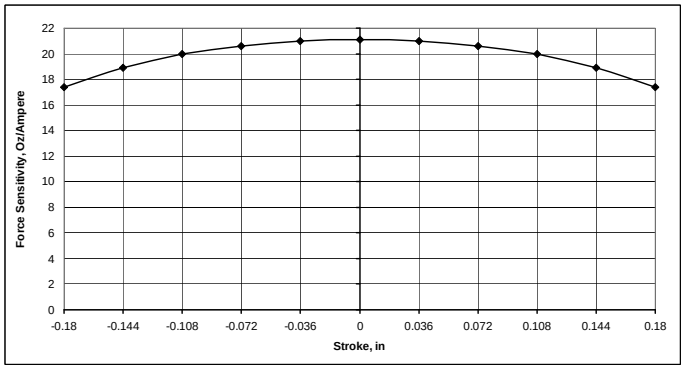

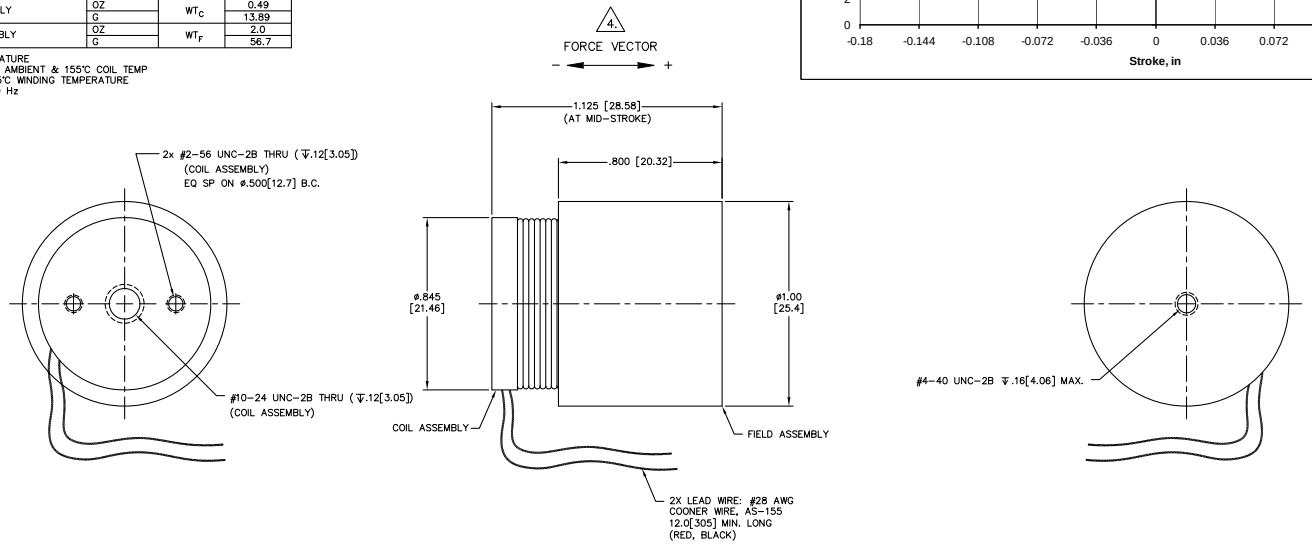

5. INSULATION RESISTANCE IS 100 MEGOHMS AT 500 VDC.

4. A POSITIVE (+) VOLTAGE APPLIED TO THE RED LEAD WILL PRODUCE A FORCE ON THE COIL ASSEMBLY IN THE POSITIVE (+) DIRECTION.

3. ALL ABBREVIATIONS IAW ASME Y14.38.

2. INTERPRET DRAWING IAW ASME Y14.100.

1. INTERPRET DIMENSIONING AND TOLERANCING IAW ASME Y14.5M-1994.

NOTES: UNLESS OTHERWISE SPECIFIED

RoHS

THIRD ANGLE PROJECTION

UNLESS OTHERWISE SPECIFIED:
-ALL DIMENSIONS ARE IN INCHES
-BREAK SHARP EDGES .015 MAX.
-SURFACE ROUGHNESS √63
-DIMENSIONS APPLY AFTER FINISH
-MAX FILLET R .010
-DIAMETERS SHALL NOT EXCEED A RUNOUT OF .005 FIM

TOLERANCES:
DECIMALS: .X ± .03; .XX ± .01; .XXX ± .005
ANGULAR: ±0° 30'

DO NOT SCALE DRAWING

BEI *KIMCO MAGNETICS DIVISION*
VISTA, CA 92081

DRAWN	BUTTERFIELD	05/23/97
MECH CHECK	STHAL	02/24/05
APPD	MARCOS	05/23/97
FILE NO.	L\TOP LEV\LA\	

TITLE: LINEAR ACTUATOR

SIZE	FSCM NO.	DWG NO.	REV
D	55789	LA10-12-027A	F

SCALE: NONE SHEET 1 OF 1

LA10-12-027A | F

Appendix B: PCB Schematics

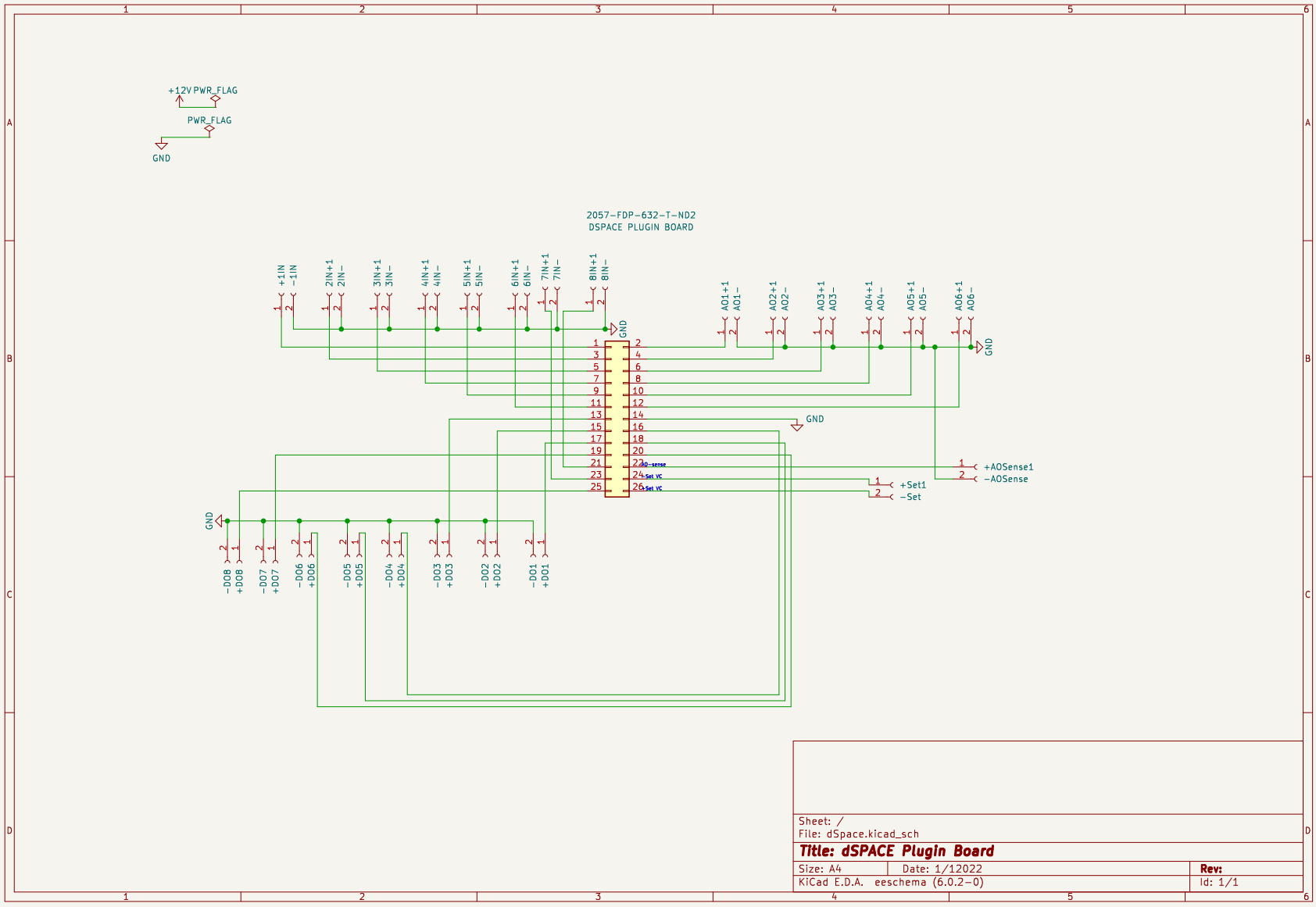
+12V PWR_FLAG
PWR_FLAG
GND
2057-FDP-632-T-ND2
DSPACE PLUGIN BOARD
+1IN
-1IN
2IN+1
2IN-
3IN+1
3IN-
4IN+1
4IN-
5IN+1
5IN-
6IN+1
6IN-
7IN+1
7IN-
8IN+1
8IN-
AO1+1
AO1-
AO2+1
AO2-
AO3+1
AO3-
AO4+1
AO4-
AO5+1
AO5-
AO6+1
AO6-
GND
GND
AO-sense
Set VC
Set VC
+AOSense1
-AOSense
+Set1
-Set
GND
-DO8
+DO8
-DO7
+DO7
-DO6
+DO6
-DO5
+DO5
-DO4
+DO4
-DO3
+DO3
-DO2
+DO2
-DO1
+DO1
Sheet: /
File: dSpace.kicad_sch
Title: dSPACE Plugin Board
Size: A4
Date: 1/12022
Rev:
KiCad E.D.A. eeschema (6.0.2-0)
Id: 1/1

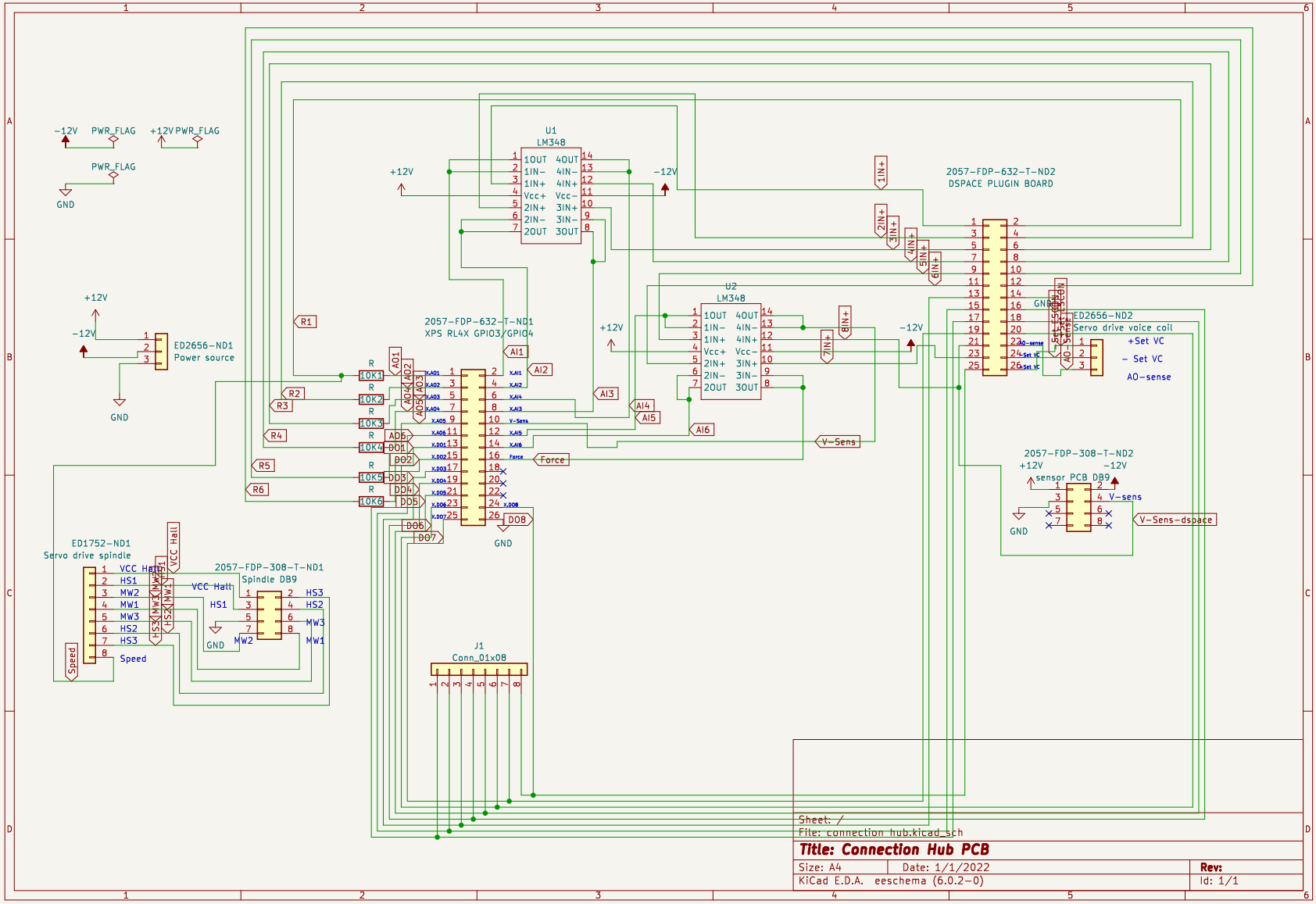
U1
LM348
U2
LM348
2057-FDP-632-T-ND2
DSPACE PLUGIN BOARD
2057-FDP-632-T-ND1
XPS RL4X GPIO3/GPIO4
ED2656-ND1
Power source
ED2656-ND2
Servo drive voice coil
+Set VC
- Set VC
AO-sense
2057-FDP-308-T-ND2
sensor PCB DB9
V-Sens-dspace
ED1752-ND1
Servo drive spindle
2057-FDP-308-T-ND1
Spindle DB9
J1
Conn_01x08
V-Sens
Force
Speed
VCC Hall
Sheet: /
File: connection hub.kicad_sch
Title: Connection Hub PCB
Size: A4
Date: 1/1/2022
KiCad E.D.A. eeschema (6.0.2-0)
Rev:
Id: 1/1

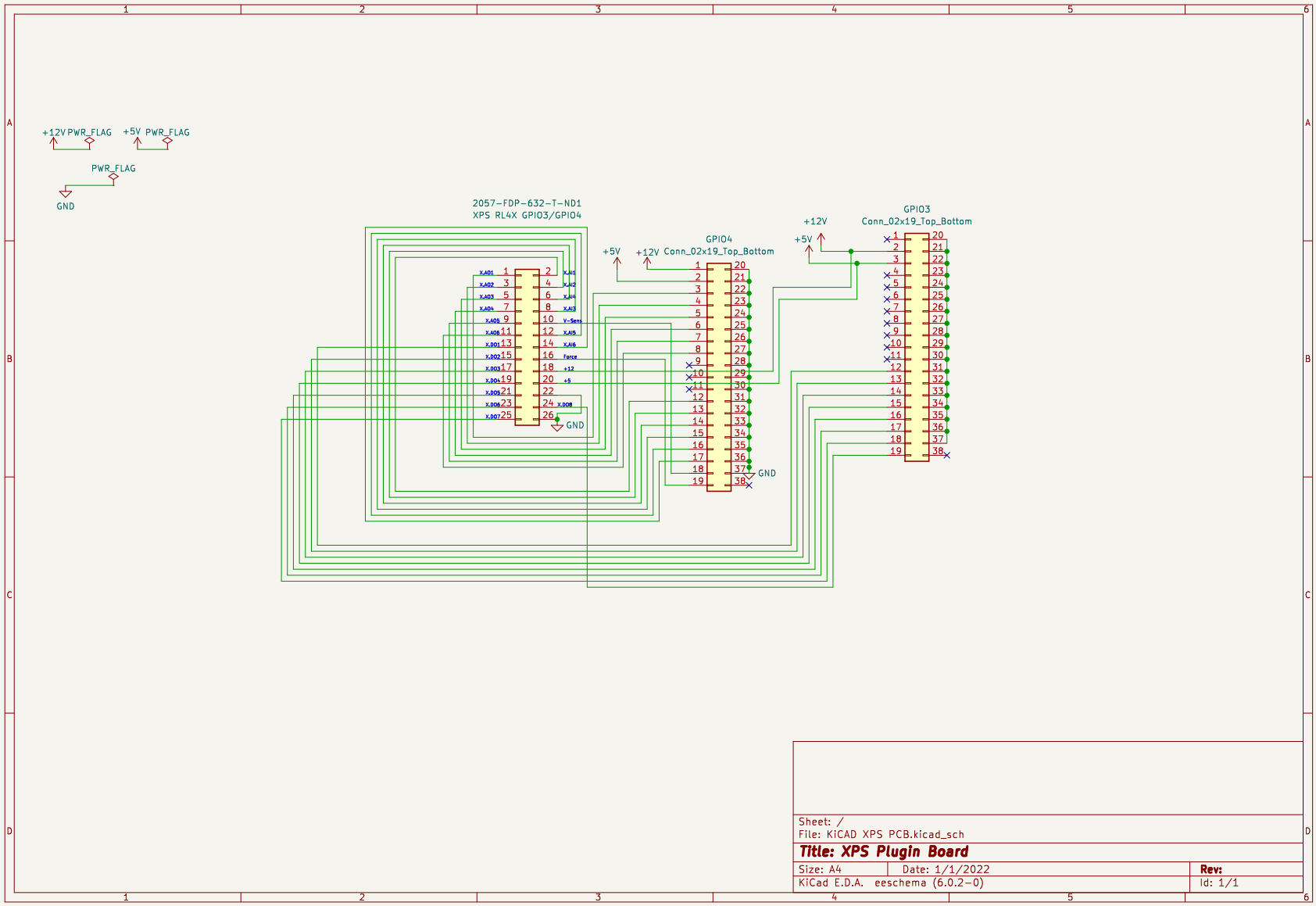
+12V PWR_FLAG
+5V PWR_FLAG
PWR_FLAG
GND
2057-FDP-632-T-ND1
XPS RL4X GPIO3/GPIO4
GPIO4
Conn_02x19_Top_Bottom
GPIO3
Conn_02x19_Top_Bottom
+5V
+12V
GND
Sheet: /
File: KiCAD XPS PCB.kicad_sch
Title: XPS Plugin Board
Size: A4
Date: 1/1/2022
Rev:
KiCad E.D.A. eeschema (6.0.2-0)
Id: 1/1

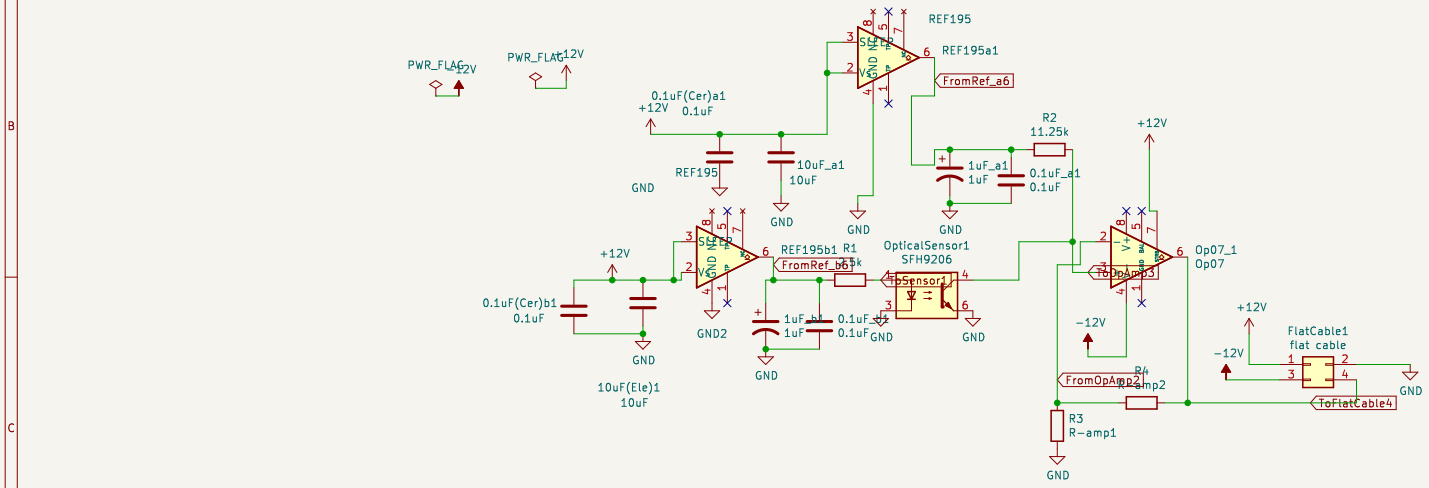

Sheet: /		
File: opticalSensorV9.kicad_sch		
Title: Optical Sensor PCB		
Size: A4	Date: 1/1/2022	**Rev:**
KiCad E.D.A. eeschema (6.0.2−0)		Id: 1/1

Appendix C: Google Colaboratory Notebook (Machine Learning Algorithms)

Predicting the Texture of Blind Micro-hole Surfaces Machined using Spark Assisted Chemical Engraving (SACE) using Machine Learning Algorithms

Objective: The goal of this colab is to predict the texture of the surface of micro-holes machined using SACE.

The dataset was created using a Factorial Optimal Design Model with 5 Factors (Basically the Input Features) as follows:

- Voltage high-amplitude
- Voltage low-amplitude
- Duty Cycle
- Period
- Electrolyte Viscosity

We have one output Feature:

- Bottom Surface Texture

A total of 42 Holes were drilled using SACE :)

Import Libraries

```
import pandas as pd
import numpy as np
from sklearn.model_selection import train_test_split
from sklearn.preprocessing import StandardScaler
from sklearn.ensemble import RandomForestClassifier
from sklearn.linear_model import LogisticRegression
from sklearn.svm import SVC
from sklearn.neighbors import KNeighborsClassifier
from sklearn.metrics import classification_report, accuracy_score
from keras.models import Sequential
from keras.layers import Dense
```

Reading the Dataset from Drive

```
# Mount Google Drive:
from google.colab import drive
drive.mount('/content/drive')
path= '/content/drive/My Drive/Surface Texture Folder/'
```

```
Mounted at /content/drive
```

```
# Load your dataset (replace 'your_dataset.csv' with your actual file)
data = pd.read_csv(path + 'Dataset5.csv')
```

Exploratory Data Analysis

```
data.head()
```

	Voltage-High	Voltage-Low	Electrolyte Viscosity	Duty Cycle	Period	Bottom Surface Texture
0	30	15.0	1.12	90	2.5	feathery
1	30	17.5	1.12	70	6.0	feathery
2	30	17.5	1.12	70	6.0	feathery
3	30	21.0	1.12	70	2.5	feathery
4	30	21.0	1.12	90	6.0	feathery

```
data.describe()
```

	Voltage-High	Voltage-Low	Electrolyte Viscosity	Duty Cycle	Period
count	42.000000	42.000000	42.000000	42.000000	42.000000
mean	34.000000	17.833333	2.632143	80.000000	4.250000
std	3.305575	2.490633	1.292758	10.121217	1.771213
min	30.000000	15.000000	1.120000	70.000000	2.500000
25%	30.000000	15.000000	1.120000	70.000000	2.500000
50%	34.000000	17.500000	2.750000	80.000000	4.250000
75%	38.000000	21.000000	4.250000	90.000000	6.000000
max	38.000000	21.000000	4.250000	90.000000	6.000000

```
output_counts = data['Bottom Surface Texture'].value_counts()
print("\nUnique Classes in the Output Column and Their Counts:")
print(output_counts)
```

```
Unique Classes in the Output Column and Their Counts:
feathery    17
Rough       13
smooth      12
Name: Bottom Surface Texture, dtype: int64
```

```
# Separate features and labels
X = data[['Voltage-High', 'Voltage-Low', 'Electrolyte Viscosity', 'Duty Cycle', 'Period']]
y = data[['Bottom Surface Texture']]
```

```
import matplotlib.pyplot as plt
import seaborn as sns

# Combine features and labels into a single DataFrame for visualization
df = pd.concat([X, y], axis=1)

# Pairplot for visualizing feature relationships
sns.pairplot(df, hue='Bottom Surface Texture', palette='viridis')
plt.suptitle('Pairplot of Features')
plt.show()

# Boxplot for each feature vs. Bottom Surface Texture
plt.figure(figsize=(16, 8))
for i, feature in enumerate(X.columns):
    plt.subplot(2, 3, i + 1)
    sns.boxplot(x='Bottom Surface Texture', y=feature, data=df, palette='Set1')
    plt.title(f'Effect of {feature}')
plt.tight_layout()
plt.show()
```

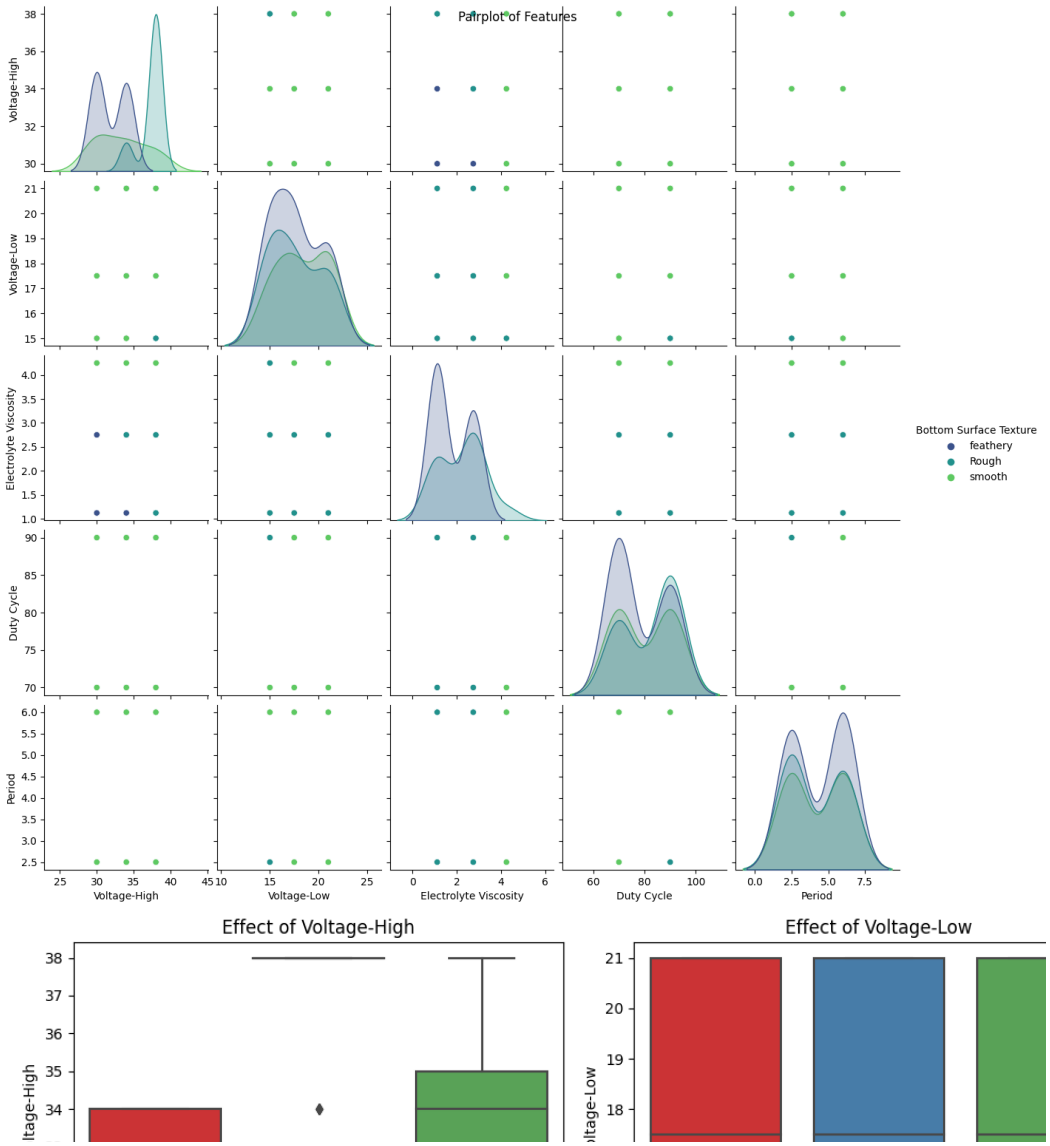
Pairplot of Features
Voltage-High
Voltage-Low
Electrolyte Viscosity
Duty Cycle
Period
Bottom Surface Texture
feathery
Rough
smooth

Effect of Voltage-High
Effect of Voltage-Low

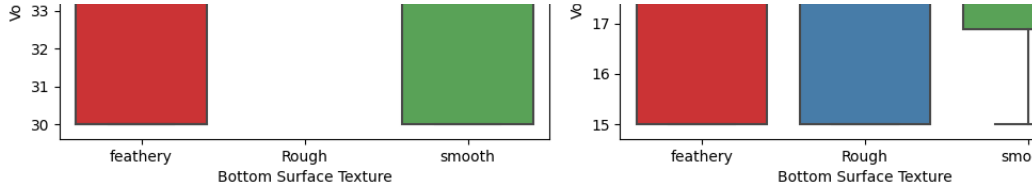


```
import pandas as pd
import matplotlib.pyplot as plt
import seaborn as sns

# Load the dataset from a CSV file
data = pd.read_csv(path + 'Dataset6.csv')



# Calculate the correlation matrix
corr_matrix = data.corr()

# Customize the color palette (replace with your preferred colors)
custom_palette = sns.color_palette("coolwarm")

# Create a heatmap with customized colors, fonts, and borders
plt.figure(figsize=(10, 8))

# Set the font style to 'DejaVu Serif' (or replace with an available font on your system)
plt.rcParams['font.family'] = 'DejaVu Serif'
plt.rcParams['text.color'] = 'black'  # Set font color to black

# Create the heatmap with the customizations
heatmap = sns.heatmap(corr_matrix, annot=True, cmap=custom_palette, linewidths=0.5, linecolor='black', cbar_kws={"orientation": "vertical", "ticks": [-1, -0.5, 0, 0.5, 1], "extend": "b

# Customize the title
plt.title('Correlation Heatmap', fontsize=16)
```

```
# Save or display the heatmap
plt.show()
```

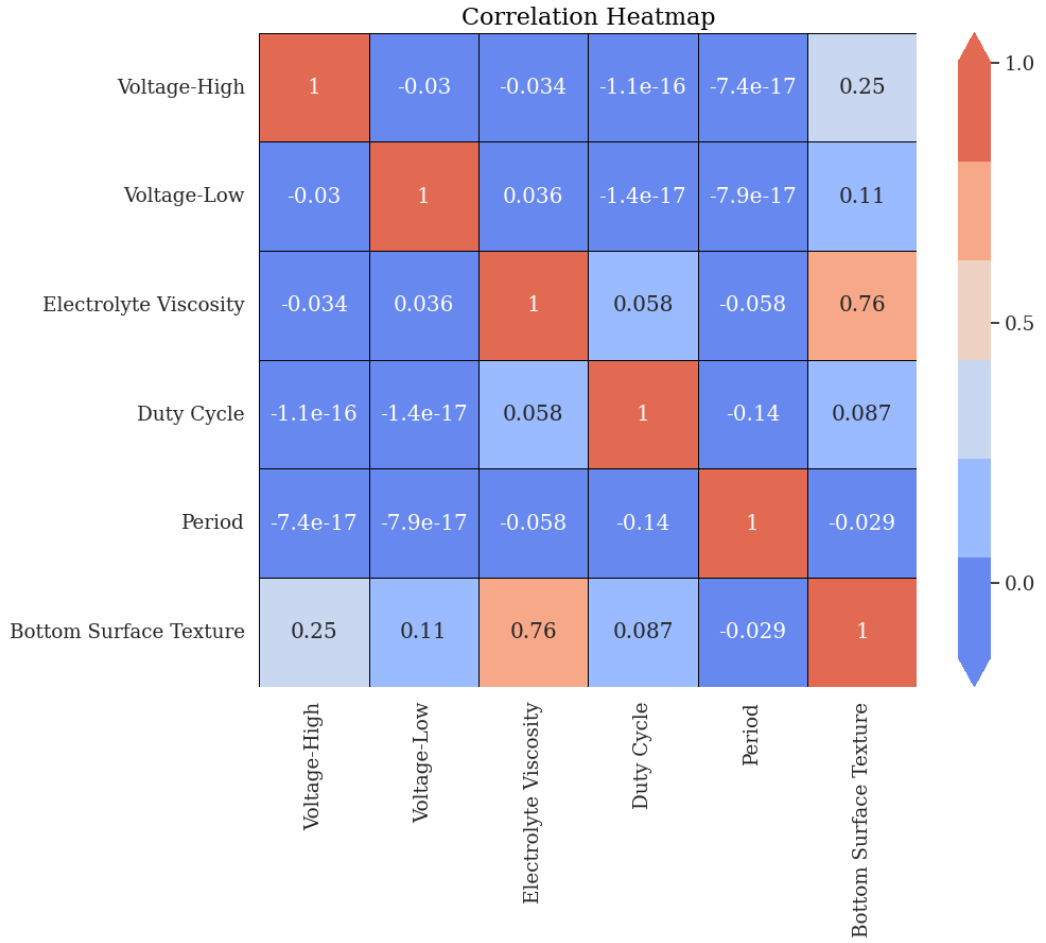

Data Preprocessing

```
X_train, X_test, y_train, y_test = train_test_split(X, y, test_size=0.3, random_state=42, shuffle=True)


# Data Scaling
scaler = StandardScaler()
X_train = scaler.fit_transform(X_train)
X_test = scaler.transform(X_test)
```

Modeling

```
# Define classifiers (Step 5)
classifier_rf_bottom_surface = RandomForestClassifier()

classifier_lr_bottom_surface = LogisticRegression()

classifier_svm_bottom_surface = SVC()

classifier_knn_bottom_surface = KNeighborsClassifier(n_neighbors=5)  # You can adjust the number of neighbors as needed


# Train the models (Step 5)
classifier_rf_bottom_surface.fit(X_train, y_train['Bottom Surface Texture'])

classifier_lr_bottom_surface.fit(X_train, y_train['Bottom Surface Texture'])

classifier_svm_bottom_surface.fit(X_train, y_train['Bottom Surface Texture'])

classifier_knn_bottom_surface.fit(X_train, y_train['Bottom Surface Texture'])
```

```
KNeighborsClassifier
KNeighborsClassifier()
```

```
# Make predictions and evaluate the models (Step 6)
# For Random Forest
rf_bottom_surface_predictions = classifier_rf_bottom_surface.predict(X_test)

# For Logistic Regression
lr_bottom_surface_predictions = classifier_lr_bottom_surface.predict(X_test)

# For Support Vector Machine
svm_bottom_surface_predictions = classifier_svm_bottom_surface.predict(X_test)


knn_bottom_surface_predictions = classifier_knn_bottom_surface.predict(X_test)
```

```
# Evaluate the models

print("Support Vector Machine Classification Report for Bottom Surface:")
print(classification_report(y_test['Bottom Surface Texture'], svm_bottom_surface_predictions))

print("Logistic Regression Classification Report for Bottom Surface:")
print(classification_report(y_test['Bottom Surface Texture'], lr_bottom_surface_predictions))


print("Random Forest Classification Report for Bottom Surface:")
print(classification_report(y_test['Bottom Surface Texture'], rf_bottom_surface_predictions))


print("KNN Report for Bottom Surface:")
print(classification_report(y_test['Bottom Surface Texture'], knn_bottom_surface_predictions))
```

```
Support Vector Machine Classification Report for Bottom Surface:
              precision    recall  f1-score   support

       Rough       0.83      1.00      0.91         5
    feathery       0.67      0.80      0.73         5
      smooth       1.00      0.33      0.50         3

    accuracy                           0.77        13
   macro avg       0.83      0.71      0.71        13
weighted avg       0.81      0.77      0.74        13

Logistic Regression Classification Report for Bottom Surface:
              precision    recall  f1-score   support

       Rough       0.71      1.00      0.83         5
    feathery       1.00      0.60      0.75         5
      smooth       1.00      1.00      1.00         3

    accuracy                           0.85        13
   macro avg       0.90      0.87      0.86        13
weighted avg       0.89      0.85      0.84        13

Random Forest Classification Report for Bottom Surface:
              precision    recall  f1-score   support

       Rough       1.00      1.00      1.00         5
    feathery       1.00      1.00      1.00         5
      smooth       1.00      1.00      1.00         3

    accuracy                           1.00        13
   macro avg       1.00      1.00      1.00        13
weighted avg       1.00      1.00      1.00        13

KNN Report for Bottom Surface:
              precision    recall  f1-score   support

       Rough       0.80      0.80      0.80         5
    feathery       0.60      0.60      0.60         5
      smooth       0.67      0.67      0.67         3
```